Etude de la dynamique des parois de domaine magnétique en présence d'un fort couplage spin orbite : amortissement chiral et origami magnétique

Safeer Chenattukuzhiyil

Communauté
UNIVERSITÉ Grenoble Alpes

THÈSE

Pour obtenir le grade de

DOCTEUR DE LA COMMUNAUTÉ UNIVERSITÉ GRENOBLE ALPES

Spécialité : NANOPHYSIQUE

Arrêté ministériel : 25 mai 2016

Présentée par

Safeer CHENATTUKUZHIYIL

Thèse dirigée par **Gilles GAUDIN**, ~

et codirigée par Ioan Mihai MIRON

préparée au sein du **Laboratoire Spintronique et Technologie des Composants**
dans **l'École Doctorale Physique**

Etude de la dynamique des parois de domaine magnétique en présence d'un fort couplage spin orbite: amortissement chiral et origami magnétique

Study of domain wall dynamics in the presence of large spin orbit coupling: chiral damping and magnetic origami

Thèse soutenue publiquement le **27 octobre 2015**,
devant le jury composé de :

Monsieur GILLES GAUDIN
CHARGE DE RECHERCHE, CNRS DELEGATION ALPES, Directeur de thèse
Monsieur IOAN MIHAI MIRON
CHARGE DE RECHERCHE, CNRS DELEGATION ALPES, Co-directeur de thèse
Monsieur BERT KOOPMANS
PROFESSEUR, UNIVERSITE TECHNIQUE EINDHOVEN PAYS-BAS, Rapporteur
Monsieur JOERG WUNDERLICH
DIRECTEUR DE RECHERCHE, LABORATOIRE HITACHI CAMBRIDGE - UK, Rapporteur
Monsieur TERUO ONO
PROFESSEUR, UNIVERSITE DE KYOTO - JAPON, Examinateur
Monsieur AURELIEN MANCHON
PROFESSEUR ASSISTANT, UNIVERSITE SCIENCES TECHN. ROI ABDALLAH, Examinateur
Madame STEFANIA PIZZINI
DIRECTRICE DE RECHERCHE, CNRS DELEGATION ALPES, Président

To my mother, who sacrificed her whole life for her children..

ACKNOWLEDGMENT

And finally, I am here. A thesis that witnessed excitements and frustrations, innovations and stupidities, hardworking and hardly working, complements and controversies, etc ends here. Generally, Ph.D. student life is considered to be difficult. However, I have to admit that I had relatively pleasant time during my thesis in SPINTEC. And here, I would like to write my heartfelt thanks to all those people provided such great experiences. Let me use my scientific skills of observing, analyzing, presenting, high impact writing (which I am not sure I have) etc to describe the different behavior and characteristics of important personalities influenced my life in Grenoble.

I came to Grenoble in 2010. In SPINTEC, I did two internships followed by the thesis. I would like to start with thank two people who introduced me into SPINTEC, they are **Vincent BALTZ and Hélène BEA**. I did my first internship with them. Vincent was quite systematic, Hélène was quite energetic. And it was a perfect beginner's internship. Along with establishing my research basics, the internship also provided an answer to a query that has been perplexed in mind for a long time. Before starting my researches, I always wondered how I am going to invent something new out of nothing. The internship gave me an answer: Instead of the initial objective of the internship to study one topic, Hélène and Vincent engaged me to study two topics in parallel. I was always busy with doing different experiments during that period. Later when we wrote a paper about my internship, both of these studies were useful. It gave me the insight: If you want to invent something new, all you have to do is to go out and try different things. The inventions will follow automatically. Anyway, I would like to thank both Hélène and Vincent for teaching me the first research as well as I thank them for introducing me to the awesomeness of SPINTEC lab.

The following year I started another internship with **Gilles GAUDIN**. Now let me write about him. I used to tell people that if I go to a new lab and I do some stuff, and people ask me from where you learned to do things like that, as a way to escape, I am going to tell them that I learnt it from my old boss, Gilles. For example, if somebody asks me why I am always late to reply to my emails, I will say I learned it from Gilles. If somebody ask me why I am submitting an abstract or an application on the last day, last hour of the dead line, then I can say I learnt it from Gilles, if somebody ask me why my office is quite messy, I will again say I learnt it from Gilles. Alright, Jokes apart and being serious, I would like to write two things specifically about him. In the beginning, when I was planning to do a Ph.D., I could not find any funding from Grenoble. I was about to quit the idea of doing Ph.D. in SPINTEC. And it was Gilles confidence that gave me this Ph.D. He had some huge money to buy some machine and he bought me instead. I would say that it indeed gave me a lot of confidence in the beginning, because the first thing that any Ph.D. student required from their supervisor is, not their help to do experiments or understand the theory , instead it is to have a belief in their students that they are capable of doing something. And I think I always got this encouragement from Gilles throughout my Ph.D. So I would like to thank him for his faith in me, believing in my abilities and giving me this PhD. And the second thing, among all the people I worked he is one such person who was open for everything and

he was quite straight. Whenever I said some new ideas, if it was good he agreed very fast, whenever I said stupid things he said I was stupid. I thank him, for being straight and supportive, and being cool and not being so bossy, or not making me feel that you are my boss.

On the other hand, next, I would like to thank Mr. **Mihai MIRON**, for always making me feel that he is the boss. Many people asked me how to deal with Mihai as a supervisor? If I give a proper answer, I may have to write an additional chapter in this thesis and that can be inappropriate. For the time being I reveal you the basic and simple way to deal with him: Mihai is sometimes a stubborn person. So if you want to work with him, be stubborn. If you have an argument with him over something, especially on physics, at the end any way he is going to win and you are going to lose; but never let him win very fast. More you fight with him, more you learn. Forgetting his nerdy side and, as my gratitude to his project money that was paid for many of my conference trips, let me write a few good words about him. I would say that Mihai is one of the brightest scientific minds in SPINTEC. He is not only bright but also passionate to do science. He is somebody who is doing science because of the absolute pleasure of finding new things. And it is quite unique. And I have to say that among all the people I worked with, he was the sharpest one, who understood things very quickly. May be these are known facts. But I can tell you something nobody noticed about him. I already said he is like the boss. I would like to call him a leader. Boss is somebody who stands in front of you and asks you to follow. The leader is somebody who stands behind you and pushes you to the front. Mihai will look like a boss, when you actually know him; you will understand he is not. All he wants is to stand behind you and push you towards excellence. It was an absolute pleasure to work and share ideas with Mihai. And I thank him for all his help.

Next, I would like to thank a French girl who went to USA and surprisingly, prefers to stay there instead of coming back: **Emile JUE**. My thesis was a continuation of her works. Her presence in the first year of my Ph.D. was highly helpful. She taught me all the basic experimental procedure. Even though I had my supervisors to guide me, having a person like her who performed the everyday experiments, made my life easier. When we do experiment, sometimes it gets struck due to small issues (for example, misplacement of a connection wire) and it may consume a lot of time to fix. In my case, I did not have such problems because Emilie was experienced and already aware of such little problems. It saved a lot of my time. And I wish every Ph.D. have a ‘Godfather’ like I had. I thank Emilie for her caring, for her help and paving my way to do better experiments.

Next I would like to thank two people from Neel institute, **Stefania PIZZINI and Monsieur Jan** for their help in my thesis. The best example to explain their help is something Emilie told me in the first year. She was teaching me how to solve when I have a problem when I work in Neel institute. She said: if you find a problem related anything related to any machine or microscope, do not touch on anything, go to Stefania's office and cry. And if Stefania is not available to see you crying, then go to Jan's office and cry. And if you don’t find both of them, then cry for yourself. I don’t know crying was her thing, but the

message was clear. It is that if i have some problems in Neel Institute, all you have to do is to go to Jan and Stefania. I would like to thank both for their help, especially to understand the experimental technique in the beginning of my Ph.D.

Then I would like to thank **Olivier BOULLE**. Olivier was my supervisor for my second internship. I really want to write something about him, but I am puzzled. Maybe, he is a mystery man got away from my detective abilities and did not give me a chance to analyze his character. Anyway I thank for all his help, his contributions to the experiments, sharing ideas in the group, simulations etc

I would like to thank **Liliana Daniela Buda PREJBEANU**, for her help by performing simulation. I can write two things about her: The first one, Liliana is mentally the most active and vibrant lady in SPINTEC. Second, she is the only one in SPINTEC who got a name that is longer than my name! (Congratulations, that is a rare achievement).

A very special thanks to **Stéphane AUFFRET** for his help in sample fabrications.

I thank **Aurelien MANCHON** from King Abdulla University of Science and Technology (KAUST), Saudi Arabia for his contributions in the theoretical understanding of my experimental results.

The toughest job during my Ph.D. was neither doing experiments nor understanding the physics. It was to deal with the French administration process and paper works. I would like thank **Catherine, Rachel and Sandra** for their help in dealing those difficult jobs.

Thanks to **Jean-Pierre, Lucian and Bernard** for their vision and leadership behind the success of SPINTEC that I can always be proud of.

Then I would like to thank all the people in my SOT group, **Karol, Natalie, Paul, Marc, Alex Sr, Alex Jr, Alexu, Claire** and **Ali** for their contributions to the group discussions and helping me to understand the various aspect of the subject.

Thanks to all other friends in SPINTEC: **Léa, Melissa, Antoine, Magali, Tulio, Yvan** (the China co-travelers), **Lampirini, Paulo, Jérémy, Mathieu** (the international food party organizers), **Abhijit, Jyotirmoy, Titiksha, Amit and Hiteshika** (the SPINTEC Indians), **Fabrice and eVaderis team** (invaders of Safeer's office) **Christophe, PY, Thomas, Cécile, Selma** and all others.

Next, I would like to thank people outside of SPINTEC. I thank University of Delhi, for providing me all the necessary arrangement and financial support to come to Grenoble for doing my masters. I thank all my master colleagues from Delhi University with whom I spent one of the best times of my life. Coming from India and living in a western country like France was quite challenging and it would not have been possible without having good friends. I thank **Mincho** and **Iulia** for being my best friends in Grenoble. I would like to

thank **Dhruv**, who came to Grenoble with me and he was the only person lasted from the beginning to the end. I gratefully remember two precious ladies I met in Grenoble, **Divya and Ketki**, for bringing new adventures and enlightenments in my life. I thank **Akhil, Meera, Shanti and Nimisha,** the people from my state in India whom I could share my homely memories.

Life in Grenoble taught me a lot of new things other than science. Learning photography was one of them. During my thesis period, I could bring a large improvement in my artistic abilities. I would like to specially thank **Claire and Guillaume** for their continuous support for doing photography. I also thank all other gorgeous models who posed for my crazy photographic experiments.

Finally, I would like to thank my family. I am blessed to have parents who never said any objections to any of my wishes. I always enjoyed the freedom they gave me and it definitely helped me to become a highly independent person. I gratefully acknowledge the sacrifice of my siblings and their support to fulfill their youngest brother's dreams.

At last, I would like to thank all the people who directly and indirectly helped me to become who I am. Thanks for your suggestions and advice that improved me both personally and professionally. In case if I did not consider somebody's criticism, I am sorry. Maybe, I was trying to do it my own way!

Merci beacoup..

CONTENTS

Chapter II

Chapter III

Chapter IV

Introduction

Late 20th century was remarkable in the history of mankind because of the technological revolution. During this period, we witnessed unprecedented evolution of semiconductor and microelectronics industries. Incredible machines were built that pushed performances of human's tasks to new heights. These days, everyone's life has become unthinkable without electronic devices such as computers, mobile phones etc.

Magnetic memories are an integral part of these devices. In the last few decades, from magnetic tapes to hard drive disks (HDD), the storage capacity has been increased by orders of magnitude. Nowadays, data density in hard drive disks is close to the Tbit /inch^2. The discovery of the giant magnetoresistance (GMR) in 1988 was an important breakthrough in the development of high density HDD since it enhances reading performances. The GMR is a significant change in the electrical resistance of a magnetic multilayer depending on whether the magnetizations of adjacent ferromagnetic layers, separated by a metallic non-magnetic layer, are in a parallel or an antiparallel alignment. Spintronics, which combines magnetism and electronics, emerged from this discovery. Controlling the magnetization by means of the current or vice versa the current by means of the magnetization offers an extra degree of freedom for the development of memory and logic devices. One of the first results was the discovery of the Tunnel Magnetoresistance (TMR), where, unlike the case of GMR, the two adjacent magnetic layers are separated by an insulating layer. This particular stack is called a magnetic tunnel junction (MTJ). Since TMR can reach several hundreds percents where GMR is limited to some tens. It was rapidly integrated in the read head of HDD and participates to a further increase in the storage density.

Soon after, Magnetic Random Access Memories (MRAM) were proposed and attracted a strong interest since they combine large endurance and non-volatility. They are based on MTJ and their read uses the TMR signal. Different approaches were introduced for the writing. The first generation used a field created by a current flowing through "write-lines". This approach raises several serious issues, particularly concerning its scalability. Since the magnetic field is proportional to the current, the current density diverges when the bit sizes decrease. The last generations are based on the Spin Transfer Torque phenomena (STT): a current flowing through a magnetic layer gets polarized and can excite the magnetization of an adjacent magnetic layer by transfer of spin angular momentum. This discovery that the magnetization can be manipulated by use of an electric current was an important achievement of spintronics. STT naturally solves the scalability issue. However even though it offers large endurance for relatively slow writing, an accelerated aging of the tunnel barrier is observed for fast switching that requires large current density. Moreover, since write and read paths are identical, unintentional write can be observed during writing if the read and write current distributions are not sufficiently separated.

Very recently, other torques were identified in structures with inversion asymmetry (SIA) such as heavy metal/ferromagnetic layer/insulating layer. These torques, so called spin orbit torques (SOT), originate from the spin orbit interaction: angular momentum is transferred to the magnetization from the orbital part of the carrier wave function, and produces the SOT. Depending whether the effect comes from the bulk of the heavy metal or the interfaces of the magnetic layer, two mechanisms were identified as responsible for the existence of the SOT, respectively the Spin Hall Effect (SHE) and the Rashba effect or more generally, the Inverse Spin Galvanic Effect. Since the current used for switching the magnetization by SOT is injected in the plane of the layer and not through the tunnel barrier, a SOT-based writing naturally solves the issues faced by the STT-MRAM: the MTJ is not damaged by the injection of large current densities and the read and write paths are decoupled. Moreover, very fast determinist and not precessional switching (switching time <200 ps) were observed experimentally in both Pt/Co/AlO_x and Ta/CoFeB/MgO based stacks. SOT-MRAMs are then credible candidates for the introduction of non-volatility in the memory hierarchy and particularly for SRAM replacement in high level cache memory.

For dot diameter larger than 30nm, magnetization reversal in SOT-MRAM involves the nucleation of a reverse domain followed by the domain wall (DW) propagation. Therefore understanding the current induced DW motion is mandatory for improving and optimizing these memories. Moreover, other memory and logic device concepts were introduced these last years, based on current domain wall motion. The most famous one is certainly the race track memory proposed by S.S. Parkin from IBM in 2004. The information is stored in nanowires in the form of magnetic domains separated by DWs. A current injected in the nanowires moves the DW-train back and forth. A read and write elements are located beneath the DW-train. This 3D-concept offers potentially very large density and fast data transfer.

Initial experiments on current induced DW motion focused on in-plane material and particularly on permalloy. The observation at SPINTEC of very fast, reproducible current induced domain wall motion in the direction opposite to the electron flow, in Pt/Co/AlOx multilayers in 2009, has rapidly attracted a tremendous interest. From an application perspective, this discovery opened a new route for the realization of the different proposed DW-based concepts. From a fundamental point of view, this observation raised several questions that needed to go beyond the STT mechanism considered so far. The strong SOT measured independently in these stacks was rapidly taken into account. However, its action depends on the DW structure: it is efficient in moving the DW as soon as its core magnetization starts having a component in the current direction. Moreover, two consecutive DW need to have opposite components to move in the same direction. Recently, the Dzyaloshinskii-Moriya interaction (DMI) was identified to be the “missing” ingredient and the SOT+DMI could explain several experimental results.

However, previous studies performed at SPINTEC on Pt/Co/AlO_x by Emilie Jué during her PhD thesis (unpublished) showed incompatibilities with this DMI+SOT model. Therefore, my first goal was to understand these incompatibilities and to test this DMI+SOT model in configurations different than the ones studied commonly. In order to try to get a picture as complete as possible, I studied in parallel two different systems.

Since the DMI+SOT model of the current induced DW motion involves several parameters such as the amplitudes of the SOT, the STT and the DMI, I choose to study a simpler case in addition to the current induced DW motion: the field induced DW motion. Moreover, in order to identify the role of the DMI, I choose systems presenting weaker SIA: Pt/Co/Pt multilayers with different Pt thicknesses. Following these experiments I identified a new source of chirality, the chiral damping.

In the STT approach, the geometry of the device controls both the shape of the magnetic layer and the current direction. This is true either for pillar geometry in the case of a uniform magnetization and for wire geometry in the presence of a DW. In the case of SOT, the "source" i.e. the non-magnetic layer, can be shaped independently from the magnetic layer. This gives a new degree of freedom and allows controlling the spatial and temporal distributions of the torques acting on the magnetization. Based on this completely new idea emerged during my PhD, I performed experiments in the so-called "non collinear geometry" in Pt/Co/AlO_x multilayers: Co/AlO_x wires with different orientations are patterned on top of a Pt pad. My results cannot be explained with the SOT+DMI mechanism and ask for a more complete model. Moreover, the observed angle dependent current induced DW velocity, was used to design new flexible and multifunctional devices. Some of them were built and tested.

This manuscript is divided into four chapters.

In the first chapter, I present the state of the art. I introduce the basic magnetism concepts needed to understand my experiments and results. The domain and DW formation in material with perpendicular magnetic anisotropy, the physical mechanisms associated with the magnetization dynamics and the current induced torques (STT and SOT) are discussed in details in this chapter. A special attention is given to the analysis of the SOT related studies. This is important for understanding the depths and shallows of my results.

In the second chapter, I introduce the different techniques used in my experiments. I first introduce the Kerr magnetic imaging technique that I used to image the DW displacements. The detailed description of the deposition of Pt/Co/Pt and Pt/Co/AlO_x multilayers studied during my PhD, as well as their nano-structuration follows. Finally, I explain the experimental set-up used respectively for the field induced and current induced DW motion studies.

The third and fourth chapters are dedicated to my experimental results and interpretation. In chapter 3, I present both current and field induced DW motion experiments in the weak SIA system, the Pt/Co/Pt multilayers. The studies on system with strong SIA ($Pt/Co/AlO_x$) are described in chapter 4.

In weak SIA multilayers such as Pt/Co/Pt, current induced DW motion is expected to be very slow. We performed a simple qualitative analysis of this slow DW motion and, in order to check the validity of our conclusions, we compared them with field induced DW motion. Systematic and detailed quantitative studies of the field induced DW motion in the presence of both out-of-plane and in-plane fields were performed. Following these experiments I evidenced the existence of the chiral damping that will enrich the understanding of DW dynamics.

In chapter 4, I present my studies on non-collinear current induced DW motion in $Pt/Co/AlO_x$. Beyond the conventional one-dimensional geometries, I show that the current induced DW motion can be extended to 2D shapes and that unexpected results are obtained. Based on these results, I designed new magnetic device concepts. The details of this device's construction, working principle and proof of concept are described in this chapter. Finally, a general conclusion is given and perspectives complete the manuscript.

The experiments were done in collaboration between two laboratories in Grenoble: SPINTEC and Institute Neel. The nanofabrication was performed in the clean room facilities of Platforme Technolgie Amont (PTA), CEA Grenoble.

Chapter I : State of the art

In this section, I will describe the basic concepts in magnetism required to understand my experimental results. I will begin with the different energies existing in ferromagnetic systems. Based on this I will explain the magnetic domain wall formation. After, the characteristics of the domain wall motion under the magnetic field and the electric current will be discussed with an emphasis on the effect of the spin transfer torque and spin-orbit torques on the domain wall dynamics. Finally, the role of Dzyaloshinskii Moriya interaction in domain wall motion will be discussed.

I.1. Energies of a ferromagnetic system

In a macroscopic ferromagnetic material, the magnetic structure forms microscopic regions called magnetic domains. Each domain consists of magnetic moments of atoms aligned in the same direction forming a uniform net magnetization. The boundaries separating two different magnetic domains are called magnetic domain walls.

The domain formation occurs to minimize the total energy of the magnetic system. Depending on the magnetic material, several different energy contributions compete with each other to produce complex magnetic domain and domain wall patterns [O'Handley, 1999]. The common energy contributions in a magnetic system are described in the below section.

I.1.1 Zeeman energy (Due to an external field)

The Zeeman energy is related to the interaction between the magnetic moments and an external magnetic field: the magnetization tends to point along the direction of the field to minimize its energy. This energy is expressed as

$$E_{zeeman} = -\mu_0 . \overrightarrow{H_{ext}} . \vec{M}$$

Where μ_0 is the magnetic permeability of vacuum, $\overrightarrow{H_{ext}}$ is the external magnetic field and $\vec{M}$ is the magnetization.

I.1.2 Exchange energy

The energy associated with the coupling of the magnetizations of two neighboring atoms is the exchange energy. Depending on the nature of the coupling, the two magnetizations tend to align parallel (ferromagnetic coupling) or anti-parallel (anti-ferromagnetic coupling) to each other. It is a short range interaction which is strongest for two adjacent atoms. The net exchange energy can be written as the summation of the interaction between all the atoms as shown below.

$$E_{Exchange} = \sum_{i,j} \overrightarrow{S_i} . \overrightarrow{S_j} \cos \varphi_{ij}$$

Where $\overrightarrow{S_i}$ and $\overrightarrow{S_j}$ are two neighboring spins and φ_{ij} is the angle between them [Buschow 2003].

The exchange interaction is isotropic, resulting in no preferential orientation of the magnetization with respect to the crystal axis.

I.1.3. Magnetostatic energy

Magnetostatic energy can be also referred as magnetic stray field energy, magnetic dipolar energy or demagnetizing energy. This energy expresses the magnetic interaction between two magnetic dipoles and depends on their relative direction and on the distance between them. Locally the demagnetizing energy is small compared to the exchange energy. Thus it has less influence on the alignment between two neighboring magnetic moments. However, it is a long range interaction that can influence the spatial distribution of the magnetization. Mathematically, it can be expressed as [Hubert 1988] .

$$E_{\ magnetostatic} = \frac{1}{2} \mu_0 \int \vec{H}_{dm} \ . \vec{M} \ dV$$

Here $\vec{H}_{dm}$ is the demagnetizing field. It depends linearly to the magnetization and a geometry dependent constant (N).

$$\vec{H}_{dm} = -N . \vec{M}$$

It is very difficult to calculate the value of H_{dm} of an arbitrary shaped magnetic object. This is because the interaction is long range and all the interactions between each of the dipoles in the system should be considered.

I.1.4. Magneto crystalline energy

In certain crystals, the magnetization prefers to align along specific crystal axes. The related energy is called the magneto-crystalline energy. This energy is anisotropic and the preferential axes depend on the system: they can be defined either by the bulk of the material and particularly the crystal lattice or by the interfaces.

In a system with uniaxial crystalline anisotropy, the magneto-crystalline anisotropy energy can be written as

$$E_{magnetocrystalline} = K_u \,.\, sin^2\theta$$

Where K_u is the uniaxial magneto-crystalline energy constant and θ is the angle between the magnetization and the anisotropy crystalline axis. For complex crystal lattices, the above equation can include higher order terms [O'Handley, 1999].

The magnetocrystalline energy is dictated by the anisotropy of the orbital momentum and to the strength of the spin orbit interaction. The crystal field breaks the spherical symmetry of the atomic wavefunctions and sets the orientation of the orbital momentum. The spin orbit interaction, $H_{so} = \lambda L.S$, couples the spin of the electrons (S) to its orbital angular momentum (L). Ultimately the anisotropy depends on the crystallographic arrangement of the material. As a result, the magnetization prefers to align with certain crystal axis [O'Handley, 1999].

I.1.4.1. Out of plane magnetic anisotropic materials

The magneto-crystalline anisotropy originates from both the bulk and the interface. In ferromagnetic thin films, the contribution from the interface plays an important role, as it may exceed the in-plane shape anisotropy created by the demagnetizing field and bring the magnetic easy axis out of plane [Néel 1954].

In my experiments, I used two kinds of perpendicular magnetic trilayer systems: Pt/Co/Pt and Pt/Co/AlO_x. Here both interfaces contribute to the anisotropy. The typical values of the anisotropy field are of the order of $H_k >$ 9Koe in Pt/Co/AlO_x and H_K >3Koe in Pt/Co/Pt.

The interface contribution to the anisotropy of these materials is well established. The out of plane magnetic anisotropy was observed both in multilayers with ferromagnet/ heavy metal interfaces (Co/Pt, Co/Pd, CoFeB/Ta etc) as well as those with ferromagnet/oxide interfaces (Co/AlO_x, CoFeB/MgO).

While the large spin orbit interaction plays an important role for the contribution of the ferromagnet/ heavy metal interface, in the case of the ferromagnet/oxide interface [Monso 2002] the spin orbit interaction is smaller. Here the anisotropy is highly dependent on the oxidation state at the interface. At an optimal oxidation condition, a strong out of plane magnetic anisotropy can be achieved [Rodmaq 2003]. The origin of the anisotropy is the strong hybridization of the orbitals of the transition metal and oxygen. This mechanism was confirmed by ab-initio calculation [Yang 2011]. This study showed that the hybridization of the 3d orbital of the metal and the 2p orbital of the oxygen can lead to out of plane magnetic anisotropy. They also showed that the anisotropy is reduced in over-oxidized and under-

oxidized interfaces due to modification of the hybridized state due to the presence or the absence of the oxygen atoms. A later study showed that the anisotropy is also sensitive to thermal annealing [Rodmaq 2009]. Here it was shown that the annealing induces the migration of oxygen towards the interface resulting better interface and thus large anisotropy.

I.2. Magnetic Domain and domain wall formation

A simple picture of magnetic domain formation in a perpendicular magnetic system due to the interplay of magnetostatic anisotropy and exchange energies is shown in figure I.1. Consider that initially the magnetic material consists of a single domain of uniform magnetization (figure I.1.a), pointing along the perpendicular direction (due to the anisotropy). Magnetic charges appear at two opposite edges creating a strong demagnetizing field in the system and increasing the magnetostatic energy (or dipolar energy). In order to minimize this energy, the magnetic structure gets divided into domains forming domain walls between them (figure I.1.b). The final structure minimizes the total energy by reducing the dipolar energy of the system at the cost of domain wall energy (anisotropy and exchange).

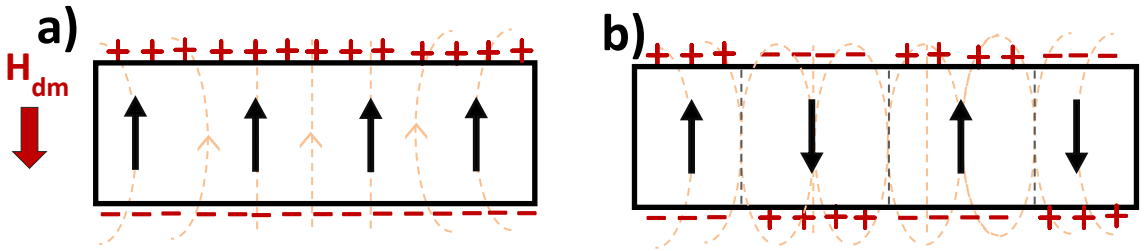

Figure I.1. The schematic diagrams of magnetic domain wall formation in a rectangular structure. **A)** In a single domain case, the magnetization aligns along one direction, creating magnetic charges at two opposite edges of the rectangular slab. These magnetic charges in turn create a strong demagnetization field inside the magnetic material**. b)** To minimize its total energy, magnetic domains are formed so that magnetic charges created by one magnetic domain get canceled by the magnetic charges in the adjacent domains.

I.3. Magnetic domain walls

The domain wall (DW) is the small region in between two different magnetic domains Inside the DW, the magnetization rotates from one domain magnetization direction to the other. The width of the DW(Δ) depends on the competition between the exchange energy (A) and the anisotropy (K): [O'Handley, 1999] [Buschow 2003]

$$\Delta \propto \sqrt{\frac{A}{K}}$$

The exchange interaction favors large DW width so that the neighboring magnetic moments are separated by small angles. The anisotropy in contrast tends to minimize the number of the magnetic moments not aligned along the easy axis. A thin DW will then be obtained when the anisotropy is large compared to the exchange energy.

I.3.1. Bloch and Néel domain walls

Domain walls can be different of types depending on the way the magnetization varies inside the domain wall. In in-plane and out-of-plane magnetic materials, different DW types were reported. In my experiments, I only studied out-of-plane magnetic systems. Hence, the discussion on the DW presented in the coming section will be focused only on magnetic systems with out-of-plane magnetic anisotropy. In this case, the magnetization of the domains is directed either up or down. The magnetization inside the domain wall rotates from up to down or vice versa.

Two types of DW can be distinguished: Bloch walls and Néel DW. If the magnetization rotates in the plane containing the magnetizations of the two domains, it is called a Néel DW. For a Bloch DW, the magnetization rotates perpendicular to this plane. [Gignoux 2005]

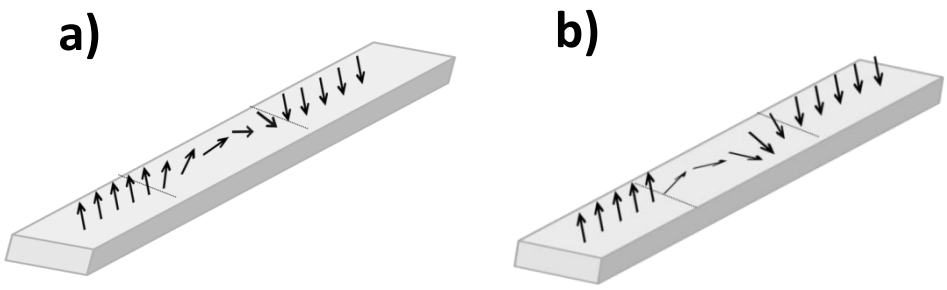

Figure I.2. The schematic diagrams of a Néel and a Bloch DW in a wire with perpendicular magnetic anisotropy. **a)** The Néel DW. The magnetization inside the domain wall varies its direction along the DW length. **B)** The Bloch DW. The magnetization rotates out of plane to the DW length.

A schematic diagram of these two DWs is shown in figure I.2. In perpendicular systems with large anisotropy the width of the DW is generally smaller than the width of the nanowire. Magnetization rotating perpendicular to the DW width would cost less dipolar energy compared to the rotation along the DW. Thus, the DW will prefer the Bloch structure.

I.4. Domain wall motion

A magnetic DW can be moved both by magnetic field (H_{ext}) and electric current (I). The magnetic field induced DW motion is due to the Zeeman energy described above while the current induced DW motion is due to the interaction between the spins of the conducting electrons and the local magnetization: spin torque effects. The major difference between these two kinds of DW motion in a nanowire is shown in figure I.3. The magnetic field induces bi-directional DW motion: magnetic domains oriented parallel to H_{ext} are energetically favored and expand while magnetic domains oriented anti-parallel to H_{ext} shrink. Then, two adjacent domain walls will move opposite to each other. The current induced DW motion is unidirectional. All the domain walls move in the same direction and the magnetic configuration is eventually shifted. From memory application point of view, the current induced DW motion is considered to be important. This is because it does not alter the magnetic domain structure so that the magnetic information can be retained during the motion in contrast with the field induced domain wall motion. [Hayashi 2008]

The physical mechanisms behind these two kinds of domain wall motion are described in details in the following sections.

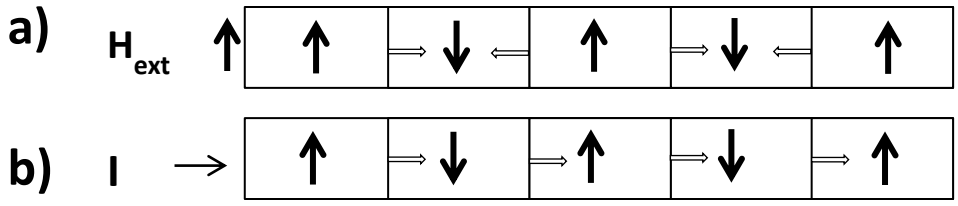

Figure I.3: The domain wall motion in nanowires in presence of **a)** an external field (H_{ext}) and **b)** an electric current (I). The field induced domain wall motion results in expansion or contraction of the magnetic domains whereas the current induced domain wall motion results in the displacement of magnetic domains along the nanowire.

I.5. Field induced domain wall motion

In magnetic thin films and bulk materials, the magnetization reversal can occur through domain nucleation and domain wall propagation. Figure I.4 shows different magnetic states during the magnetization reversal under an applied external magnetic field (H_{ext}). When H_{ext} is larger than the saturation field (H_{sat}), the magnetic system is in a single domain state. When H_{ext} is slowly increased in the opposite direction, a magnetic domain with opposite magnetization gets nucleated. In the realistic experimental case, the magnetic system has imperfections due to defects, crystal mismatches etc. These imperfections can have weaker

anisotropies where the magnetization reversal requires smaller fields compare to the other parts of the magnetic system. These spots serve as the source of initial domain nucleation creating domain wall boundaries in the magnetic structure. As the magnetic field is increased further, these domain walls can move expanding the nucleated domain. At the same time, new domains can also be nucleated. When the H_{ext} becomes larger than H_{sat} in the opposite direction, a monodomain state is obtained.

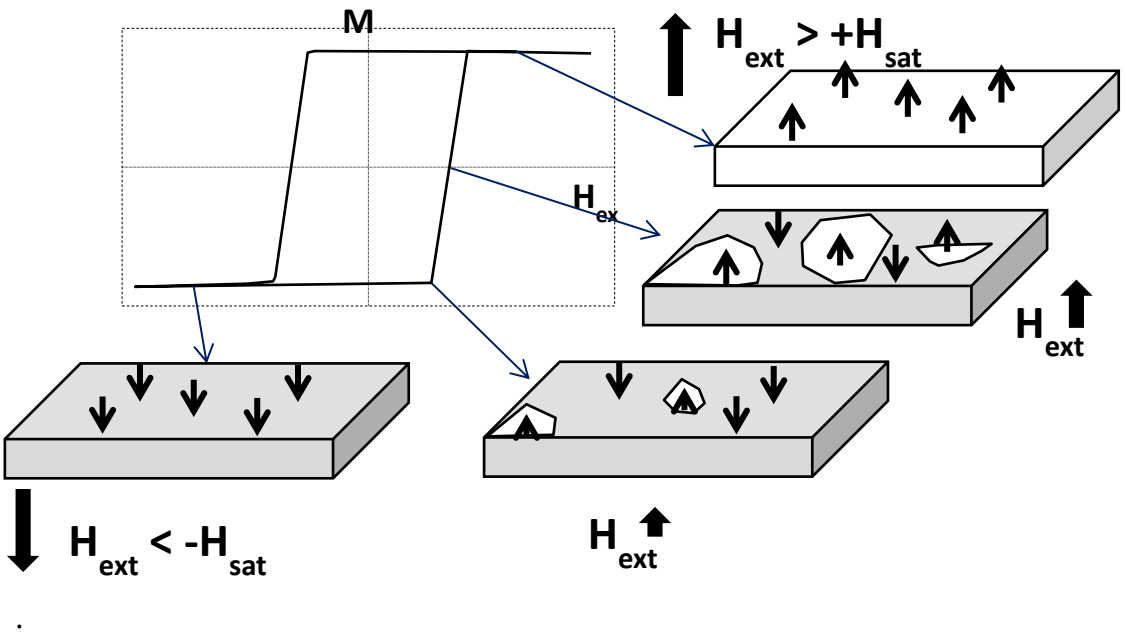

.

Figure I.4. Schematic diagrams of the magnetic reversal through a nucleation/propagation mechanism. **A)** At $H_{ext} < -H_{sat}$, magnetization is saturated along the applied field direction **b)** For a small positive applied field domains with up magnetization are nucleated c) At higher positive field, domain walls moved and the nucleated domains expand d) At $H_{ext} > +H_{sat}$, the magnetization is saturated up resulting in a single domain state.

In this section, at first I will briefly describe the physical mechanisms governing the field induced DW dynamics. Then I will show the comparison of these theoretical models with the experimental results.

I.5.1. LLG equation

The time and space evolution of the magnetization under the application of a magnetic field is mathematically described by the Landau Lifshitz Gilbert (LLG) equation. The same equation can be used to understand the magnetization reversal of a uniform magnetic domain

as well as the magnetization dynamics inside the DW. The equation was first proposed by Landau Lifshitz [Landau-Lifshitz 1935] and then modified by Gilbert [Gilbert 2004].

When an external magnetic field is applied to a magnetic material, the magnetization starts to precess around the field axis. The torque that causes this precession can be written as

$$\frac{\partial \vec{M}}{\partial t} = -\gamma \vec{M} \times \vec{H}_{eff}$$

Here γ is the gyromagnetic ratio, $\gamma = \frac{ge\mu_0}{2m_e}$ where g is the Lande factor (~2). H_{eff} is the effective field including all the contributions from exchange field, magneto-crystalline anisotropy field, external applied field etc.

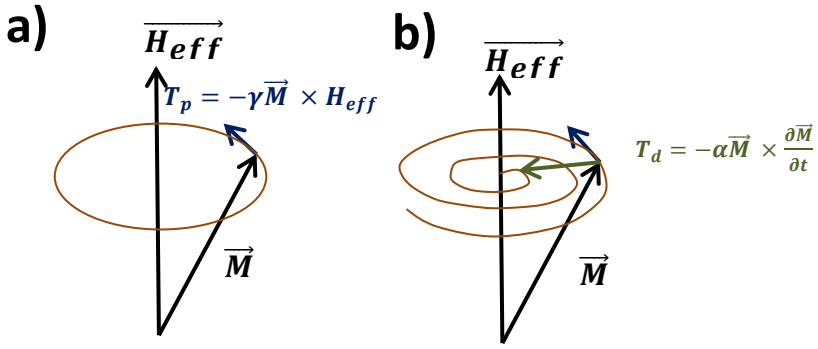

Figure I.5. The schematic diagram showing the magnetization dynamics under an applied external magnetic field. **A)** Precession of the magnetization around H_{eff} without any damping. The magnetization describes a perfect cycle. **b)** In the presence of the damping, the magnetization relaxes along H_{eff} describing a spiral. The damping torque is perpendicular to the spiral.

Considering only this torque, the magnetization will precess endlessly around the external field. This is not what is observed experimentally: when an external field is applied, the magnetization relaxes into an equilibrium state aligned along $\vec{H}_{eff}$. Hence, an additional torque describing the damping (T_d) is required to explain the magnetization dynamics. In the LLG formalism, the damping can be written as

$$(T_d) = \alpha \vec{M} \times \frac{\partial \vec{M}}{\partial t}$$

Here α represents the damping constant, $\alpha > 0$. The damping mechanism is associated with a transfer of energy from the magnetic system to other degrees of freedom such as the lattice through the spin-orbit coupling.

Therefore, the LLG equation for the net magnetization dynamics can be written as the summation of two terms: a precessional term and dissipation term.

$$\frac{\partial \vec{M}}{\partial t} = -\gamma \vec{M} \times \vec{H}_{eff} + \alpha \vec{M} \times \frac{\partial \vec{M}}{\partial t}$$

I.5.2. Field induced domain wall dynamics

Even though the DW has a non-uniform magnetic texture, the DW dynamics can be described using relatively simple models. This is because the non-uniformity of the magnetization in the DW (the DW width) is fixed by energies (anisotropy and exchange) much larger than the Zeeman energy from the applied field. Therefore it can be considered constant. The only degree of freedom is the orientation of the DW core magnetization. When a magnetic field is applied, the magnetizations inside the domain wall rotate leading to the overall displacement of the domain wall. The behavior of the domain wall velocity under a magnetic field was firstly described by Walker [Schryer 1974]. According to the Walker model, the domain wall motion is divided into two velocity regimes: a steady state regime and an oscillatory regime. The steady state regime corresponds to the motion of the domain wall at low magnetic fields, and the oscillatory regime corresponds to the motion at higher fields. Both of these regimes are schematically shown in figure I.6. At low magnetic field, the velocity increases linearly with the magnetic field amplitude. Then at a certain field called the Walker field, the magnetization inside the domain wall starts to oscillate and the DW velocity drops. A further increase in the magnetic field results in a global motion of the DW along the same direction with a velocity increasing linearly with the magnetic field amplitude. However, the DW motion is turbulent: the DW undergoes transformations from Bloch to Néel to Bloch etc., and the motion is constituted of back and forth displacements.

The interplay between the different torques acting on the magnetization inside the domain wall determines the steady or oscillatory behavior of the DW motion. A simple picture of the action of the different torques on the magnetization of a Bloch wall in the presence of an external applied field (H_a) is shown in figure I.6.b. Here instead of considering the whole magnetization gradient, I will simplify the DW into a small region with a constant in-plane magnetization (shown by the red arrow in figure I.6.a). According to the LLG equation, when an external field is applied, a torque (T_a) acts on the magnetization and rotates it in the XY plane. This rotation of the magnetization creates magnetic charges at the edges of the domain wall that produce a dipolar field (H_{Demag}) along –X. H_{Demag} creates an out of plane torque (T_{Demag}) along the Z direction that pulls the magnetization out of plane. The in-plane torque (T_{Damp}) associated to the damping of this motion opposes T_a and at equilibrium they

compensate, providing a steady in-plane angle for the magnetization. The DW velocity is given by T_{Demag}.

As the magnetic field increases further, the in-plane magnetization continues to rotate, increasing T_{Demag}. However, T_{Demag} reaches a maximum for an in plane angle of the magnetization θ=45°. Beyond, T_a is no longer compensated by the T_{Damp} and the magnetization starts to precess in the X-Y plane. This phenomenon is called the Walker breakdown. Increasing further the magnetic field results in the turbulent DW motion. Since the DW undergoes back and forth displacement, the domain wall mobility in this regime is smaller compared to the steady state regime [Mougin 2007].

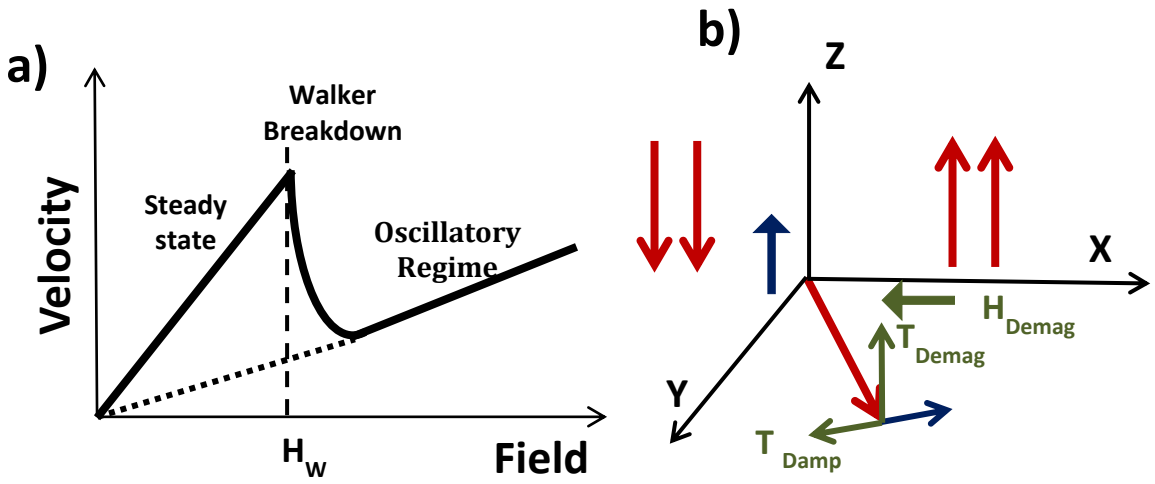

Figure I.6. a) The schematic diagram of the velocity versus the applied external field amplitude. The velocity shows two linear regimes, the steady state regime and the oscillatory or turbulent regime, separated by the Walker breakdown at field H_w. **b)** Schematics of the different torques acting on a single magnetization at the center of the Bloch domain wall. The applied field (H_a, shown in blue) is associated with as torque T_a that rotates the magnetization in the plane and creates an in-plane dipolar field (H_{Demag} shown in green). The damping torque T_{Damp} associated to the motion induced by H_{Demag} then compensates T_a. Finally, T_{Demag} pulling the magnetization out of plane results in the domain wall motion.

I.5.3. Creep and flow regimes of the domain wall motion

The model presented in the previous section is only applicable to ideal systems. The room temperature experiments show deviations from this picture. Especially at low magnetic fields, the interplay between material imperfections and thermal energy contribution plays a major role in defining the domain wall motion behavior. Samples used for domain wall motion studies exhibits imperfections and defects such as impurities, disorders. These imperfections can act as pinning, modifying the domain wall motion. At zero temperature,

they can even stop the domain wall motion. However, at finite temperature, thermal energy activates the depinning of the domain walls from these sites [Chauve 2000]. The motion regime is then dependent on the amplitude of the magnetic field. From this perspective, the magnetic field induced domain wall velocity can be divided into three regimes: the creep regime, the depinning regime and the flow regime [Metaxas 2007].These regimes are shown in figure I.7.

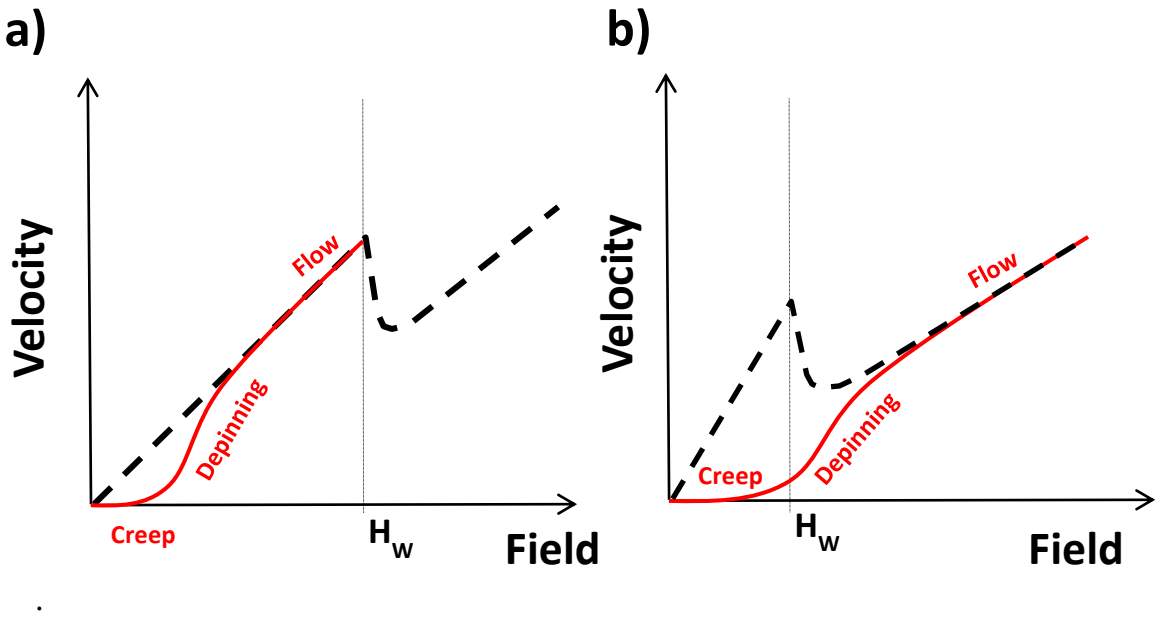

Figure I.7. The schematic diagram of the experimental field induced velocity (shown in red) compare to the velocity expected from the model presented previously (shown as the dotted black curve). **a)** For the case where the Walker breakdown occurs at fields larger than those of the creep and depinning regimes, the observed linear dependency corresponds to the steady flow regime. **B)** For smaller Walker fields the sudden velocity drop due to the Walker breakdown is not visible in the experimental curve. The observed linear regime corresponds to the oscillatory regime. One of the difficulties in analyzing experimental velocity curves is that the Walker breakdown may be hidden by the presence of defects (the creep regime and the depinning regime as shown in figure I.7). When this happens, it is not always possible to know whether the DW motion in the flow regime is steady or turbulent.

At low magnetic field, the domain wall velocity is extremely slow and the motion can be described by the dynamics of an elastic interface driven by a force in the presence of weak disorder [Lemerle 1998] [Metaxas 2007]. This regime is called the creep motion. Increasing the force, here the magnetic field, along with thermal activation energy, induces the depinning of the domain walls from the defects. Thus the domain wall velocity suddenly increases. This second regime of the DW motion is called the depinning regime and is shown

in figure I.7. As the magnetic field is increased further into high values, the domain wall motion becomes independent of the pinning defects and the domain wall velocity becomes linear as predicted theoretically. This is the flow regime

I.6. Current induced domain wall motion:

In magnetic microstructures, applying current can induce domain wall motion either along or opposite to the electric current. The torque responsible for current induced DW motion can be of two types: Spin Transfer Torques (STT) and Spin-orbit Torques (SOT). In the following section I describe different aspects of the physics associated with STT and SO

I.6.1. Spin Transfer Torques (STT)

When a spin polarized current flows through a magnetized magnetic material its spin polarization changes (it aligns with the magnetization). Since the total angular momentum (spin of conductive electrons and magnetization) is conserved, the conductive electrons transfer their angular momentum to the magnetization of the magnetic material. Thus a torque is applied on the magnetization. This spin transfer torque will eventually cause the magnetization switching if the current density is large enough (if enough momentum is transferred) [Ralph 2008]. The Spin transfer torque is an effective way of changing the magnetization that is already used as a new writing scheme in memory and logic devices. [Rizzo 2013]

The spin transfer torque can also lead to domain wall motion. The first prediction of current induced domain wall motion was made by L. Berger [Berger 1974]. He proposed that electrons passing through the domain wall can induce a torque which can drag the domain wall along the electron flow direction. However, the first experimental demonstration of this idea was done decades after in 2003[Klaui 2003]. A detailed theoretical model was proposed later [Zhang 2004] [Piechon 2007] [Waintal 2004] [Vanhaverbeke 2007]. The different aspects of these theoretical models are described in the following sections.

I.6.1.1. LLG equation

Two contributions of the spin transfer torque were evidenced both theoretically and experimentally. The first one is called adiabatic spin transfer torque. It comes from the transfer of angular momentum from the spins of the conducting electrons to the magnetization. Here the spins of the conduction electrons adiabatically follow the direction of the local magnetization inside the domain wall. Mathematically the adiabatic component of the STT can be written as

$$\frac{\partial \vec{M}}{\partial t} = -\frac{g\mu_B JP}{2eM_s}\frac{\partial \vec{M}}{\partial x} = -u\frac{\partial \vec{M}}{\partial x}$$

Where g is Lande factor, μ_B is Bohr magnetron, J is current density, P is polarization and M_s is the saturation magnetization.

Considering only the adiabatic contribution, the critical current density for domain wall motion predicted theoretically is much larger than the one observed experimentally [Thiaville 2004] [Klaui 2003]. Another torque called non-adiabatic is needed to describe the experiments. This torque can be written as

$$\frac{\partial \vec{M}}{\partial t} = \beta u\, \vec{M} \times \frac{\partial \vec{M}}{\partial x}$$

Where β is a non-dimensional coefficient that gives the strength of the non-adiabatic torque. The above equation is only valid for small β [Zhang 2004] The physical origin and amplitude of the non-adiabatic contribution have been the subject of numerous studies, both experimental and theoretical (ref). First theoretical studies predicted β equal to the ratio of the spin flip rate over the s-d exchange ($\beta = \tau_{sd}/\tau_{sf}$) [Zhang 2004] [Piechon 2007] [Vanhaverbeke 2007]. More recently microscopic calculations of the spin transfer torque considering the electronic band structure were presented. These calculations find an intrinsic origin to β: the spin orbit interaction [Hals 2009] [Garate 2009]. Qualitatively, this conclusion is the same as this of Zhang and Li since the spin flip frequency increase with the spin orbit interaction that couples spins up and spin down.

According to the Zhang and Li model [Zhang 2004], the slight mistracking between the electrons spins and the local magnetization direction generates a non-equilibrium spin accumulation across the DW. This spin accumulation precesses around the magnetization and relaxes toward the magnetization direction due to spin-flip scattering. These two phenomena lead to both adiabatic and non-adiabatic spin-transfer torques. They found the amplitude of the non adiabatic torque c_j

$$c_j = \frac{\tau_{sd}\tau_{sr}}{\left(\tau_{sd}^2 + \tau_{sf}^2\right)} = \frac{\beta}{1+\beta^2}$$

Where τ_{sd} is the exchange time and τ_{sf} is the spin-flip relaxation time.

Another very important consequence of the spin orbit interaction will be described in the next section 1.7.2: the spin orbit torques.

I.6.1.2 STT driven DW motion:

The complete LLG equation for the current induced domain wall motion including both the adiabatic and non-adiabatic torques can be written as

$$\frac{\partial \vec{M}}{\partial t} = -\gamma \vec{M} \times H_{eff} + \alpha \vec{M} \times \frac{\partial \vec{M}}{\partial t} + -u \frac{\partial \vec{M}}{\partial x} + \beta u \vec{M} \times \frac{\partial \vec{M}}{\partial x}$$

This equation is valid only for small β values according to the Zhang and Li model. It contains four terms. The first two terms give the magnetization variation with respect to the time, where the last two represent the magnetization variation within the space. The first two terms are independent of the current. They represent the precession and damping due to the effective filed in the system, just like the case for the field driven domain wall motion discussed in the section I.5.1. The last two terms are the current driven adiabatic and non-adiabatic torques. They are perpendicular to each other and both perpendicular to the magnetization.

If we consider the magnetization at the center of the domain wall and the regime of low applied current densities, the direction of the effective magnetic field associated with the adiabatic torque is perpendicular to the easy axis while the one associated to the non-adiabatic torque is parallel to the easy axis. The non-adiabatic torque is considered to be responsible for the steady domain wall motion (figure I.18). In a 1D model, the domain wall velocity in the steady state is expressed as $v = \beta u/\alpha$. As the current density is increased the DW undergoes an instability equivalent to the Walker breakdown and the magnetization inside the DW starts precessing. The adiabatic torque is now efficient for DW motion and dominates at higher current densities.

To summarize, the current induced domain wall motion exhibits the same features as those of the field induced domain motion shown in figures I.6 and I.7. The current induced domain wall motion can be steady or oscillatory depending on the current density.

From the application point of view, the usefulness of the current induced DW motion depends on two parameters: the current required for the depinning of the DW and the DW velocity. As discussed in the section I.5.3, the DW can be trapped in the pinning potential created by the imperfections in the sample. Thus, a large current may be required for the depinning of the DW. Initial studies of the STT driven current induced DW motion were

concentrated on NiFe based nanostructures. In these cases, the depinning current is found to be relatively large [Yamaguchi 2004] [Hayashi 2006]. By improving the sample quality, the depinning critical current could be decreased [Meier 2007] [Kläui 2005]. Regarding the DW velocity, it can be increased either by increasing the current density or using the material with large STT efficiency. On the other hand, experimentally, increasing the current density may damage the sample. In the high quality samples of NiFe, with the maximum applicable current density, the STT driven DW velocities up to 100 m/s were observed [Hayashi 2007].

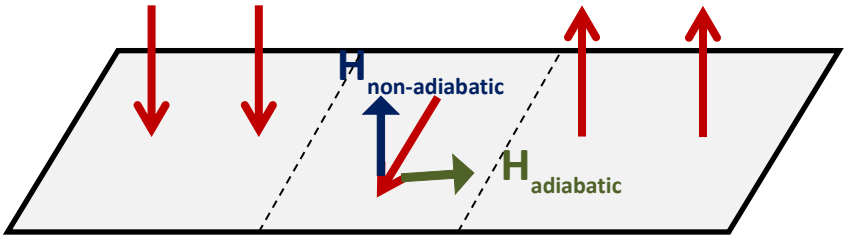

Figure I.8. Schematic diagram of the effective fields acting on the DW magnetization. The effective fields due to the non-adiabatic and adiabatic torques are along easy and hard axis respectively

More recently large DW velocities, too large to be explained by the STT, were observed in systems with structural inversion asymmetry (SIA). Here experiments were done in trilayers made of a thin magnetic layers sandwiched between two different non-magnetic layers. In these samples, the DW motion was against the electron flow in contradiction with the STT model. To explain these observations, additional torque mechanisms were introduced. This will be explained in the next section.

I.6.2. Spin-orbit torques

In the case of STT, the spins of conduction electrons get polarized either by passing through and adjacent magnetic layer, the polarizer, or in the presence of magnetization gradient as DW. Recently it has been shown that spin angular momentum can be transferred to the magnetization from the crystal lattice, through the spin orbit interaction. Due to this origin, the resulting torques on the magnetization are named spin-orbit torques (SOT). Unlike the STT, the SOT does not require magnetic textures nor is its amplitude limited to the maximum spin polarization. As SOTs offer a novel route to manipulate the magnetization and open the way to more efficient spintronics devices, it has been studied widely these last years within the spintronics community.

In the following section, I discuss in details about the different theoretical and experimental aspects related to the spin-orbit torques. At first I explain the structural and symmetry requirements of SOT. Then I will present the history of the experimental evidences of spin-orbit torques. Finally, the influence of SOT on the domain wall dynamics will be discussed.

I.6.2.1. Need of structural inversion asymmetry

In the case of SOT, the magnetization dynamics is manipulated by transferring angular momentum from the crystal lattice. There are two requirements in order to have efficient SOT: the material should have a large spin-orbit coupling and the system should present a structural inversion asymmetry (SIA). Since the electron speed, the Fermi velocity, is close from the relativistic regime, electrons traveling through the non-vanishing electric field will experience in their own frame a magnetic field (H_{SO}) that is perpendicular to both their velocity and the electric field. This magnetic field modifies the spin momentums of the conduction electrons that are further transferred to the local magnetization. The SIA can be either intrinsic to the material, for example in non-centrosymmetric crystal lattice such as zinc-blende crystal structures [Dresselhaus 1955] or provided by specific structure, such as for example asymmetric magnetic multilayers systems [Miron 2010]. In the case where the non-vanishing electric field is induced inside the ferromagnetic material, the SOT can be considered local and originate from the competition between the s-d exchange interaction that tends to align the spins of conduction electrons along the local magnetization and the SOC that tends to align them along H_{SO}. This case is often referred in the literature as the inverse spin galvanic effect [Garate 2010].

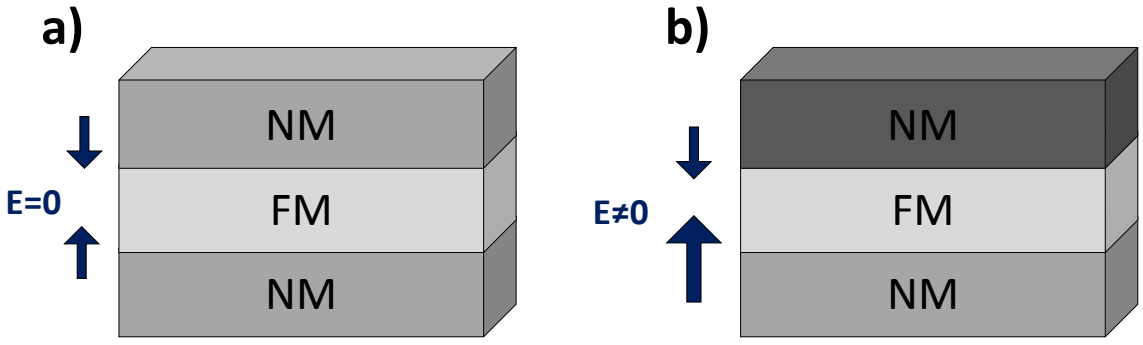

Figure I.9. a) In the case of a symmetric multilayer with a ferromagnetic layer (FM) sandwiched between two identical nonmagnetic layers (NM), the spin-orbit fields I generated in the FM from the presence of the two NM layers cancel each other. **b)** In the case of multilayer with structural inversion asymmetry, the net spin-orbit field in the FM is non-zero

Figure I.9 shows the schematic diagram of the systems that I studied. It consists of a ferromagnetic metal layer (Co in my case) sandwiched in between two nonmagnetic materials (Pt or AlO_x in my case, here one or both of the layer provides large spin-orbit coupling). If the multilayer is symmetric, then the spin-orbit electric fields arising from the two non-magnetic layers cancel each other (figure I.9.a). For the asymmetric multilayers, the net spin-orbit field is finite (figure I.9.b)

It is also possible to inject spins from the adjacent nonmagnetic layer through the spin hall effect[Dyakonov_1971] [Hoffman_2011] (detail explanation will be given in section I.6.2.4.2). Also in this case, the SIA is required. In order to obtain a net torque, spins should be injected only from one side of the ferromagnet. Injection from both sides leads to cancelation. The SOT originates then from a transfer to the local magnetization through the s-d exchange interaction as in the STT case

I.6.2.2. Symmetry of the spin torques

In this section, I will discuss the existence of the SOT from symmetry consideration. I will more specifically emphasize on the importance of the SIA structure and the direction of the SOT. I will study how the torques behave under rotational and mirror symmetry operations.

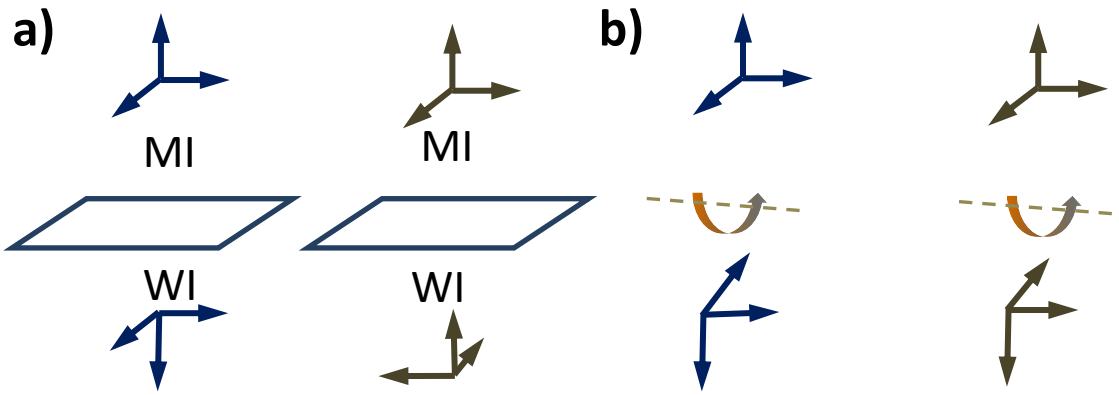

Figure I.10: Schematic diagram of polar (shown in blue) and axial (shown in grey) vectors under symmetry operations. **a)** The mirror symmetry operation. A polar (axial) vector perpendicular to the mirror plane is reversed (unchanged) while it remains unchanged (gets reversed) when parallel to the plane. **b)** The rotational symmetry operation. Here both axial and polar vectors behave the same way. They are reversed when they are perpendicular to the axis of rotation and remain unchanged when they are parallel to the axis of rotation

For a better understanding of the symmetry operations discussed in this section, the mirror symmetry operations for two different vectors need to be distinguished: the polar and axial vectors. As shown in the figure I.10.a, polar vectors (displacement, electric current, etc.) perpendicular to the mirror are reversed, while axial vectors (magnetization, magnetic field, etc.) are reversed if they are parallel to the mirror plan. On the other hand, these vectors behave in the same way under the rotational symmetry operations (figure I.10.b)

I.6.2.3. Symmetry operation on a magnetic domain

Since I have studied perpendicular magnetic materials, all the discussion is based on such system. Consider both a 180° rotational symmetry around an axis parallel to the current direction and mirror symmetry with a mirror perpendicular to the current direction, applied to a uniform magnetic domain. As shown in figure I.11, when there is no current, the whole system including the magnetization (shown in grey arrows) is invariant under the mirror and rotational symmetry operations. Applying current breaks the rotational symmetry, as shown in figure I.11. However, the system remains invariant by the mirror symmetry

Now consider the current creates torques represented by effective fields (represented by red and blue arrows in figure I.11) perpendicular to each other and to the magnetization. Under the mirror operation, both effective fields are changed to their opposite. It means that if such effective fields exist, their opposite fields exist as well resulting in their cancelation

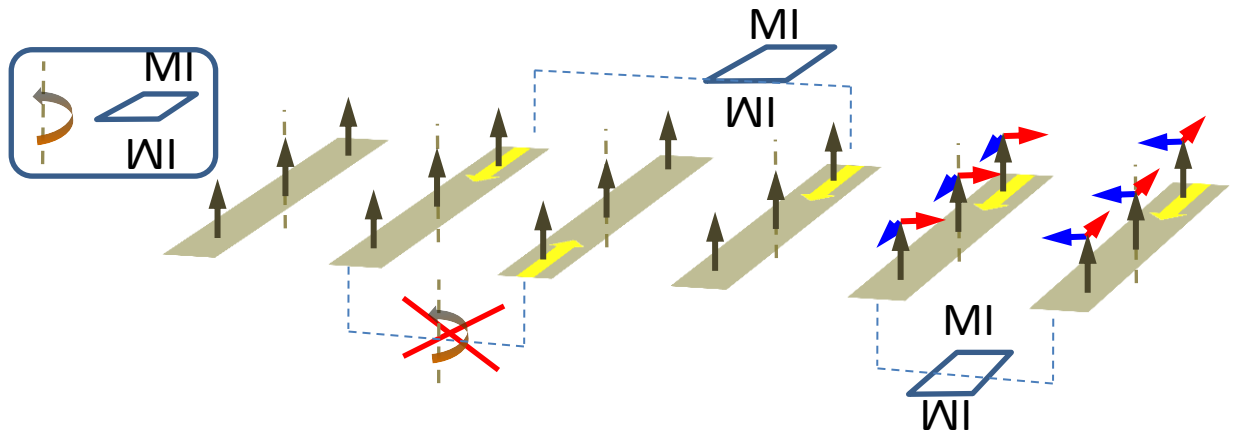

Figure I.11: Schematic diagram of the mirror symmetry with a mirror perpendicular to the current direction, and 180° rotational symmetry around an axis parallel to the current direction, of a uniform magnetic domain. The current injection breaks the 180° rotational symmetry but not the mirror symmetry. If the current could create torques on the magnetization (represented by two effective fields shown in blue and red perpendicular to each other and to the magnetization direction) the mirror symmetry allow the existence of both the effective fields as well as of their opposite resulting in their cancelation.

The picture changes if another parameter is introduced that breaks the mirror symmetry, for example an electric field along the magnetization direction (shown as green arrow in the figure I.12). This electric field breaks the invariance of the system by the mirror symmetry and allows the existence of the SOT. In the scenario of the SOT, the electric field mentioned is created by the lattice (a detailed discussion about this is given in section I.6.2.4

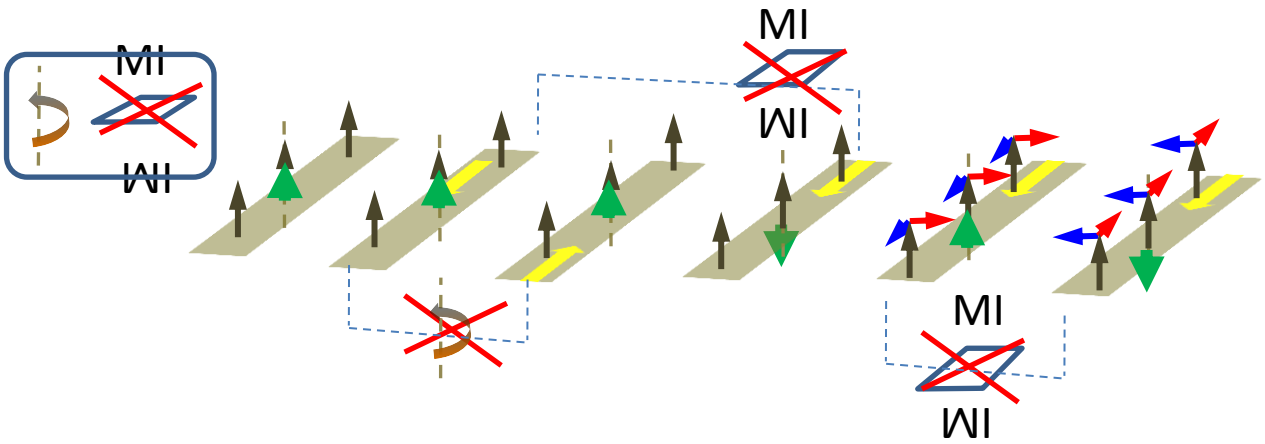

Figure 1.12: In the presence of an additional vertical electric field represented by the green arrow, the mirror symmetry is broken. Then, the existence of an effective field acting on the magnetization does not imply the existence of its opposite. There is no more cancellation and the SOT are allowed.

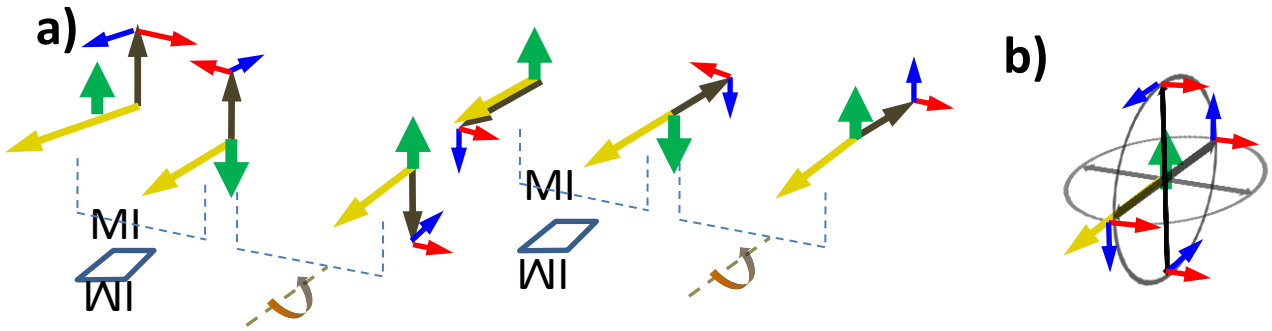

Figure I.13. a) Schematic diagram showing the directions of the current (yellow), magnetization (grey), electric field (green) and effective fields under different mirror and rotational symmetry operations b) Directions of the effective fields deduced from the symmetry operations in figure a for different magnetization directions. One of the effective fields (shown in red) is always aligned along the same direction for all the magnetization directions, while the other is rotating with the magnetization direction (shown in blue)

Furthermore, the directions of the two effective magnetic fields can be obtained as a function of the magnetization direction as shown in figure I.13. Considering a given electric

field and current direction such as represented in figure I.13.a), and starting from an in-plane or an out-of-plane magnetization, the successive application of a mirror symmetry and a 180° rotation around an in-plane axis change the magnetization in its opposite, every other parameters remaining unchanged. The two effective fields acting on the magnetization behave differently. The first one is always oriented in the same direction (shown by red arrows in figure I.13) and is called the field-like component of the SOT. The second one is rotating with the magnetization direction (shown in blue in figure I.13) is called the damping-like component of the SOT. A detailed discussion on these two components will be done in the following sections

To summarize, the breaking of vertical symmetry is necessary for the existence of the SOT. The symmetry arguments discussed here only show that the torque can exist, but it is not a proof that they actually exist, nor it gives any information on their amplitude and the role of the material and structural parameters.

I.6.2.4. The field like and damping like torques:

As explained in the section I.6.1.2, the STT contain two terms: the adiabatic and non-adiabatic torques. This two components act in two perpendicular directions with respect to the magnetization. Similarly, the SOTs are composed of two components: the field-like torque (T_{FL}) and the damping-like torque (T_{DL}). These torques and their effective fields can be written as

$$T_{FL} \sim \vec{m} \times (\hat{z} \times j) \qquad \& \qquad H_{FL} \sim \hat{z} \times j$$

$$T_{DL} \sim \vec{m} \times (\vec{m} \times (\hat{z} \times j) \qquad \& \qquad H_{DL} \sim \vec{m} \times (\hat{z} \times j)$$

Where z is the direction perpendicular to the plane of the sample and j the current density. In the following section, I will discuss in details the various theoretical and experimental studies that have been performed to understand these two torque components as well as their microscopic origins.

I.6.2.4.1.The field like term

As its name suggests, the field-like torque acts as if there were an external magnetic field applied to the system. The first experimental observation of the current induced SOT in ferromagnetic metallic layers was done by I. M. Miron *et al*. [Miron 2010] using Pt/Co/AlOx multilayer system. In this study, they showed that magnetic domain nucleation can be

modified by the presence of an effective magnetic field in-plane and perpendicular to the current direction.

In this experiment, a Pt/Co/AlO_x trilayer was patterned into 20 parallel wires and the current-induced nucleation was observed by MOKE microscopy. Starting from a down saturated magnetic state, a current applied into the wires results in the nucleation of up domains (in black in the figure I.14, first raw). When an in-plane external field (H_{ext}) is superimposed, the domain nucleation behaves asymmetrical depending on the relative directions of the current and H_{ext}: for a given current direction, the nucleations disappear for one magnetic field direction and increases for the other. Inversing the current direction requires reversing also the external field direction in order to observe the same behavior. The same experiment was repeated in Pt/Co/Pt symmetric multilayers. In this case no asymmetric nucleation was observed pointing the necessity of having a SIA.

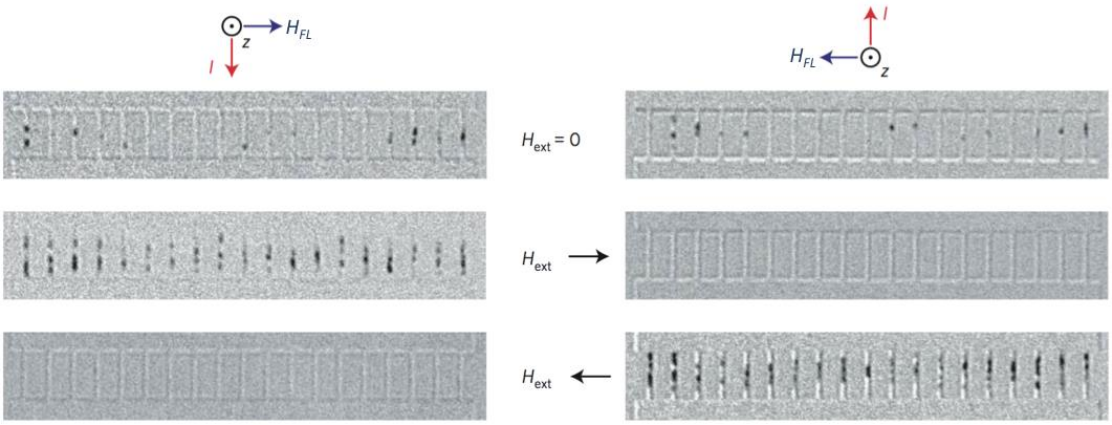

Figure I.14. Observation of the asymmetric domain nucleation experiment done on Pt/Co/AlOx wires [Miron 2010]. The MOKE microscopy images of the domain nucleations in an array of wires are shown, where the black color contrast represents the nucleated domains. For a constant current (I) direction, the nucleations can be increased or suppressed depending on the external field (H_{ext}) direction. This is interpreted as evidence of the presence of the field-like torque (H_{FL}) perpendicular to the current directions that either adds or subtracts to H_{ext}. For an opposite current, the action of H_{ext} on the domain nucleation is opposite. H_{FL} produced by the current changes sign.

This change in the domains nucleation was interpreted as an evidence of the existence of a magnetic field (H_{FL}) in-plane and perpendicular to the current direction. Thus when H_{ext} is applied the energy barrier for domains nucleation becomes smaller (higher) if it is anti-parallel (parallel) to H_{FL} resulting in an increase (a reduction) of the domains nucleations (figure I.15b).

The conduction electrons were claimed to feel a magnetic field originating from the spin-orbit coupling, perpendicular to the drift velocity, the current direction, called the Rashba field (H_R). Hence the spins of the conduction electrons are submitted to both H_R and the s-d exchange interaction and a torque is exerted on the magnetization. The effective field associated to this torque is called H_{FL}. This result confirms the existence of H_{FL} predicted by Manchon and Zhang [Manchon 2009] The quantitative study of these asymmetric nucleations showed that the amplitude of the H_{FL} can be remarkably large ($1T/10^8$ A/cm²). However, this value was overestimated due to the measurement principle and particularly the role of the thermal energy. Much lower values are reported for this system [Pi 2010] [Garello 2013]

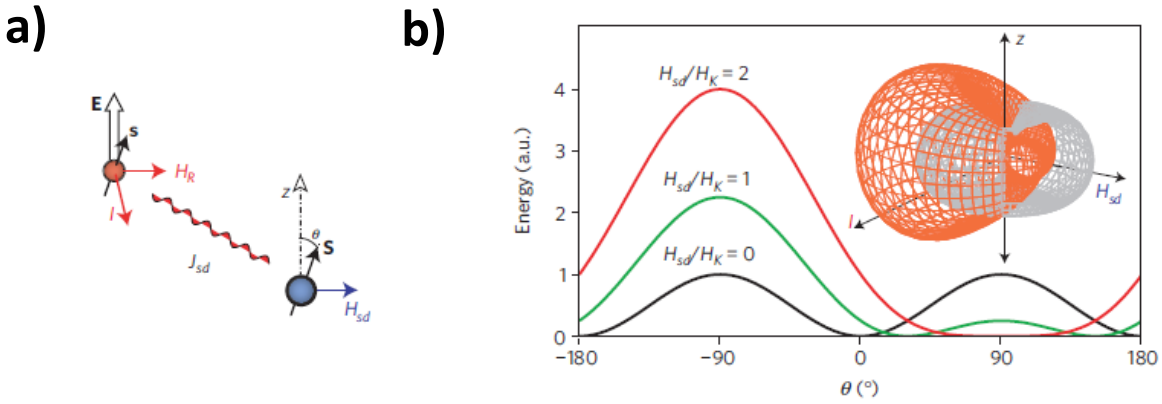

Figure I.15 a) The spin of the conduction electrons are submitted to both the Rashba field (H_R) and the s-d exchange interaction. A torque is then exerted on the localized moments resulting in an effective field (H_{sd} or H_{FL}) in the plane of the sample and perpendicular to the current direction. **b)** The 3-D contour represents the energy required for the magnetization reversal in presence (shown in orange color) and absence (shown in grey color) of H_{sd}. The graph shows the variation of the magnetic energy with respect to the polar angle (θ) for different H_{sd}/H_k ratios, where H_k is the anisotropy field. In the absence of H_{sd}, the graph is symmetric with respect to the angle θ=0 (black curve). When H_{sd} is introduced the energy becomes asymmetric with θ and the energy barrier for nucleating a domain is decreased (green curve). Eventually it disappears for H_{sd} larger than H_K (red curve) [Miron 2010]

Following this work, numerous experiments were reported confirming the presence of H_{FL} in different asymmetric multilayers such as Ta/Pt/Co/AlO_x [Pi 2010] ,Ta/CoFeB/MgO [Suzuki 2011] [Kim et al., 2012] using different magnetic characterization techniques such as anomalous Hall effect Later K. Garello *et al.* proposed a general method to measure the SOTs based on the harmonic analysis of planar and anomalous Hall effects [Garello 2013] . Using this method, the presence H_{FL} in different multilayer systems was confirmed.

I.6.2.4.2. Damping like term

In 2011, the second component of SOT: the damping-like torque (T_{DL}) was observed in in-plane magnetic Pt/NiFe multilayers [Liu 2011]. Here the authors demonstrated that the spin hall effect in Pt can excite the magnetic precession in the adjacent ferromagnetic film (NiFe). This experiment was done using the ferromagnetic resonance (FMR) measurements. Later I. M. Miron *et al.* evidenced the same kind of torque components in Pt/Co/AlOx [Miron 2011]. In their experiment, they demonstrated that due to the presence of this damping-like torque, a perpendicularly magnetized ferromagnetic dot can be switched under an in-plane current injection

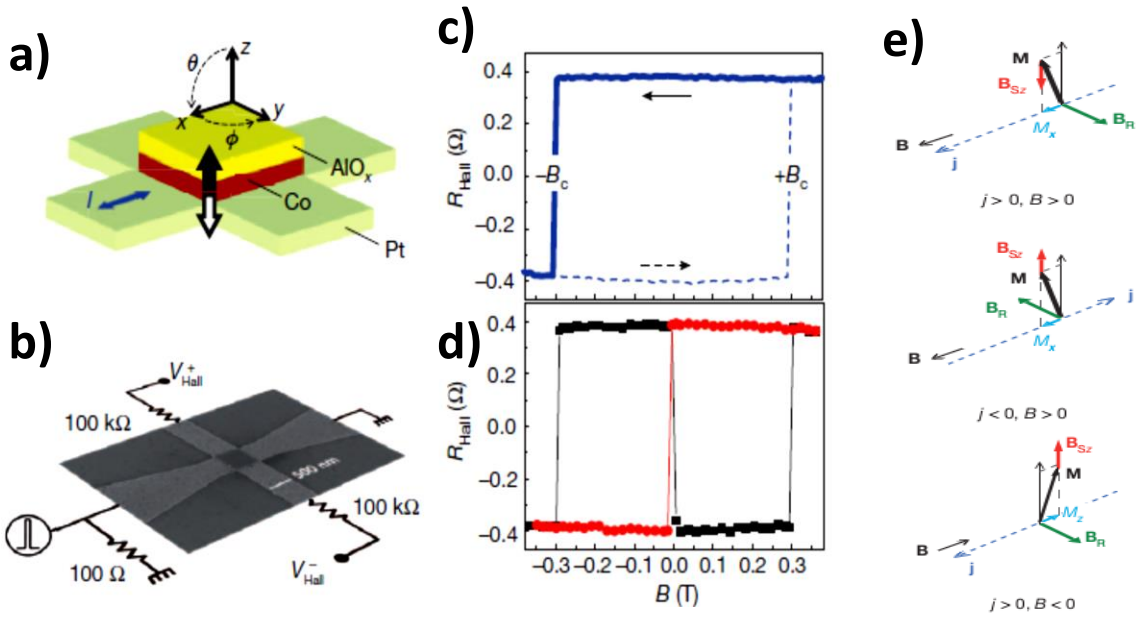

Figure I.16. a) Schematic diagram of the geometry used for the switching experiment: a Co/AlOx dot sitting on a Pt Hall cross. **b)** Scanning electron image of the sample with a schematic of the electric circuit used for the extraordinary Hall effect measurement. **c)** Hall resistance (that represents the M_z component) of the Co dot versus the external magnetic field amplitude (B) applied nearly in-plane (2° from the plane). The switching field (B_c) was around 0.3 T. **d)** Mz measured after the injection of positive (black) and negative (red) current pulses applied along with B, as a function of B amplitude e) Schematic of the direction of the switching field (B_{sz}) depending on the directions of the current (j) and field (B) for the case of Pt/Co/AlO$_x$. When both j and B are in same direction (j>0, B>0 or j<0, B<0), B_{sz} is oriented downwards, while for j and B opposite to each other (j>0, B<0 or j<0, B>0) B_{sz} is upwards [Miron 2011].

The experiment was performed on a 500x500 nm $Co_{0.6}$AlOx dot sitting on a Pt_3 Hall cross. Here an in-plane current (j) was injected in the presence of an in-plane magnetic field (B). M_z was measured using the extraordinary Hall Effect (EHE) [Gerber 2002] signal. At

first M_z was first measured as a function of B applied nearly in-plane (tilted 2° from the plane). The coercive field (B_c) was found around 300 mT. The injection of positive (resp. negative) in-plane current pulses results in the switching of the magnetization from up to down (resp. down to up) for negative B and down to up (resp. up to down) for positive B in the entire field range delimited by the coercive field

These experiments showed that a current injected in-plane creates a torque acting on the magnetization. This torque is equivalent to an effective field acting on the magnetization $\mathbf{B_{sz}} \sim (\mathbf{z} \times \mathbf{j}) \times \mathbf{B} \sim (\mathbf{z} \times \mathbf{j}) \times \mathbf{M}$ since **B** determines the initial magnetization (**M**) direction (figure 1.16). Eventually, this torque switches the magnetization. As we already discussed above, two mechanisms were proposed to account for the spin accumulation at the origin of this torque: the the ISGE or Rashba effect here, arising at the heavy metal/ ferromagnet interface and the spin hall current produced in the bulk of the heavy metal.

Concerning the first mechanism, an out of plane polarization had already been observed in presence of a longitudinal magnetic field in InGaAs [Kato 2004]. The Rashba field ($\mathbf{B_R} \sim (\mathbf{z} \times \mathbf{j})$) acting on the conduction electrons, produces a non-equilibrium spin accumulation ($\mathbf{s_R}$) along its direction. $\mathbf{s_R}$ will precess around **B** while $\mathbf{s_B}$ created by **B** will precess around $\mathbf{B_R}$ (figure 1.17). If both $\mathbf{B_R}$ and **B** were "real" magnetic fields, the two precessions will cancel each other. However, $\mathbf{B_R}$ is not a real magnetic field and depends on the electrons mobility. In the case of anisotropic scattering on impurities or non-parabolic energy band, spins up and spins down will experienced a different spin accumulation. Eventually, a perpendicular spin accumulation will build up [Engel 2007] [Miron 2011 Sup].

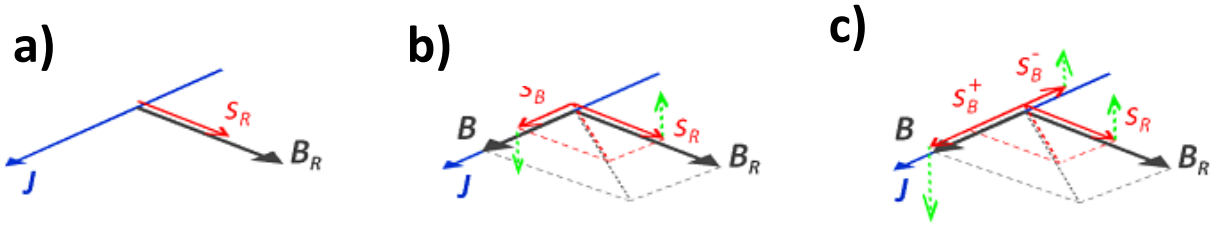

Figure 1.17. Schematic diagrams of **a)** Spin accumulation (S_R) due to the Rashba field, (B_R) **b)** The spin accumulation (S_B) due to the field B. The green arrows shows the torque acting on S_R and S_B. **c)** The spin polarization due to B is the sum of majority (S_B^+) and minority components(S_B^-). The different torque acting on these two components produces a net uncompensated perpendicular torque [Miron 2011 Sup].

The second mechanism that can produce this torque is the spin hall effect (SHE). A current is injected in heavy metals the spin orbit coupling induces a transverse spin current. If the translation symmetry is broken by the presence of an interface, a spin accumulation will be created at this interface. The direction of the spins is parallel to the interface and perpendicular to the current direction (figure 1.18a). Different mechanisms were identified to explain this phenomenon. On one hand spin dependent scattering on a nonmagnetic impurity can modify the incident wave vector by the Mott scattering mechanism, this is the "skew scattering" phenomenon [Smit 1958] or shift the wave function, the "side jump effect" [Nagaosa 2010] [Berger 1970] (figure 1.18 b&c) On the other hand, its origin can be intrinsic, due to the band structure [Karplus 1954] [Luttinger 1958] [Murakami 2003] [Murakami 2004] [Sinova 2004] [Inoue 2004] [Kontani 2007] [Tanaka 2008]. The strength of the SHE is expressed by the parameter called the spin Hall angle θ_{SHE}, the ratio between the amplitudes of the transverse spin current and longitudinal electric current. If a magnetic material is brought in contact, this spin accumulation will flow in this material. The absorption of the transverse part of this spin current creates this torque as in the STT mechanism [Ando 2008] [Liu 2011] and be absorbed.

This particular term of the SOT that is rotating with the magnetization and that causes the switching is called the damping like torque ($\mathbf{T_{DL}}$) and the corresponding effective field will be written as $\mathbf{H_{DL}}$ in the following.. $\mathbf{H_{DL}}$ can be written as ($\mathbf{H_{FL}}$) x $\mathbf{M}$. since the field-like component $\mathbf{H_{FL}}$ is proportional ($\mathbf{z}$ x $\mathbf{j}$): $\mathbf{H_{DL}}$ is always perpendicular to $\mathbf{H_{FL}}$ and to the magnetization as we already noticed above.

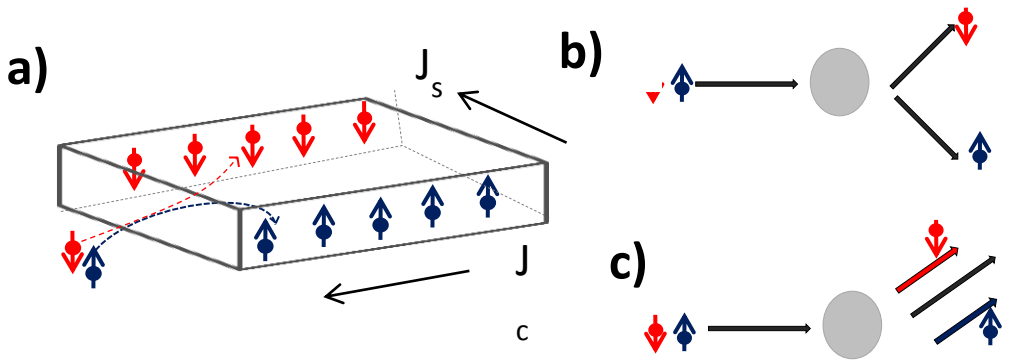

Figure I.18. The schematic diagram of a) the formation of transverse spin accumulation in heavy metal b,c) The two mechanism that causes the spin hall effect: b, the skew scattering where the two spins are scattered due to the spin orbit interaction with an impurity. c, the side jump mechanism due to the spin dependent wave function modification.

Considerable theoretical and experimental work is dedicated to separating the Rashba and SHE contributionsto the $\mathbf{H_{FL}}$ [Wang 2012] [Kim 2012] [Freimuth 2013] [Haney 2013] [Ortiz 2013]. However, since both effects have the same spin-orbit coupling origin, changing any material parameter can cause changes in both effects. Thus the experimental separation of these two contributions is difficult and the exact contribution of the two effects still under debate.

I.6.2.5. Current induced DW motion in PtCoAlOx – Limitations of the STT model

I.6.2.5.1. Large velocities without any Walker breakdown signature

In 2011, I. M. Miron *et al*. reported very fast domain wall motion in Pt/Co/AlOx nanowires [Miron 2011]. In this experiment, a Pt/Co/AlOx trilayers was patterned into twenty 500nm wide, 20µm long nanowires. CIDW motion was studied using wide field Kerr microscopy. As shown in figure I.19, high domain wall velocities up to around 400 m/s were reported for current densities of some 10^{12} A/m^2. This domain wall velocity is much larger than the expected DW velocity in the oscillatory regime, even at the limit of full spin polarization (P=1). Moreover, the equivalence between the action of the current and the field that can be extracted from fast current and field induced DW motion (figure I.19.b) is the same as the one obtained in the quasi-static case [Miron 2009].Thus the domain wall motion observed here seems to correspond to the steady state motion and involves a large β value since the velocity is proportional to $\beta u/\alpha$

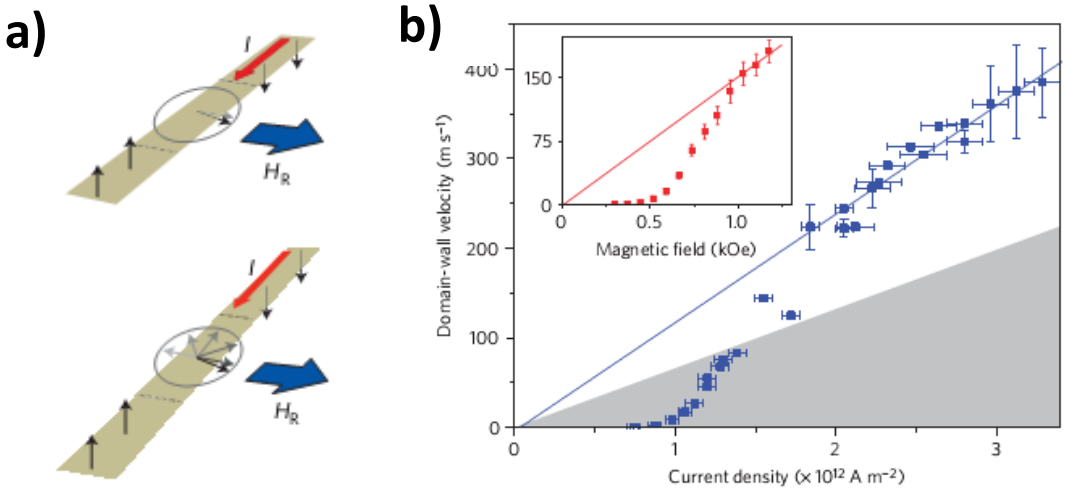

Figure I.19. a) Schematic diagram of the action of the field-like term of the SOT, named H_R for Rashba field in this publication, on the magnetization inside the domain wall. H_R acting perpendicular to the current stabilizes the DW structure against the DW structure transformation that causes the oscillatory motion**. b)** DW velocity with respect to the current density. A high current induced domain

wall velocity up to 400m/s is reported here. The DW velocity vs the applied magnetic field is represented in the inset [Miron 2011].

However, the Walker breakdown current is inversely proportional to β ($\sim[1-\beta/\alpha)]^{-1}$) [Mougin 2007]. A large β shifts the Walker breakdown to lower currents whereas no Walker instability is observed experimentally. The Rashba field (H_R) was proposed in this work to stabilize the DW structure. It acts along the magnetization in a Bloch DW structure and stabilizes its chirality by preventing the magnetization to precess (figure I.19.a). Thus, the high mobility regime is maintained up to large current densities

I.6.2.5.2. DW motion against the electron flow

Besides this large velocity, I. M. Miron *et al.* reported that the direction of the domain wall motion is against the electron flow (or in the direction of the current flow), opposite to what is expected from standard STT model. Two possible scenarios were proposed in the framework of this model. 1) Both the adiabatic and the non-adiabatic torques are negative. This could happen with a negative spin current polarization [Šipr 2008] [Lee 2010] 2) The non-adiabatic torque is negative while the adiabatic torque is positive. A negative β value could account for this situation and cause a DW motion in the direction of the current flow only below the Walker breakdown. If the adiabatic torque would be negative and the non-adiabatic torque positive, the DW motion will be opposite to the electron flow direction only below the Walker breakdown. Even if negative β values have been predicted [Garate 2009] the explanation has evolved since this publication, taking into account now the role of the damping like term of the SOT.

In 2012 A. Thiaville *et al.* [Thiaville 2012] proposed a new mechanism combining the damping-like torque of the SOT and the antisymmetric exchange originating from the spin-orbit coupling called the Dzyaloshinskii-Moriya interaction (DMI). This mechanism explains the direction of the DW motion as well as the very large velocities without any Walker breakdown signature. This new mechanism is explained in details in the following section.

I.7. Dzyaloshinskii Moriya interaction

The Dzyaloshinskii Moriya interaction (DMI) is an antisymmetric exchange interaction first predicted by [Dzyaloshinskii]. It has been first proposed in bulk materials lacking space inversion symmetry [Moriya 1960] and later evidenced at the interface between the magnetic thin films and adjacent layer with high spin orbit coupling [Fert]. In the latter case, DMI originates 3 site indirect exchange interaction between two neighboring atomic spins mediated by an atom that has large spin-orbit coupling, located in an adjacent layer. A schematic diagram of this interaction is shown in the figure I.20.a [Fert 2013] , where the

interaction between the two neighboring spins S_1 and S_2 is described by the DMI vector (D_{12}) perpendicular to (S_1S_2). The DMI interaction can be written as: $\mathbf{H_{DMI} = D_{12}.(S_1 \times S_2).}$

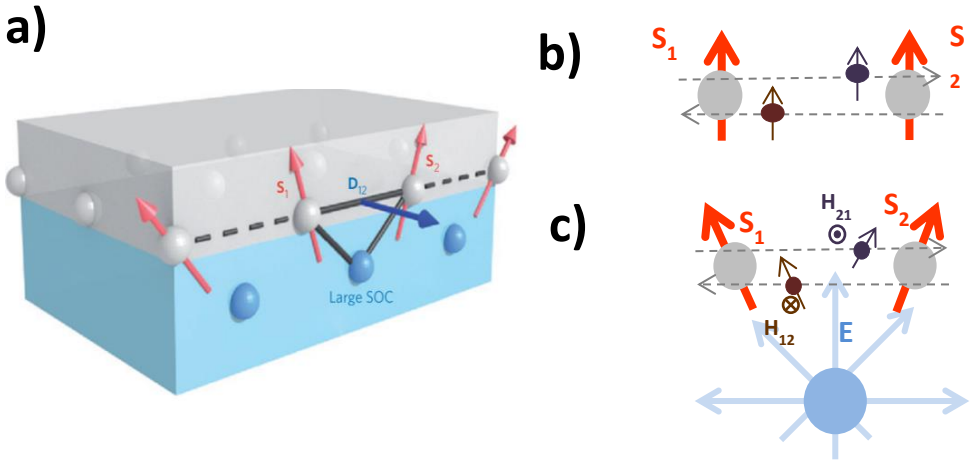

Figure I.20. a) Schematic diagram of the Dzyaloshinskii Moriya interaction at the Ferromagnetic/ Heavy metal interface. The spin S_1 and S_2 are coupled through a heavy metal atom**. b)** The schematic diagram of the two virtually travelling electrons between two neighbouring spins S_1 and S_2. **c)** In the presence of a non-zero crystal fieI(E), the spins of the travelling electrons feels perpendicular magnetic field in its own frame of reference and they precess. This cause the rotation of the atomic spins S_1 and S_2.

The DMI can induce spin textures with specific chirality of rotation. Figure I.20 b&c shows the formation of such rotation between two neighboring spins S_1 and S_2. Consider that two electrons virtually travelling between the two spins (Figure I.20 b). In the presence of a heavy metal atom that provides a non-compensated crystal Ild (E), the moving electron feels a magnetic field perpendicular to it. Here, the two virtual electrons moving opposite to each other feel opposite magnetic field (H_{12} and H_{21}). Therefore, they precess opposite to each other around the respective magnetic fields. Then due to the exchange interaction, the spins S_1 and S_2 get tilted to the electron spin direction (figure I.20).

In magnetic multilayer system with large spin orbit coupling, the DMI can induce chiral DW structure. This is described in the next section.

I.7.1. Chiral DW structures due to DMI

The magnetization of the two adjacent DWs can have same or different chirality of rotation. If the sense of the magnetization rotations (clockwise or anticlockwise) of the two adjacent DWs (up/down and down/up) are the same, they are called homochiral DWs (figure 1.21.a). In a magnetic system, both chiralities are equally probable unless there is an additional mechanism that fixes the chirality of the magnetization rotations.

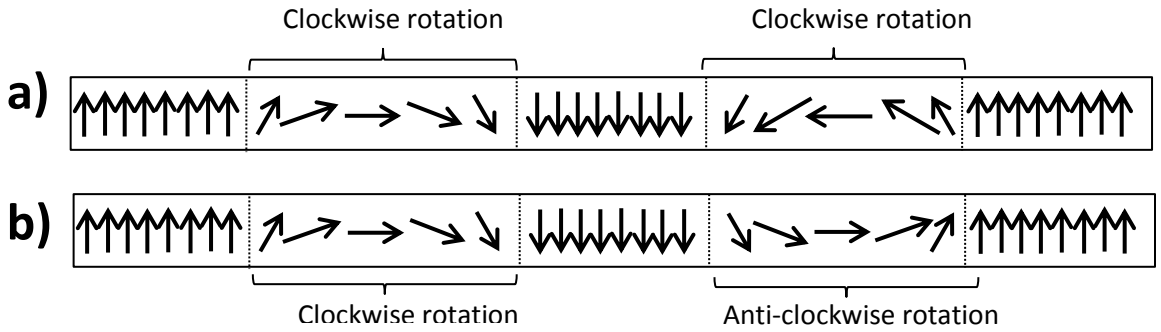

Figure I.21. The schematic diagrams of the rotations of the magnetizations inside the domain wall when **a)** the chiralities of rotation are same and **b)** they are different. In the case of the homochiral domain walls, magnetizations of both up/down and down/up domain walls rotate clockwise; where for the second case the rotations are opposite.

In magnetic thin films with perpendicular anisotropy, the large magnetocrystalline anisotropy energy favored the Bloch DW structure: DW is thin so that the demagnetizing energy of the DW is less if the magnetization inside the DW is oriented along the DW (Bloch structure) than perpendicular to it (Néel structure). The DMI favors a tilt between two adjacent moments. For amplitudes small enough to keep the ferromagnetic order, it affects mainly the "weak" points, the DW. In fact, if the DMI has to compete with the magnetocrystalline anisotropy to destabilize the magnetic order, in the DW it competes with the demagnetizing energy, which is much lower. The DMI can then induce a chiral Néel DW structure: two consecutive DWs will have their core magnetization opposed to each other [Thiaville 2012].The presence of a chiral Néel wall is important in the DW dynamics because the action of the SOT on the DWs largely depends on its structure.

I.7.2. SOT driven current induced DW motion in presence of DMI

The study of current assisted DW depinning by P.P.J. Haazen *et al.* [Haazen 2013] showed that the damping like (DL) component of SOT is efficient in moving the DW motion if this DW has a Néel component. In this study, an in-plane field was used to create such Néel component. The action of the DL torque depends on the DW structure. As shown in figureI.22.a and b, if the DW has a Bloch structure, the magnetization in the DW is aligned with the H_{FL} and the DL torque is zero. In the case of a Néel DW structure, since the magnetization is perpendicular to H_{FL}, the DL torque can be very efficient is moving a DW since H_{DL} is maximal. However, in the case where two consecutive DWs (up/down and down/up) are aligned along the same direction as in the experiment of Haazen *et al.*, [Haazen 2013] they feel the same effective field H_{DL} and the two DWs move opposite to each other

(figure I.22.c). This points the important role of the DMI in the mechanism proposed by Thiaville *et al.* [Thiaville 2012]. Since this interaction promotes a chiral DW, the in-plane magnetizations inside two consecutive DWs are opposite to each other. They feel opposite effective magnetic field H_{DL} and the two DWs move in the same direction. To summarize, in this mechanism, the DMI provides the proper conditions for the DL of the SOT to be efficient for current induced DW motion.

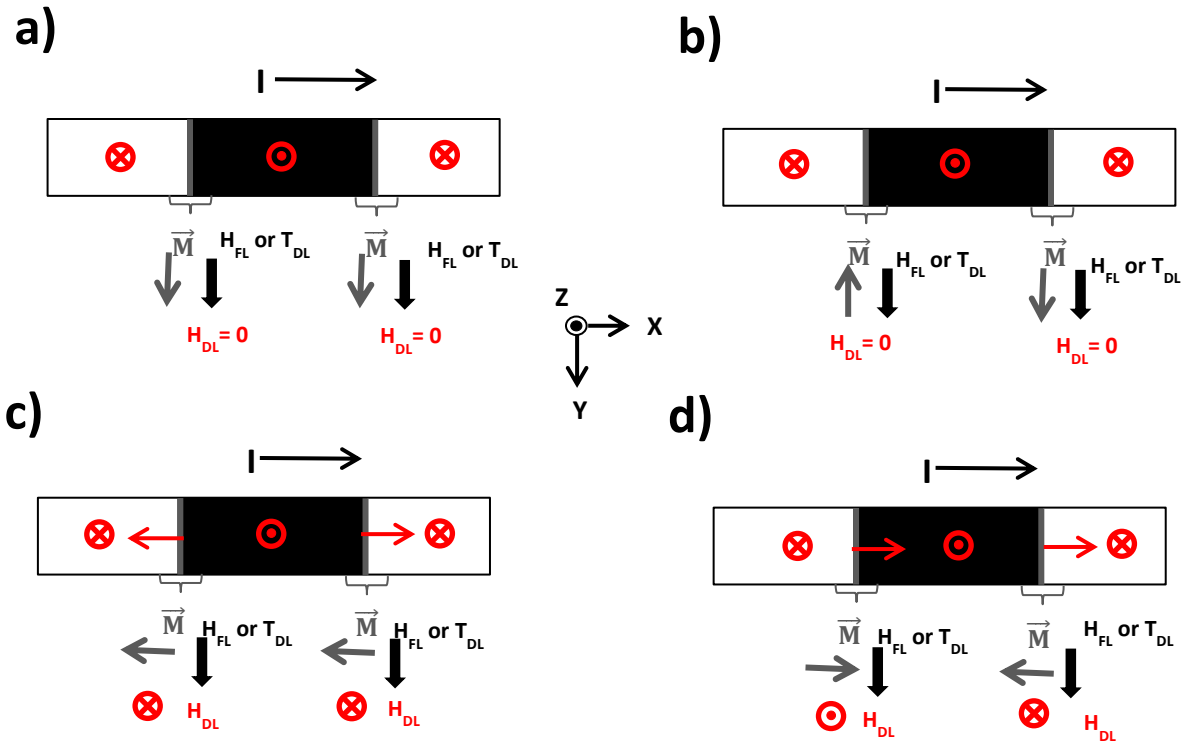

Figure I.22: Schematic diagram of the action of SOT on different domain wall structures. The magnetization at the center of the domain wall is represented by a grey arrow**.** The direction of DW motion is represented by the red arrows. **a, b)** $\mathbf{T_{DL}}$ acting on non-chiral and chiral Bloch walls. In both cases, the magnetization is aligned with $\mathbf{H_{FL}}$ and $\mathbf{H_{DL}} \sim (\mathbf{M} \times \mathbf{H_{FL}}) = \mathbf{0}$. No DW motion is observed. **c)** T_{DL} acting on a non-chiral Néel DW. The magnetization inside the down/up and the up/down DWs are directed along the same direction. Thus H_{DL} is the same for both DWs, for example upwards, and the up magnetic domain expands. Up/down and down/up DWs are then moving in directions (shown by the red arrows) opposite to each other. **d)** In the case of a chiral Néel DW, H_{DL} acting on down/up DW is downwards resulting in the expansion of the down magnetic domain, whereas H_{DL} acting on up/down DW is upwards resulting in the expansion of the up magnetic domain. Thus the two adjacent domain walls move along the same directions.

I.7.3. The direction of DW motion

The signs of the DMI define the chirality of the DW: right handed Néel DW for DMI>0 (the magnetization inside the DW rotates clockwise) or left handed chiral Néel wall for DMI<0 (the magnetization inside the DW rotates anticlockwise). This sign is defined by the material properties and the multilayer composition. Similarly, depending on the multilayer system, the DL torque can be either positive or negative. These two parameters give four possible combinations; two of them move the DW along the current directions while the other two move the DW against the current directions. As shown in figure I.23, for a left handed Néel wall (DMI<0) and a DL torque acting along the positive direction as well as for a right handed Néel wall (DMI>0) and a DL torque acting along the negative direction, the DWs move along the current direction. The other two combinations result in the DW motion against the direction of the current.

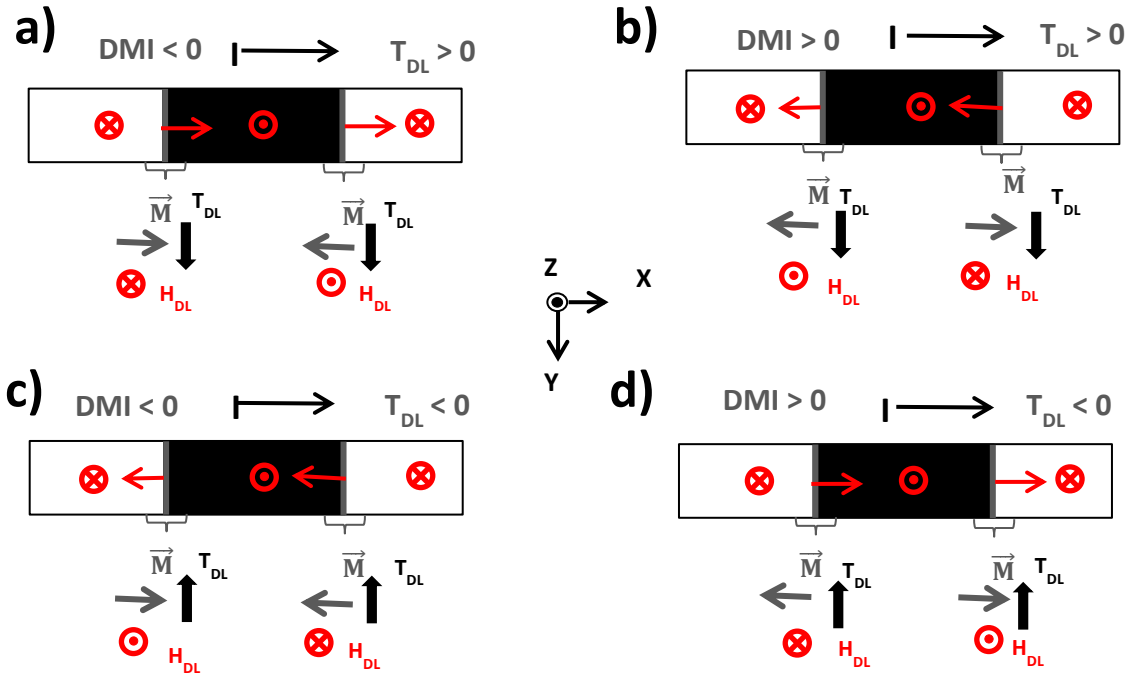

Figure I.23: Schematic diagram showing the direction of the effective field acting on the domain wall for different DMI and damping like torque (T_{DL}) signs. This effective field defines the direction of the DW motion. For DMI< 0, the DW is a left handed Néel wall and the magnetization inside the DW (shown by grey arrows) is directed towards the up magnetic domain. For DMI>0, the magnetization is directed towards the down magnetic domain. **a)** DMI<0 and T_{DL} is positive (along the +Y direction), **b)** DMI>0 and $T_{DL}$is positive, c) DMI<0 and T_{DL} negative d) DMI>0 and T_{DL} negative For cases **c)** and **d),** the DWs move in the direction of the current (shown by the red arrows) while for cases b) and c), the DW motion is opposite to the current.

To summarize, according to the DMI+DL torque model, depending on the multilayer system, the current can move the DW along its direction or against it. Then, the puzzling issue raised by the observation of DW moving along the courant direction in certain multilayers such as Pt/Co/AlOx, can be naturally solved within the framework of this model.

1.7.4. Experimental proof of the existence of DMI induced chiral Néel wall

The first experimental evidences of the presence of the DMIin multilayers systems and of its role in the DW motion were indirect. Ryu *et al.* [Ryu 2013] and Emori *et al.* [Emori 2013] measured the DW current induced domain wall velocity in the presence of an in plane field respectively on Co/Ni multilayers and on Pt/CoFe/MgO and Ta/CoFe/MgO. The in-plane longitudinal field (H_x) modifies the DW velocity. As show in figure I.24, depending whether H_x is parallel or antiparallel to the current direction, the up/down (resp. down/up) DW velocity will increase (resp. decrease) or vice versa. This indicates that the magnetizations inside two consecutive DWs are opposite to each other. Moreover, at a certain applied field, the domain wall velocity becomes zero, for example, in figure I.24, the up/down DW at a negative in-plane field and the down/up DW at positive in-plane field. This field is considered as the field that reverses the DW from a Néel structure to a Bloch structure. It is the field required to overcome the DMI field inside the domain wall.

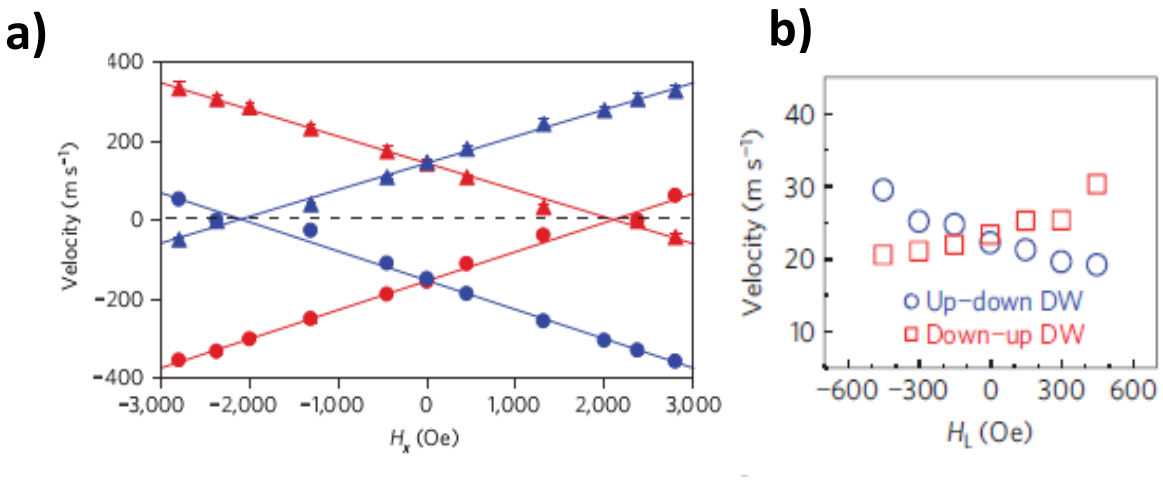

Figure 1.24: a) Domain wall velocity versus an in-plane field (H_x) applied along the current (the x direction) for a positive current (triangles) and a negative current (circles) in Co/Ni multilayer system by Ryu *et al* [Ryu 2013] The velocity of up/down and down/up domain walls is shown in blue and red respectively. The up/down DW velocity becomes zero at around H_x = -2kOe and the down/up DW velocity at around H_x = +2kOe. This field is considered as the field that transforms the Neel wall into a Bloch wall **b)** The same kind of measurements performed by in Pt/CoFeB/MgO [Emori 2013]

After these first results, numerous studies were focused in obtaining direct evidence of the presence of a Néel wall as well as quantitative measurements of the DMI. Direct imaging of a chiral Néel DW was reported using different microscopy techniques. G.Chen *et al.* [Chen 2013] first observed chiral Néel DWs in Co/Ni based multilayers using SPLEEM. However this technique is limited to model samples such as bare magnetic surface obtained typically by molecular beam epitaxy. The debate remained then open for "standard" samples obtained by sputtering such as the trilayers with SIA. J. P. Tetienne *et al.*, [Tetienne 2014] using a scanning nanomagnetometry based on nitrogen-vacancy defect in a diamond tip, evidenced a chiral Néel DW in Pt/Co/AlOx and a Bloch DW in Ta/CoFeB/MgO.

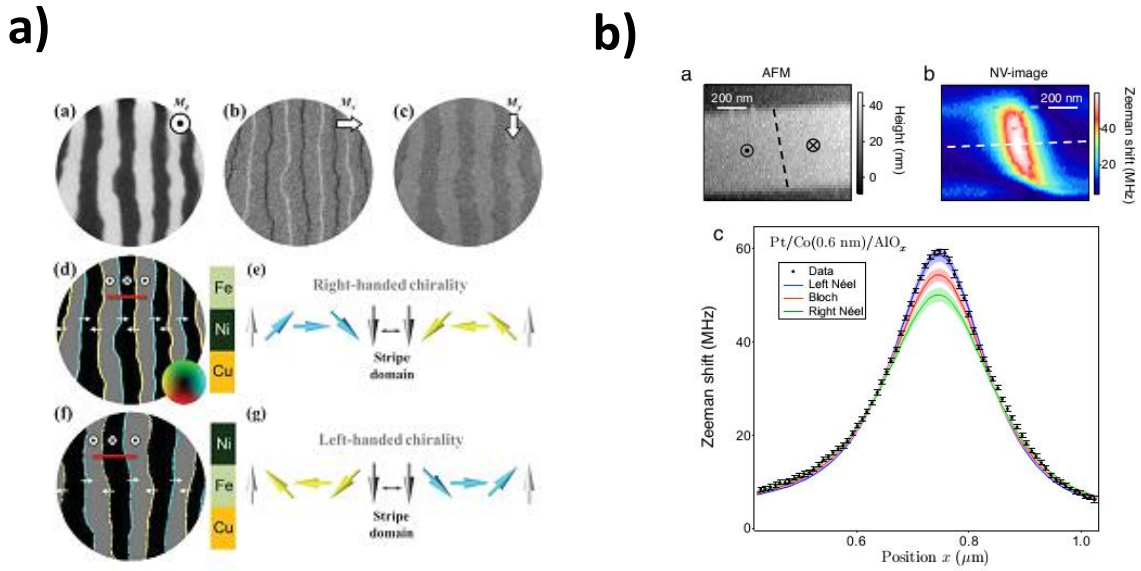

Figure I.25: a) The DW imaging in Fe/Ni/Cu by G.Chen *et al* using SPLEEM [Chen 2013]. The magnetization components along X,Y&Z direction (M_x, M_y, M_z) are shown on the top. The mapping of the DW structure is shown below where the blue and yellow colors show the direction of the in-plane magnetization inside the DW. For Cu/Ni/Fe and Cu/Fe/Ni they observed opposite chirality. **b)** The measurement done by J. P. Tetienne *et al* in Pt/Co/AlOx. [Tetienne 2014]AFM and scanning nanomagnetometry images are shown on the top. In their technique, the Zeeman shift due to the stray field from the DW was measured. Below, the graph containing the comparison of the experimentally measured Zeeman shift with the theoretical model is shown. The experimental results fit with theoretical curve for Left chiral Néel wall structure.

Even though all these experiments partially indicate the presence of the DMI in DW, a universal direct method for the accurate measurement of the DMI is still to be established. Very recently, a new way to measure the DMI field (H_{DMI}) is proposed using the asymmetric field induced bubble domain expansion method [Je 2013] [Hrabec 2014]. During my Ph.D, I

have observed incompatibilities of this method. The details of this method and further discussion on the influence on the influence of the DMI in DW dynamic will be done in chapter III.

I.8. Conclusion

The goal of this chapter was to introduce the basic concept behind the magnetic DWs and their dynamics.

At first, I explained the different magnetic energies and how they lead to the formation of magnetic domains and DWs. Then the different magnetic DW structures were discussed.

After this, I have discussed about the DW motion. DW in a magnetic structure can be moved by two ways (1) with a magnetic field (2) by applying spin polarized current. At first I explained about the basic physics behind the field induced DW dynamics based on the LLG equation. Then two current induced torques mechanisms, STT and SOT, were discussed. Since our experimental studies were mainly concentrated in magnetic systems with large spin orbit interaction, a thorough understanding of the SOT is required to understand our results. Therefore in this chapter, special importance was given to the discussions on the various aspects behind the SOT mechanism.

Finally, the importance of the DMI in the DW dynamics was discussed. Here, the various experimental studies proving the existence of the DMI were discussed.

The first experimental evidence of the existence of the SOT in ferromagnetic multilayers systems was shown 5 years ago. Within the short span of time, the SOT has emerged as one of the hot topics in the spintronics research community. As discussed in this chapter, the various studies were performed to improve the fundamental understanding behind SOT. As well as, the new magnetic device concepts were introduced. In my Ph.D, I continued these two research trends. I have performed two different studies: The first studies introduce a new device concept while the second studies bring lights into the physics behind the DW dynamics. I have performed experiments related to the both field-induced and current induced DW motion. Based on my experiments on the field induced DW dynamics, I propose a new phenomenon called chiral damping mechanism. Parallel to this work, I introduce a new device concept based on current induced DW motion and it is called magnetic origami. All this work will be described in the following chapters.

Chapter II

Experimental techniques

During my Ph.D, I have studied the DW motion in two multilayer systems: Pt/Co/Pt and Pt/Co/AlO_x. The field induced DW motion was studied in non-patterned thin films. The current induced DW motion was studied in nanostructures of different geometries: nanowires, structures with asymmetric shapes, etc. The samples were deposited by sputtering, and patterned using standard nanofabrication tools: e beam lithography, deposition, etching, etcThe domain wall displacements were measured using MOKE microscopy imaging technique. The details of all these techniques are described in this chapter.

II.1. Imaging of the DW motion using Magneto-optic Kerr effect (MOKE) microscopy

In my experiments, the DW motion was measured using the optical imaging technique called the wide field magneto-optic Kerr effect (MOKE) microscopy. Since the resolution of the microscope is ~300nm, this technique is suitable for studying DW displacements in nanowires down to 500nm wide as well as in thin films.

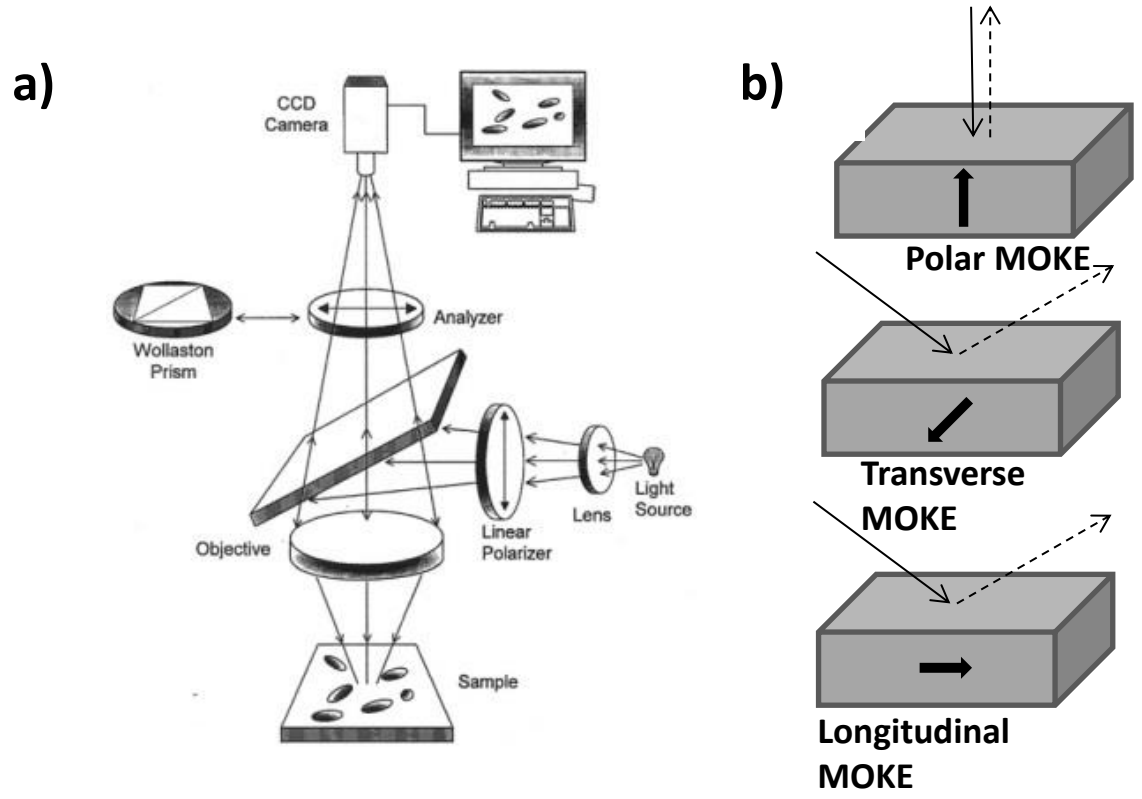

Figure II.1. a) Schematics of the optical diagram of the MOKE microscope. The light from the source gets linearly polarized and is then reflected by the semi-reflecting blade to enter the sample through the objective. The light reflected from the sample passes through the analyzer and reaches the camera. **b)** Ray diagrams Polar, transverse and longitudinal Kerr effects are defined according to the direction of the magnetization with respect to the incidence plane of the light and to the plane of the sample.

The Kerr effect arises due to the interaction between the light and a magnetic material. The reflection of a polarized optical wave from a magnetic material results in a change in both polarization state and intensity of the incident wave. Detecting these changes enables an indirect measurement of the magnetization of the material [Schäfer 2007]

Depending on the direction of the magnetization with respect to the incidence plane of the light and the reflecting sample surface, three different Kerr effects are defined: polar, linear and transversal Kerr effects (figure II.1.b). In my experiments, I used the polar Kerr effect (PMOKE) set up. In this set up, the normal incidence of the light was used where the magnetization is perpendicular to the reflection surface and parallel to the incidence plane. The change of the polarization after the reflection contains information about the out of plane magnetization state of the material. In the longitudinal MOKE case, magnetization is parallel to both the plane of the incidence and the reflection surface (figure II.1.b). Here the incident light is at an angle with respect to the reflection surface (not perpendicular as the polar MOKE). The linearly polarized incident light becomes elliptically polarized, with the change in the polarization is directly proportional to the magnetization component that is parallel to the plane of the incidence and the reflecting surface. In the case transverse case, the magnetization is perpendicular to the plane of the light incidence. Here unlike the linear MOKE case, instead of measuring the polarization, the intensity of the reflected light is measured.

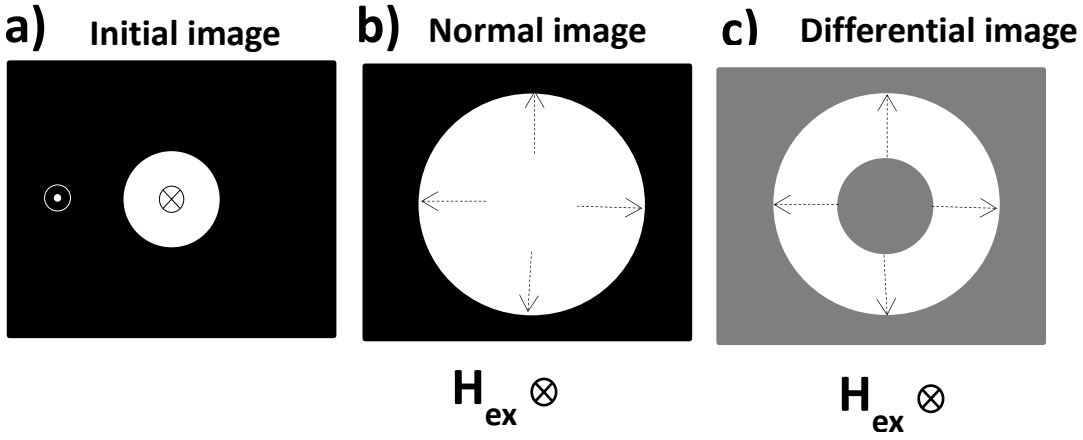

Figure II.2. Schematic diagrams of the MOKE images. Here the white and black color contrasts correspond to the down and the up magnetic domains respectively. **a)** The initial domain structure. The DW sits at the boundary of the two areas of different contrasts. **b)** Normal imaging of the domain structure after applying a field (H_{ext}) in the down direction. The image shows only the final boundary of the domain where the initial position of the DW can't be retrieved. **c)** The differential image, the subtraction of the image represented in a) from the one represented in b), shows the difference between the final (figure b) and the initial (figure a) domain structure. From this image, the initial and final positions of the DW can be easily detected and the DW displacements can be accurately measured.

A schematic diagram of the optical set up used in the PMOKE measurement is shown in figure II.1.a. A light beam passes through a polarizer and becomes linearly polarized. It is reflected by the surface of the magnetic material and passes then through an analyzer to finally reach the photodetector. At normal incidence, the incidence plane is parallel to the out-of-plane magnetization of the material. The interaction with the magnetization changes the linear polarization to an elliptical polarization associated with a rotation of the elliptical axis away from the initial direction of the polarized light. This angle of rotation and the ellipticity of the reflected wave are proportional to the magnetization. The rotation of the polarized light changes sign when the magnetization direction gets reversed. To image a sample, one can either scan a laser beam over the sample or use a wide field technique typically with a standard microscope. A camera connected to the microscope records the magneto-optical images. This is the typical set-up that I used during my PhD: a MOKE microscope. Since an up domain will rotate the polarization in one direction while a down domain will rotate it in the other direction, two different intensity of the light for each domain will result after the passage of the beam through the analyzer. Magnetic domains are then imaged by different contrasts (generally dark and bright contrasts).

The contrast of the output signal, that defines the intensity of the output signal varies from sample to sample depending on the magnetization, reflectivity etc. It also depends on the external parameters like the incident light intensity, the wavelength of the light, the alignment of the polarizer and analyzer etc. By tuning these external parameters, the contrast of the magnetic images can be improved. The observation of the sample surface from an overview at the centimeter scale down to a detailed imaging at the micrometer size is easily done changing the microscope objectives.

I used the differential imaging mode of the microscope to measure accurately the DW displacements. A schematic diagram describing the difference between normal and differential imaging modes is shown in figure II.2. Consider initially a small magnetic domain and an applied magnetic field resulting in the expansion of this domain. Using the normal imaging mode, the final image does not contain any information about the initial position of the DW (figure II.2.b). Therefore, it is difficult to measure the DW displacements precisely. The differential image shows the difference between the final and initial domains. Here, the DW displacement can be accurately measured (figure II.2.c).

Besides allowing imaging the magnetic state of a sample, the MOKE set-up can be used to measure the magnetic hysteresis loops. The variations with respect to the applied field of the intensity corresponding to the variations of the light polarization are plotted. This technique is a non-contact method and measurements can be much faster compared to other magnetic hysteresis loop measurement techniques such as Vibrating-Sample Magnetometer (VSM). One disadvantage of this method is that the magnetization is indirectly measured by

the variation of the optical wave properties. Therefore, extracting the quantitative information of the magnetization value using this method is difficult.

II.2. Sample fabrication

The sample fabrication includes the deposition of the multilayer using the sputtering technique, the patterning using optical or e-beam lithography, deposition, etching, etc. To fabricate the different sample structures, the different lithography procedures were followed. All the different steps are described in this section.

II.2.1. Deposition of the multilayers

Pt/Co/Pt and Pt/Co/AlO_x systems have been studied for many years at SPINTEC. Initially they were studied for optimizing the perpendicular magnetic tunnel junctions. They have been used then for DW motion studies as described in chapter I. They are deposited on Si/SiO_2 by sputtering.In the case of Pt/Co/AlOx layer, the upper layer is obtained by depositing the Al layer that is then oxidized using a low power RF oxygen plasma [Manchon 2008] [Monso 2002].

Extraordinary Hall effect measurements are used to measure the magnetic hysteresis loops of the samples. Two examples of hysteresis loops for a Pt $_{(3nm)}$ /Co $_{(0.6nm)}$ /AlO_x and a Pt $_{(2nm)}$ /$Co_{(0.6nm)}$ / $Pt_{(2nm)}$ are shown in figure II.3. The square shapes of the hysteresis loops indicate the good out-of-plane magnetic anisotropy with 100% remanence. The coercivity and the saturation magnetization values are different for the different samples.

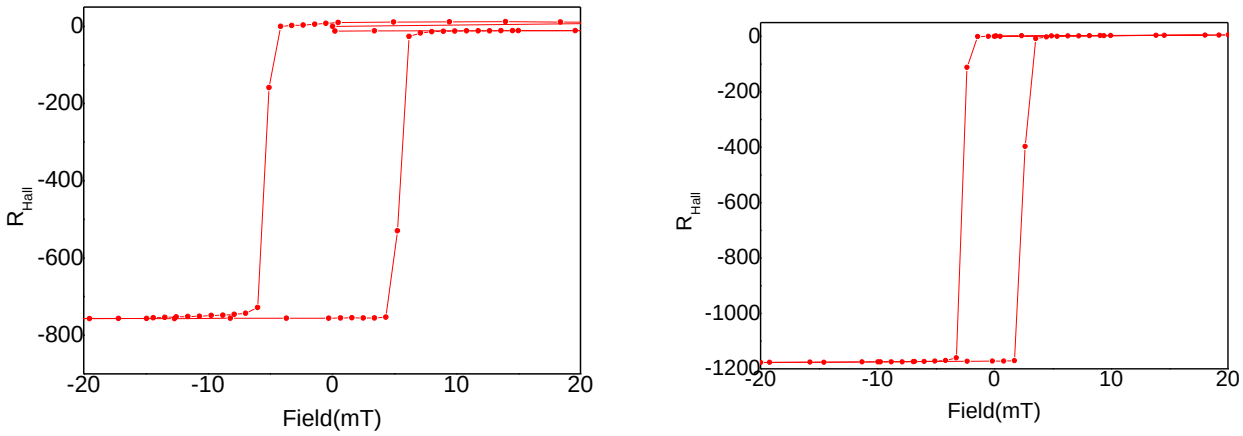

Figure II.3. Examples of hysteresis loops measured using ordinary Hall effect measurements for **a)** Pt $_{(3nm)}$ /Co $_{(0.6nm)}$ /AlO_x and **b)** Pt $_{(2nm)}$ /$Co_{(0.6nm)}$ / $Pt_{(2nm)}$ multilayers. The square loop indicates an out-of-plane magnetic anisotropic.

II.2.2. Fabrication of the nanowires

In chapter III, I will discuss the current induced DW motion in Pt/Co/Pt microwires. Current induced DW motion requires large current densities of the order of 10^{12} Am^{-2}. Therefore, experiments have to be done in confined geometries as micro- or nanowires. On the other hand, the smallest possible dimensions of the structures are limited by the resolution of the MOKE microscope. Since the optical resolution of the microscope is around 300nm, the widths of the structures have been chosen equal to or larger than this value. In my experiments on Pt/Co/Pt, I used 10µm long, 1µm wide wires.

A schematic diagram of the fabrication process of the microwires is shown in the figure II.4. The Pt/Co/Pt trilayer is first sputter deposited. Then a Ti mask in the shape of the microwires was fabricated on top of this thin film. The fabrication procedure includes the spin-coating of a positive photoresist and its exposure by ebeam lithography followed by its development. A thin Ti layer is deposited by evaporation followed by a lift off process. Ion beam etching is then used to transfer the shape of the Ti mask into the Pt/Co/Pt trilayer. The etching of the Ti mask, Pt and Co were monitored by in-situ secondary ion mass spectroscopy (SIMS). Whenever the required etching was completed, it was stopped manually. Finally, the contact pads were fabricated using optical lithography followed by the evaporation of an Au layer and a lift-off process.

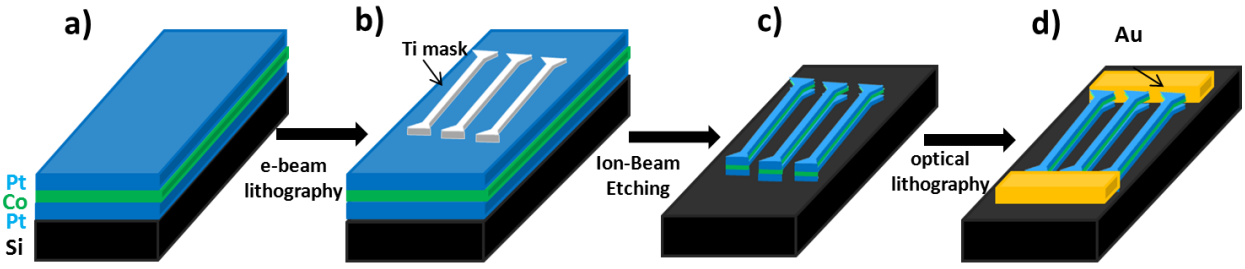

Figure II.4. Schematic diagrams of the different steps used to fabricate the wires **a)**The multilayer of the Pt/Co/Pt sample is sputter-deposited. **b)** After the e-beam lithography and development, a Ti mask in the shape of the nanowire is formed above the multilayer. **c)** After the ion beam etching, the nanowires of Pt/Co/Pt are formed. **d)** Optical lithography was then used to fabricate the gold contact pads.

It is not necessary that the Ti mask above the Pt/Co/Pt wires is etched completely as long as it is not too thick. In my experiments, around 5nm of Ti remained on the Pt/Co/Pt wires. A too thick Ti layer would potentially deviate a part of the current. However, since the electric conductivity of the Ti is much lower than that of the Pt, I did not observe such situation. However, in some cases, I have observed that a thick Ti layer may affect the

contrast of the magnetic imaging using MOKE microscope. In this case, the etching of the Ti was continued until a good magnetic contrast was obtained.

II.2.3. Fabrication process of nano-geometries

In chapter IV, I will describe the topic 'magnetic origami' where the DW motion and the switching behaviors were studied in different geometries from a Pt/Co/AlOx trilayer. There are two differences compared to the case described previously: the geometries used here are different from the typical nanowires generally used for current induced DW motion experiments; whereas in this last case the whole nanowire is constituted of Pt/Co/AlOx, in the magnetic origami case, the shapes of the Co and AlO_x are different from that the Pt (figure II.5.a). The fabrication process includes different levels of lithography, deposition and etching.

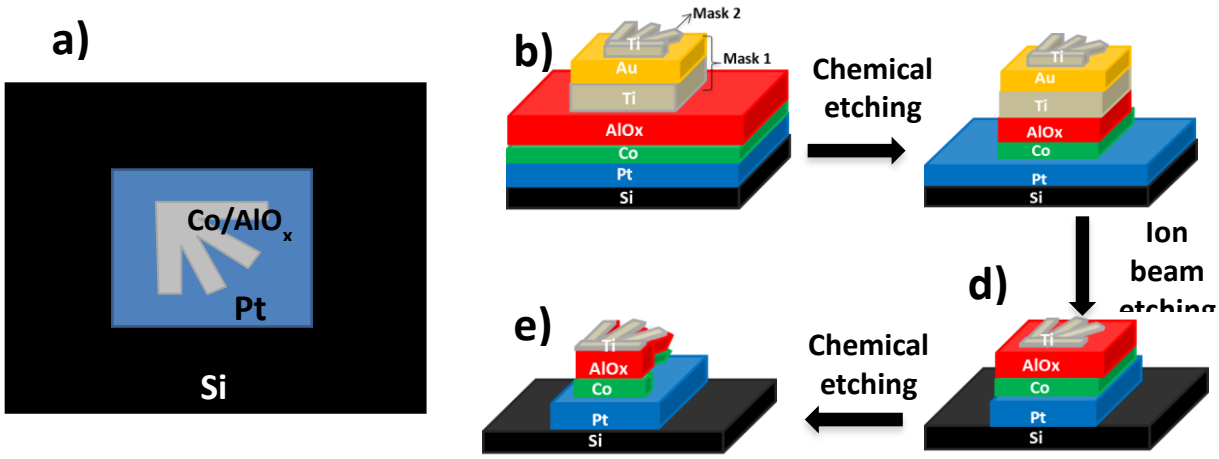

Figure II.5. a) Schematic diagram of the top view of the required sample geometry. It consists in Co/AlOx nanostructure sitting on top of a Pt rectangular pad. **b, c, d, e)** Schematic diagrams of the different structures after each etching step **b)** The structure after the fabrication of the masks on to of the Pt/Co/AlOx layer. Mask 1 has a rectangular shape and mask 2 has the shape of the required geometry. **c)** The structure after the first chemical etching of Co and AlOx. Here the layers under the masks were protected from etching. **d)** Ion beam etching removes the Pt and reduces the masks thickness. e) The final structure obtained after a last chemical etching step.

$Pt_{(3nm)}/Co_{(0.6nm)}/AlO_x$ trilayer was first sputter-deposited. Two levels of masks were then defined on top of this trilayer. Their fabrication involved ebeam lithography, evaporation and lift-off. The first mask was fabricated from Ti and Au in the form of a rectangle. On top of this, the second mask of Ti was patterned in the form of the required shape. Then three steps of etching were done. A schematic diagram of the different structures obtained after each etching step is shown in figure II.5. At first, using selective chemical etching, both AlOx and Co were removed while the rectangular part underneath the masks was protected (figure II.5.c). Secondly ion beam etching was used to remove the Pt as well as to reduce the

thickness of the masks until only a thin layer of Ti in the form of the required geometry is left on the top (figure II.5.d). Finally, a last selective chemical etching was used to remove all the Co and AlOx except the part below the thin Ti mask.

II.3. The Field Induced domain wall motion set up

I studied field induced DW motion using two combinations of magnetic fields: 1) under the application of an out-of-plane field and 2) under the combined action of an out-of-plane magnetic field and an in-plane field. The description of the corresponding experimental set-up is given in this section.

II.3.1. Out of plane field induced domain wall motion

Two electromagnetic coils were used in order to apply the out of plane magnetic field: for small field experiments, a macroscopic copper solenoid coil was used whereas a micro-coil was used for high field experiments.

Our normal macroscopic solenoid coil can generate small magnetic fields up to 30 mT. A Kepco (model BOP 100V/4A) was used to apply the voltage to the coil. The time duration as well as the value of the input voltage were controlled via a home-built lab view program. The field was applied continuously or with pulses (pulses down to 1 ms long can be applied). The unpatterned sample was fixed on a flat sample holder located above the electromagnetic coil. The complete system is then placed under the objective of the MOKE microscope in such a way that the sample stays above the center of the coil. The magnetic field is non-uniform since the field lines diverge from the center of the coil to its edges (figure II.6.a). Normally this does not affect our experiments since the sample area observed with the microscope is very small (few micrometers) compared to the size of the coil (few centimeters). The spatial variations of the field can be considered as negligible.

For the high field measurements, micro-coils designed by Marlio Bonfim [Bonfim 2001] were used. As shown in the figure II.6.b&c, the coils are made of copper electro-deposited on a Si/SiO_2 substrate. The copper layer was etched in the shape of a hole at the center surrounded by lines (shown by the white part in the figure II.6.b). In this geometry when a voltage is applied to the coil, the current lines are forced to follow a circular path around the central hole. This creates a perpendicular magnetic field. In my experiments, the current up to 60A can be injected, resulting in a magnetic field up to 400mT in the sample with pulse from 30ns to a few hundreds of ns long.

The procedure imaging of the DW motion is the following. The sample is cleaved into a 2x2 mm size piece that is pasted on the coil such that the upper surface of the sample is faced against the copper surface of the coil. In order to insulate electrically the sample from

the copper surface, a 100nm PMMA insulating layer was initially deposited on the copper surface of the coil [Bonfim 2001]. The system micro-coil/sample is then placed under the MOKE microscope and the imaging is done through the central hole from the back-side of the micro-coil (figure II.6.c). The field distribution inside the micro coil is not homogenous. The field amplitude increases from the center to the edges. For quantitative measurements of the DW displacements, such inhomogeneities were taken into account. The measurements were always done on the domain spanning the same spot on the magnetic thin films. Therefore, the errors due to the inhomogeneities were same for every measurement. Such errors were then subtracted to get the accurate value.

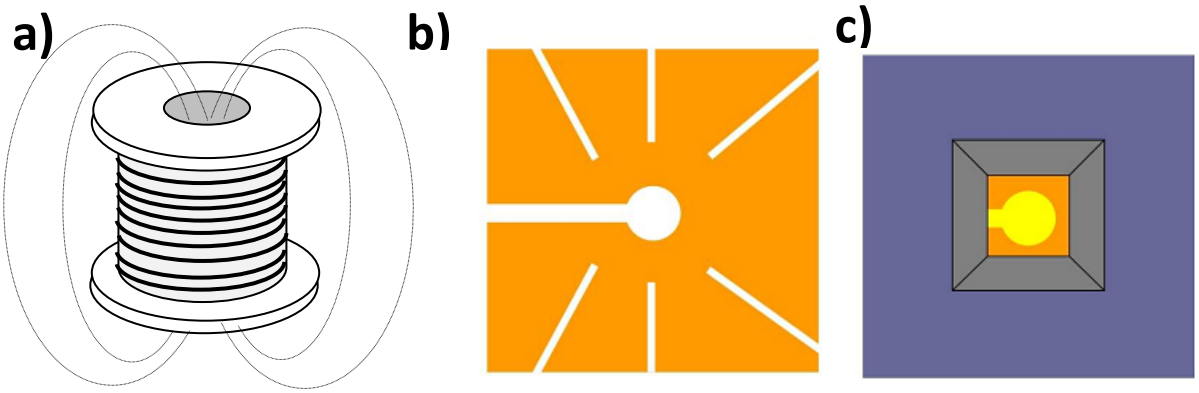

Figure II.6. Schematics of the out-of-plane magnetic coil used for the experiments. a) The normal macroscopic solenoid coil with copper windings. b) The front side of the micro-coil fabricated from copper. The white part shows the insulating part. During the imaging, the face of the sample is glued to this surface. c) The back side of the micro-coil. This side generally faces the objective of the microscope and the imaging is done through the hole at the center[Bonfim 2001]

To study the domain wall motion, an initial magnetic domain nucleation is required. The field required for the nucleation is relatively larger than that for the DW propagation. For better experimental conditions, a single domain nucleation is preferred because if several domains are nucleated, the DWs propagating from the different nucleated domains can overlap. This may limit the accuracy of the single DW displacement measurement. In an ideal sample, the anisotropy is uniform over the whole sample and so is the nucleation field. When this nucleation field is applied, many domains are nucleated. However I studied sputtered thin films that contain localized defects where the anisotropy is lower. At these sites, the nucleation fields are smaller and the application of a smaller field results in nucleations that can be controlled. In the case where several domains are nucleated because of the presence of several defects in the observed area, the sizes of these nucleated domains are generally different and the size of the smaller domains can be reduced by applying a reversed

propagation field, until a single magnetic domain is left on the sample., The DW propagation in this domain is then studied.

After the images acquisition, domain wall displacements are measured using the ImageJ software. The velocity is obtained by dividing the displacement by the magnetic field pulse duration.

II.3.2. DW motion in presence of an in-plane magnetic field

In chapter III, I will present my studies on the out-of-plane field driven domain wall motion in the presence of an in-plane field. In order to apply the in-plane field, the sample mounted on the out-of-plane field coil is placed between the poles of an in-plane electro-magnet. The out of plane field and the in-plane field can be applied together or separately. For both cases, a continuous DC field as well as field pulses (pulse duration $\geq$ 1 ms) can be applied.

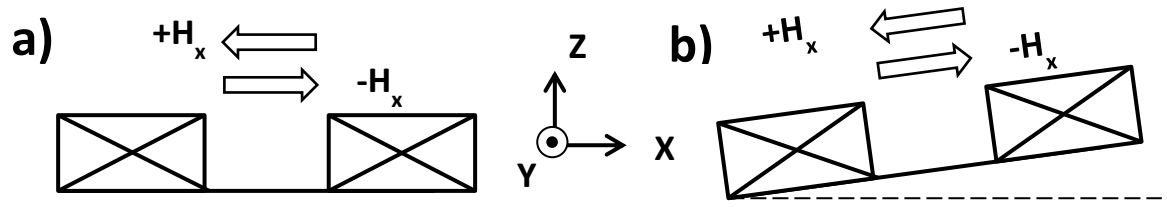

Figure II.7. Schematic diagrams of the arrangements of the in-plane field (H_x) coil on a supporting plate. **a)** without any tilt. Here the H_x does not give any out of plane field (along Z direction). **b)** If there is a tilt, then the opposite inn-plane fields ($\pm H_x$) give the opposite out of plane ($\pm H_z$) fields.

The in-plane field coil was placed on a supporting plate whose height and tilt can be adjusted. Any tilt of the in-plane field coil may contribute to the out-of-plane field felt by the sample and can influence the domain wall motion. Such sources of errors were removed by adjusting the tilt of the supporting plate as follows: The out of plane field driven DW displacements under the presence of a positive and then a negative in-plane field were studied. The opposite in-plane fields give opposite out of plane field components (figure II.7.B) which make the DW displacement different for both cases. The tilt of the supporting plate was adjusted until the DW displacements for both cases become equal.

The in-plane field was made of copper wire wound on an iron slab. Magnetic fields up to 350mT can be provided.

II.4. Current Induced DW motion set-up

Figure II.8 shows the schematic diagram of the experimental set-up used for the current induced DW motion measurements. The sample was fixed on the sample holder that presents two copper contact pads, an input and an output. The input is connected to an ultrafast voltage pulse generator and the output to an oscilloscope. These copper contact pads are connected to the sample using micro-bonding. When an input voltage is applied, the current first passes through the sample and then through the 50Ω impedance of the oscilloscope. The current is obtained from the voltage measured at the oscilloscope.

Four parameters can be tuned on the ultrafast voltage source according to the experimental requirements: the voltage amplitude, the pulse duration, the number of pulses and the frequency of the pulses.

The maximum current that can be injected through the nanostructures, depends on two factors: the maximum voltage that can be generated by of voltage sources and the resistance of the sample. For applying large currents, either voltage sources with larger maximum voltage can be used or the sample resistance can be reduced. According to the experimental requirements (they will be discussed in chapter III and chapter IV), I used different voltage sources with different maximum voltage. In order to reduce the sample resistance, gold contact pads were defined as explained in section II.2.2.

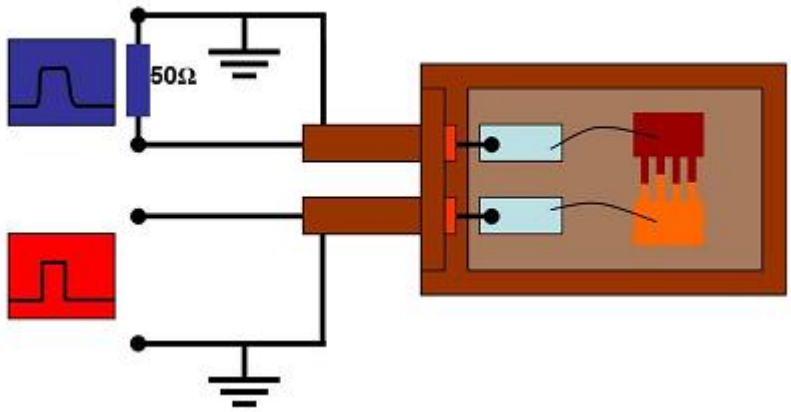

Figure II.8. Schematic diagram of the current induced DW motion measurement set-up. The sample is fixed on the sample holder. Using micro-bonding, it is electrically connected to the two copper electrodes (shown in light blue color). One of the copper electrodes is connected to the current source (red box) and the other one to the oscilloscope (blue box). The input impedance of the oscilloscope is 50Ω and the current amplitude is obtained from the voltage measured with the oscilloscope.

The current densities needed for DW motion are high, especially for fast DW motion. Applying the corresponding voltage during a relatively long time results in large over-heating that may destroy the nanostructures. ,Short pulses are required. In my different experiments I generally used pulses from 0.5ns to 10ns. If the domain wall displacement induced by a single short pulse was not large enough to be observed with the microscope, a series of several identical pulses was applied. To adjust the current induced heat dissipation in the sample I varied the interval between two consecutive pulses, the frequency of the pulses generation.

Knowing the shape of the pulse is important to determine the intrinsic domain wall velocity. The very short pulses that I used in my experiment, can present a large rising and fall times. Using the pulse duration to calculate the velocity is a source of errors, since the domain wall displacement does not occur during most of these rising and fall times. In order to remove this error in the velocity extraction, the following procedure was used to determine the intrinsic domain wall velocity. Domain wall displacements were measured for three different pulse durations. Then the graph of domain wall displacement v/s pulse duration is plotted whose slope gives the accurate domain wall velocity (an example is shown in figure II.9). Using this procedure, the error due to the rising and fall times are removed and the intrinsic velocity of the domain wall is accurately calculated since the rising and fall times are identical for the three pulses are same and only the differences between the three domain wall displacements are considered.

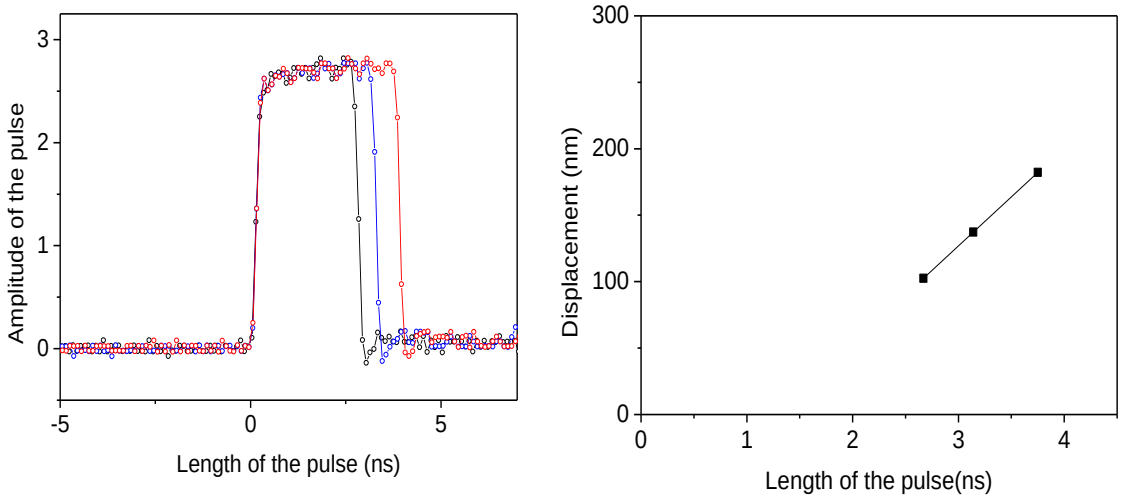

Figure II.9. Procedure of the DW velocity measurement. a) Example of three voltage pulses measured by the oscilloscope. **b)** DW displacement with respect to the pulse duration for three different pulse durations. The slope of the fit (displacement/pulse duration) gives the domain wall velocity. Note that the fit does not extrapolate to the origin. As explained in the text, the DW can be static during a part of the pulse, typically the rise and fall times.

II.5. Summary

I studied two different samples: non-patterned films and nanostructures. The layers were deposited by sputtering and patterned using standard methods: ebeam lithography, deposition and etching. Current and field induced domain wall motions were measured using PMOKE microscopy in the differential imaging mode. Out-of-plane as well as in-plane magnetic fields can be applied and fields up to 400mT for duration down to 30ns can be generated using micro-coils. Current pulses as small as 0.5ns were injected and the intrinsic DW velocity is obtained by measuring the DW displacements for several different pulses. All the studies using these set-ups and methods are described in the forthcoming chapters III and IV.

Chapter III

Domain wall motion in systems with weak SIA (Pt/Co/Pt)

In this chapter I will discuss about the chiral damping, a mechanism that can influence the DW dynamics in systems with structural inversion asymmetry (SIA). This is the result of my experimental studies of both current and field induced DW motion in Pt/Co/Pt trilayer systems.

In multilayer systems with SIA, the current induced DW motion is currently described using SOT+DMI mechanism. I have performed the qualitative study of the current induced DW motion in Pt/Co/Pt. From this measurement, we extracted the sign of the DMI. To understand the role of DMI in Pt/Co/Pt, the field induced DW motion was thoroughly studied in the same sample. Here, we observed incompatibilities with the expectations from the DMI model. To explain our results, we propose a new mechanism based on chiral damping. This is explained in the second section of the chapter. Finally the differences between the field induced DW motion in Pt/Co/Pt and that in Pt/Co/AlOx will be discussed.

III.1. Current induced domain wall motion in Pt/Co/Pt nanowires

Recently it was proposed that the combined action of DMI and the damping like torque (T_{DL}) could explain both the direction and the velocity of the DW motion [Thiaville 2012]. In multilayers with SIA, the DMI favors the chiral Néel DW wall structure. As a consequence, two consecutive DWs move in the same direction either towards or against the electron flow depending on the signs of the DMI and the T_{DL} (explained in details chapter I.7.3)

In the literature, a few studies reported the observation of current induced DW motion in symmetric Pt/Co/Pt multilayer systems [Moore 2008] [Lavrijsen 2012]. They showed that an observable pure current induced DW displacement is not achievable in Pt/Co/Pt. Since spin orbit torque is generally observed in systems with large structural inversion asymmetry (SIA), no DW motion is expected in ideal symmetric Pt/Co/Pt systems. However, recent studies show that depending on the growth conditions, from the microscopic point of view, a small structural asymmetry can persist in Pt/Co/Pt multilayers [Hrabec 2014] . Furthermore, by growing different thickness for Pt under and upper layer, a volume asymmetry can be introduced [Lavrijsen 2012] [Haazen 2013].

In this section, I will explain my experimental study of the current induced DW motion in $Pt_{(30Å)}/Co_{(6Å)}/Pt_{(15.6Å)}$ nanowires (10 µm x 1 µm size). A detailed discussion of the fabrication of the nanowires is given in chapter II. At first, the sign of the T_{DL} was obtained by measuring the current induced DW motion in presence of an in-plane field. Then the DW displacement under current injection was observed. Finally, by fitting the direction of the DW motion and the sign of T_{DL} into the DMI+SOT model, we obtained the sign of DMI. The details of these measurements are described in this section.

III.1.1. Method to measure the sign of the damping like torque

In section I.6.2.4.2, I have discussed how the damping like torque (T_{DL}) can induce the switching of a perpendicular magnetic device [Miron 2011a] [Liu 2012]. Here, a small in-plane magnetic field is used to define the direction of the magnetization reversal. The out of plane switching field (H_{sz}) that defines the magnetization reversal is proportional to ($\mathbf{z} \times \mathbf{j}$) × $\mathbf{H}_{ip}$. The ($\mathbf{z} \times \mathbf{j}$) defines the direction of the T_{DL} [Miron 2011a]. On the other hand, by measuring the H_{sz} field in the presence of a current (j) and an in-plane field, one can indicate the sign of the T_{DL}.

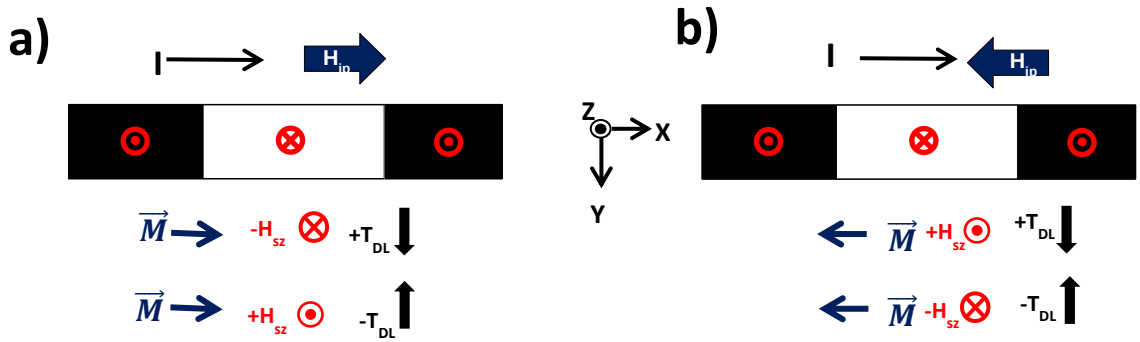

Fig III.1. Schematic diagram defining the direction H_{Sz} for the systems with **a)** For H_{ip} along +X direction **b)** For H_{ip} along –X direction, under current injection along +X direction. The in-plane magnetic field (H_{ip}) sets the magnetizations of both of the DWs in its direction. Depending on the direction of M and T_{DL}, H_{sz} can be either along ±Z directions. Depending on the direction of H_{sz}, the expansion of an up or down magnetic domain can be observed.

The spin-orbit effective fields can be quantitatively measured using ac-torque measurement set up [Garello 2013]. For my experimental studies explained in this section, the qualitative understanding of T_{DL} is enough; no quantitative analysis is required. This is why; I measured the current induced DW motion in the presence of H_{ip} to identify the sign of the T_{DL}. By imaging the type of DW motion (up to down or down to up), the sign of the H_{sz} field and thus the sign of T_{DL} can be retrieved.

Figure III.1 shows the schematics of the current induced displacements of the two DWs in the presence the H_{ip}. A sufficiently large H_{ip} saturates the magnetization of the DW along H_{ip}. If the H_{ip} along +X axis, the $+T_{DL}$ results H_{sz} along the –Z direction. Therefore the down magnetic domain expands (figure III.1.a). For the $-T_{DL}$, the up magnetic domain expands. The opposite will be observed when the H_{ip} is applied along –X axis (figure III.1.b).

III.1.2. Domain growth in presence of current and in-plane field in the nanowires

The sign of the T_{DL} in our sample was experimentally determined using the above procedure. At first, using current and H_z, I nucleated a magnetic domain and placed two DWs in the nanowire and observed their motion in the presence of current and H_{ip}. Figure III.2.a shows that applying current and H_{ip} in the same direction results in the expansion of down magnetic domains which indeed means that the H_{sz} is downwards (along negative Z direction). H_{sz} chages sign when the current and H_{ip} are applied opposite to each other. Comparing these results to the schematic diagram shown in figure III.1, we conclude that for the current applied in the positive direction, the sign of T_{DL} is positive (figure III.2.b).

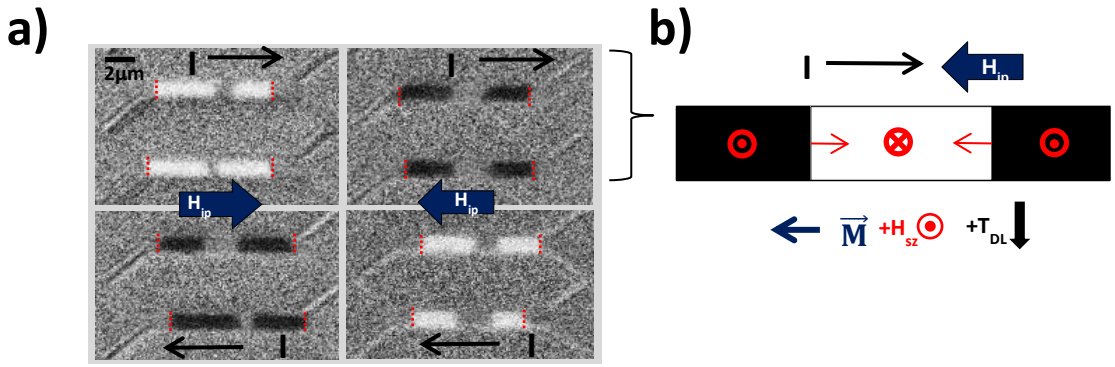

Fig III.2. **a)** The MOKE differential images of the DW motion in nanowires in presence of current and H_{ip}. Here the current density was 2.13 x 10^{12} A.m^{-2} and the H_{ip} was 70 mT. The red dotted lines show the initial positions of the DWs. When the current and H_{ip} are applied in the same direction, the magnetic switching field ($-H_{sz}$) expands the down magnetic domain (bright contrast). When the current and H_{ip} were applied opposite to each other the magnetic switching field ($+H_{sz}$) expands the up magnetic domain (dark contrast). **b)** Schematic diagram of the directions of the core magnetization, the effective switching field and T_{DL} for the current and H_{ip} applied along positive and negative X axis respectively.

III.1.3. Current induced DW motion in the nanowires

We performed DW motion experiments in the nanowires by applying only the current. As shown in figure III.3.a, we observed the DW motion in the direction of the current. Here the DW motion in the sample was very slow (~order of 0.1 m/s), but the direction of the motion was always preserved.

For the further confirmation the direction of the DW motion, I placed two DWs (up/down and down/up) in the nanowire and studied the current induced DW motion in presence of an out of plane (H_z) field as shown in figure III.3.b. Here the H_z field moves the both DWs equally in the opposite direction while the current applies unidirectional pressure. This results in an asymmetric DW motion and the direction of the asymmetry indicates the contribution from the current. The asymmetry of the DW motion is always in the direction of the current (figure III.3.b). This again confirms the contribution of the current to the domain wall motion is in the direction against the electron flow

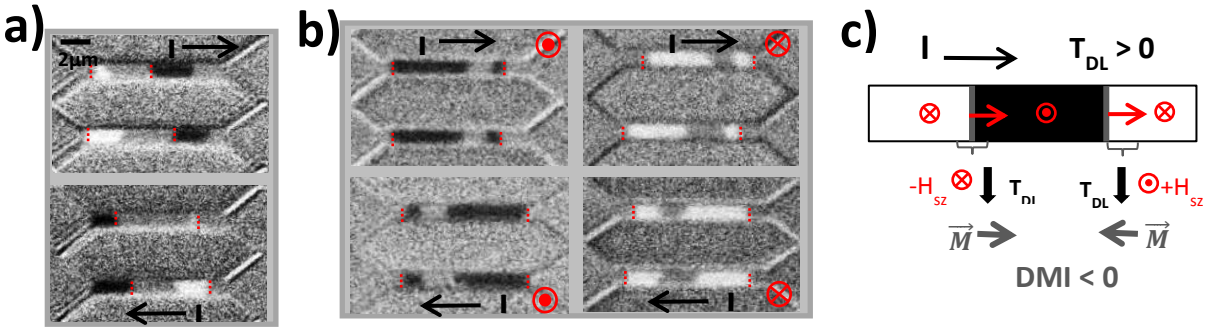

III.3. a) The MOKE differential images of CIDW motion in the nanowires of Pt/Co/Pt by applying current alone. Here the current density was 2.55 x 10^{12} A.m^{-2}. The red dotted lines show the initial positions of the DWs. The DWs clearly moves in the same direction of the current. **b)** The current induced DW motion (2.13 x 10^{12} A.m^{-2}) of two DWs (up/down and down/up) in the presence of a small H_z field (±15mT). Here the DWs moving in the same direction as the current have higher velocity compare the DWs moving opposite to it. This confirms that the contribution from the CIDW motion to the net DW motion is in the same direction of the current. c) Schematics of the CIDW motion according DMI+T_{DL} model. For the T_{DL} along +y direction and DW motion in the direction of the current, the sign of the DW should have left handed chirality (DMI<0)

The comparison of the DW displacement with DMI+T_{DL} mechanism is shown in figure III.3.c. By analyzing the sign of the T_{DL}, the sign of direction of the current induced DW motion, we deduced that the DW has left chiral Néel structure (DMI<0) where the DW magnetization rotates anti-clockwise.

III.1.4. Conclusions

We observed that the current induce DW motion in Pt/Co/Pt in the direction against the electron flow. Comparing this result to the DMII+T_{DL} model, we concluded that our sample has left handed chiral Néel DW structure.

Recently, it was reported that the field induced DW motion studies can be used to measure the sign of the DMI. By using this method, we compared the sign of the DMI

measured by the current. We found incompatibilities between these measurements. This is described in details in the next section.

III.2. Field induced DW motion in Pt/Co/Pt thin films

In this section I will explain about the out of plane field driven DW motion in presence of an in-plane field in Pt/Co/Pt thin films. At first, I will explain how we can use the field induced DW motion to measure the sign of the DMI. Here I will review the various studies reported in the literature and then compare these studies with my experimental results. Then I will show a detailed quantitative studies of the field induced DW motion. As a result of this study, I will introduce a new mechanism producing an asymmetric DW dynamics, the chiral damping.

III.2.1. Method to measure DMI sign

In 2012, A. Thiaville *et al* proposed the DMI+T_{DL} model to describe the current induced DW motion mechanism [Thiaville 2012]. Shortly after this prediction, CIDW motion in the presence of a longitudinal hard axis magnetic field (H_L) evidenced chiral phenomena that were claimed as a proof of the existence of the DMI and as a validation of the (DMI+T_{DL}) scenario in these metallic layers[Ryu 2013] [Emori 2013] (explained in chapter I.7.4). These experiments open the quest for direct evidence of the (DMI + T_{DL}) scenario as well as the measurement of the DMI amplitude. Direct microscopy imaging is the most straightforward way to determine the DW structure. However, these observations were limited to particular samples well suited for the observation [Tetienne 2014] [Chen 2013]. Interestingly, it was proposed that the out of plane field induced DW motion in presence of an in-plane field can be used as a method to measure the sign of the DMI. The details of this experiment is explained in the next section

III.2.1.1. Field induced asymmetric bubble domain expansion

Recently it was proposed that by measuring the expansion of a magnetic bubble in the presence of an in-plane and out of plane field, the sign and the strength of the DMI can be identified. In the pioneer studies, S-G. Je *et al* [Je 2013] showed that analyzing the asymmetric bubble domain growth in different Pt/Co/Pt trilayer systems, the DMI field of the systems can be quantified. They studied field induced domain wall motion in asymmetric Pt/Co/Pt multilayers using wide field Kerr microscopy. They observed that, when the out of plane and in plane fields were applied simultaneously, a magnetic bubble domain expands asymmetrically. In the case of magnetic multilayers with perpendicular anisotropy like Pt/Co/Pt, perpendicular magnetic fields (H_z) propagate the DWs isotropically in the plane of the film. Normally, if in-plane field (H_{ip}) is applied along with the H_z, the symmetry of the DW displacement should not be affected. But they observed that in presence of H_{ip} the H_z

driven DW motion becomes asymmetric (shown in figure III.4.a). i.e. the two DWs (up/down and down/up) moving in opposite directions along the axis of H_{ip} have different velocity. S-G. Je et al [Je 2013] claimed that this asymmetric DW motion behavior is due to the presence of the DMI interaction. According to the DMI model, an internal field H_{DMI} sets the internal magnetizations of up/down and down/up DWs in opposite directions. Thus two DWs moving opposite to each other along H_{ip} axis experience different effective fields (H_{ip}-H_{DMI} and H_{ip}+H_{DMI}), hence they move with different velocities.

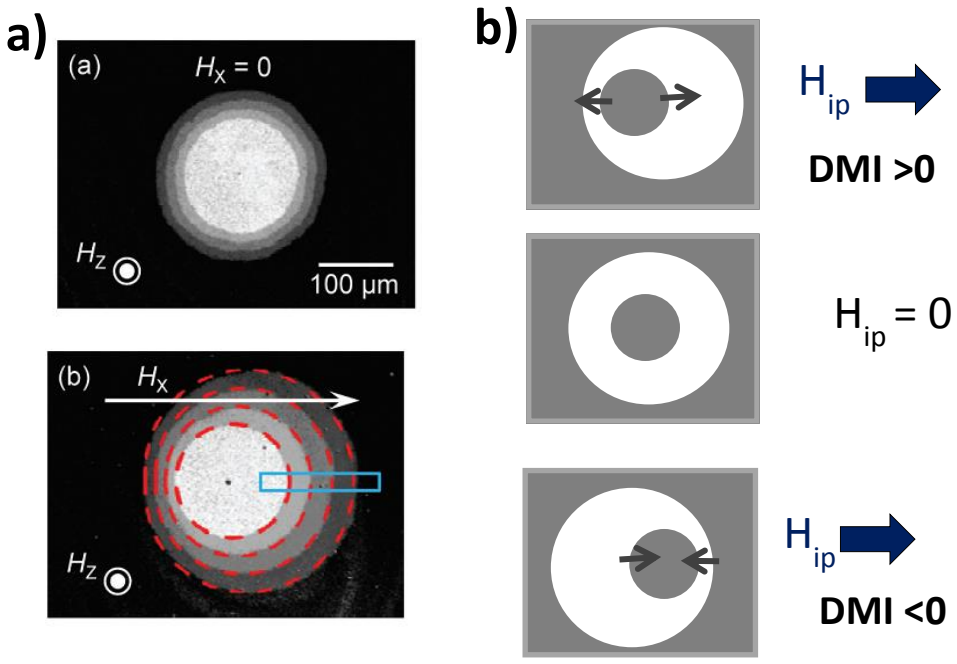

Fig III.4.a) The observation of asymmetric DW motion by S-G.Je *et al* [Je 2013]. Here the white contrast corresponds to the up magnetization. When H_x=0, H_z causes the symmetric bubble domain expansion. When an H_x field introduced along with H_z, the bubble domain expands asymmetrically. **b)** The schematic diagram to explain the asymmetric DW motion based on the idea of DMI. The grey arrows show the magnetization at the center of the DW. If DMI>0, the domain wall has right Néel structure where the core magnetization inside of the up/down domain wall points to the right; down/up DW has opposite magnetization. When the H_{ip} is applied, the DW with the magnetization in the same direction moves faster resulting the domain expansion asymmetric. Opposite asymmetry will be observed for the case DMI<0.

Depending on the direction of the asymmetry (or the direction of the fast DW motion), the chirality of the Néel DW and thus the sign of the DMI can be identified. If the Néel wall is of right handed chirality (the magnetization inside the DW rotates in clock wise direction), under the positive in-plane field, the up magnetic bubble domain expands asymmetrically towards the positive direction. Opposite asymmetry will be observed for the down magnetic domain as well as for the negative in-plane field (figure III.4.b).

Later, using the same technique, A. Hrabec *et al*[Hrabec 2014] showed that the sign and the strength of the DMI depend on the growth and the choice of the heavy metal in the multilayer systems. They observed that the sign of the DMI in Pt/Co/Pt can be controlled by inserting an Ir layer in between Pt and Co. By varying the thickness of the Ir layer, the asymmetry of the bubble expansion reverses its direction (figure III.5.a). This is because the sign of the DMI reverses by inserting the Ir layer. Further, they showed that the DMI can be present or absent in almost symmetric Pt/Co/Pt system depending on the growth condition. To prove this, they have studied the asymmetric domain expansion in two Pt/Co/Pt systems with same thickness but different growth conditions. One sample was deposited by sputtering and another one was deposited epitaxially using MBE technique. In the case of the sputtered samples, the asymmetric bubble domain expansion was observed. On the other hand in the epitaxial samples, the DW motion was symmetric. They concluded that the structural inversion asymmetry in the sputtered Pt/Co/Pt is due to the micro-structural differences between the lower Pt/Co and upper Co/Pt interfaces. On the other hand, the epitaxial samples have high level of crystallographic ordering and the multilayers are nearly symmetric.

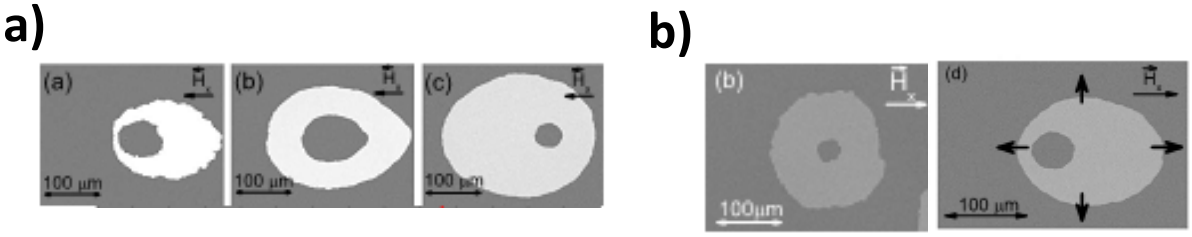

Fig III.5. a) The MOKE images of asymmetric bubble expansion studied by A. Hrabec *et al* [Hrabec 2014] measured for three different Pt/Co/Ir(t)/Pt samples (t= 0, 2.3Å and 4.6Åfrom left to right). The asymmetry of the bubble expansion reverses its direction as the t is increased. This is due to the reversal of the sign of the DMI. **b)** The comparison of the bubble expansion for the epitaxial and sputtered samples. For the epitaxial samples, no asymmetry in the DW motion was observed. This indicates that there is no SIA exist in the epitaxial sample.

To summarize, both studies by S.G-Je *et al* and A. Hrabec *et al* showed that asymmetric bubble expansion experiment can be used as a standard tool to measure the sign of the DMI. They also confirmed that by controlling the growth conditions, the SIA can be achieved in Pt/Co/Pt.

III.2.1.2. Asymmetric bubble expansion in Pt $_{(30Å)}$/Co$_{(6Å)}$/Pt$_{(15.6Å)}$

In order to determine the sign of the DMI and thus the structure of the DW in our Pt/Co/Pt sample, we studied the H_z induced growth of a bubble domain in presence of H_{ip}. The films were sputter grown at room temperature on etched Si/SiO_2 substrates. The differential MOKE microscopy images of the bubble expansion are shown in figure III.6.

When H_{ip} is applied along +X, the up/down DW move faster along +X compared to the down/up DW moving along -X. Opposite asymmetry is observed for the opposite H_{ip}. This indicates that the magnetization inside the DW rotates clockwise (with right handed chirality) and hence DMI is positive. This result is the same as the one measured by S-G Je *et al* [Je 2013] and A.Hrabec *et al* [Hrabec 2014].

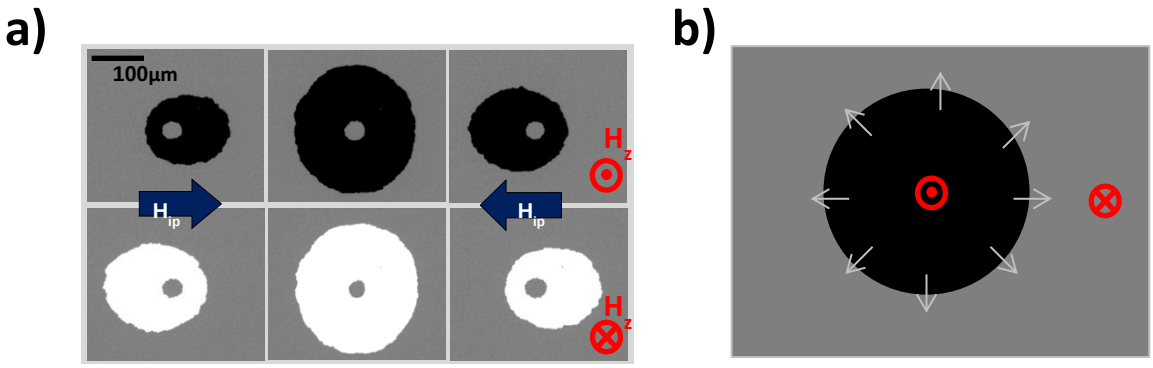

Fig III.6. **a)** The MOKE microscopy differential images of DW motion in $Pt_{(30Å)}/Co_{(6Å)}/Pt_{(15.6Å)}$ trilayer. The black and white contrasts correspond to the up and down domains respectively. The blue arrows show the direction of H_{ip}. The H_z used here was 11mT. When H_{ip}=0, the DW motion is symmetric towards all the directions in the plane of the film. When H_{ip} (±40mT) is applied, the DW motion becomes asymmetric. For the up/down DW motion the asymmetry is in the direction of the H_{ip} and for the down/up DW motion it is opposite. If this asymmetric DW motion is due to DMI, then the sign of the DMI should be positive, resulting in right handed Néel wall. **b)** The schematic of the core magnetization of right handed Néel wall structure (shown by the arrows).

III.2.1.3. The contradiction of the sign of the DMI

In section III.1, I have explained the measurement of the current induced DW motion in $Pt_{(30Å)}/Co_{(6Å)}/Pt_{(15.6Å)}$. This measurement predicted the presence of left handed chiral Néel wall structure (DMI<0). Contrary to this, in the same multilayer system, the field induced asymmetric domain expansion shows the Néel DW structure with right handed chirality (DMI>0). This dilemma questions the validity of determining the sign of the DMI using field and current induced DW motion.

III.2.1.4. Conclusion

We studied the asymmetric bubble domain expansion in $Pt_{(30Å)}/Co_{(6Å)}/Pt_{(15.6Å)}$ of H_{ip} and H_z . We found a discrepancy between the sign of the DMI measured by field and current induced DW motion. Even though we do not have a unique explanation for this observation, we would like to suggest a few possibilities.

1) The field induced bubble expansion method to measure the DMI sign is wrong. If the DMI has the opposite sign of that predicted from the asymmetric bubble expansion picture, the DMI + T_{DL} model explains the current induced DW motion direction. If so, the asymmetric bubble expansion may arise from another mechanism that is different from the DMI.

2) The field induced DW motion experiment defining the sign of the DMI is correct, while the DMI+T_{DL} model to describe the current induced DW motion is not applicable for our sample. If this hypothesis is confirmed, the original question that initially motivated the DMI+T_{DL} model, (why the DW moves in the direction of the current? [Miron 2011b] [Thiaville 2012]) would remain unanswered. We would have to consider different hypothesis such as negative STT [Šipr 2008] [Lee 2010] in order to explain this observation.

3) There is no DMI in Pt/Co/Pt. If so, in the absence of DMI, both field induced DW motion and the current induced DW motion in Pt/Co/Pt requires an alternate explanation.

All these three possibilities indicate that more theoretical and experimental efforts are needed to understand the DW motion in Pt/Co/Pt.

In order to shed some light on these discrepancies, we decided to focus our efforts on the field induced asymmetric bubble expansion experiment. Since it avoids the extra complexity of the current induced torques, it should be easier to understand.

III.2.2.Chiral damping mechanism of the magnetic DWs

Magnetic materials with structural inversion asymmetry (SIA) can exhibit different spin orbit related phenomena. One such phenomenon is Dzyaloshinskii-Moriya interaction (DMI) leading to the existence of chiral Néel domain walls (DW). Until now, DMI was the only well-established interaction that may explain chiral DW dynamics. Here, using our experimental evidence of field induced domain wall motion in Pt/Co/Pt trilayer; we prove that DMI is not the only interaction caused by the SIA that can influence the DW dynamics. We propose a new SIA related phenomenon: a chiral damping mechanism.

In this section, first I will show the detailed experimental studies of the asymmetric bubble domain expansion in different Pt/Co/Pt multilayers. Then I will show the comparison of the experimental results with micro magnetic and numerical models. At the end, the idea of the chiral damping will be discussed in details.

III.2.2.1. Background

A qualitative picture of the asymmetric bubble domain expansion under the application of H_z and H_{ip} is explained in the last section. In their pioneer studies, S-G *Je et al* reported that quantitative variation of the DW velocities with respect to the H_{ip} can be used as a

method to measure the DMI field. As explained earlier, according to the DMI model, the two DWs moving opposite to each other along H_{ip} experience different effective fields (H_{ip}-H_{DMI} and H_{ip}+H_{DMI}). This leads to the differences in their velocities and creates the asymmetric domain expansion. They proposed that by studying the variation of the DW velocities by varying the H_{ip} for a constant H_z, the intrinsic H_{DMI} of the sample can be measured.

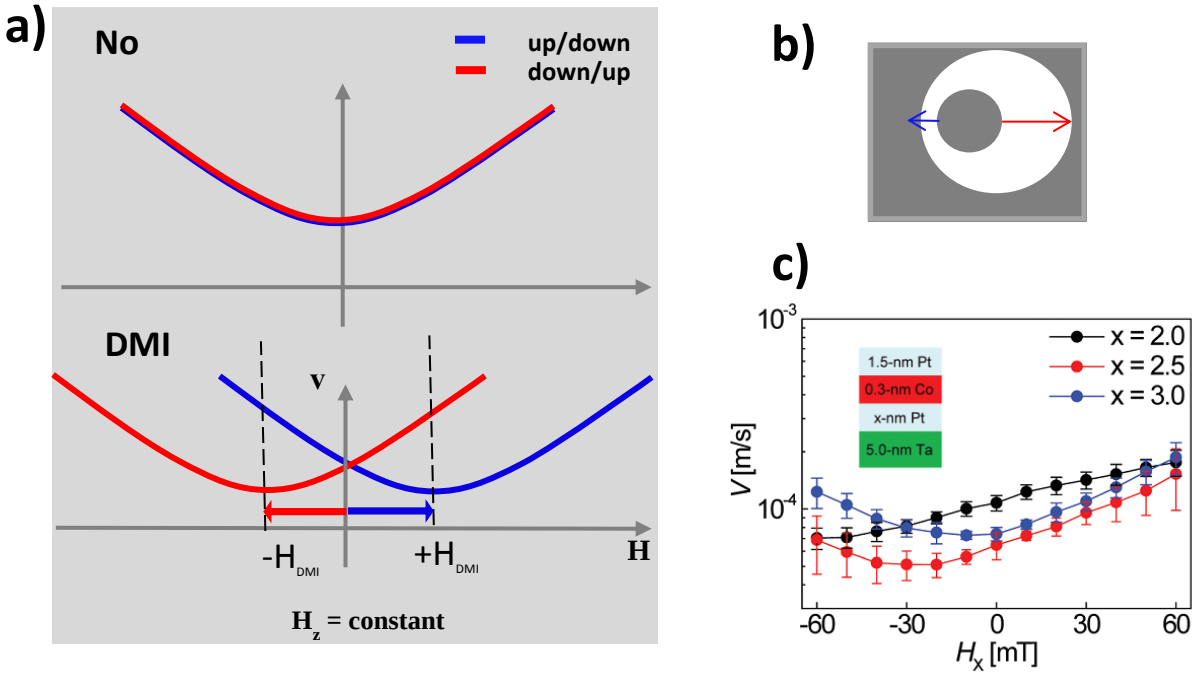

Fig III.7. a) Schematic diagram of the domain wall velocity vs. H_{ip} at constant H_z. In the absence of the DMI, the DW velocity increases symmetrically with respect to H_{ip}=0 for both up/down and down/up DWs (red and blue curves). In the presence of the DMI, the two DW velocities shift horizontally opposite to each other by a bias field $\pm H_{DMI}$. **b)** Schematic diagram of a differential image of the asymmetric DW motion. Red and blue arrows correspond to the displacements of the up/down and down/up DWs. **c)** The measurement of the velocity vs. H_x by S-G Je *et al*[8] for different Pt/Co/Pt samples. They show that the values of H_{DMI}, measured by the bias shift, are different for different samples. The value of H_{DMI} is determined by the position of the velocity minimum.

A schematic illustration of the measurements of the H_{DMI} using the velocity curve with respect to H_{ip} field is shown in figure III.7.a. In the absence of SIA, H_{ip} can modify the H_z driven DW velocity through different mechanisms. For example, it can modify the anisotropy or the energy landscape for the DW motion. Assume that applying the H_{ip} increases the DW velocity. In this case up/down and down/up DWs move with equal velocities (shown in figure III.7.a). The DW velocity curves will have parabola shape with the minimum of the velocity at H_{ip}=0. When the SIA is turned on, the DMI provides an intrinsic in-plane bias field (H_{DMI}) to the DWs that will shift the minimum velocity will away from H_{ip}=0. The new minimum

will occur when $H_{ip} = -H_{DMI.}$ Since the directions of the H_{DMI} for the two DWs (up/down and down/up) are opposite to each other, the two velocity ($V_{\uparrow\downarrow}$ and $V_{\downarrow\uparrow}$) curves shift opposite to each other

In their experiments, S-G Je *et al* measured the H_{DMI} fields for different Pt/Co/Pt sample (shown in figure III.7.c). i.e, they proposed a way for the quantitative comparison of the H_{DMI} values for different samples.

In my experiments, I followed the same procedure of the S-G Je *et al* to measure the H_{DMI}. In our detailed study, we observed new features for the DW velocities that deviate from the simple DMI model. All these experiments are explained in the following section.

III.2.2.2 Experimental study of field induced DW motion in Pt/Co/Pt

III.2.2.2.1. The DW velocity vs H_{ip} (at constant H_z)

I have studied the field induced domain wall motion in different $Pt_{(30Å)}/Co_{(6Å)}//Pt_{(tÅ)}$ samples. The details about the experimental set up are described in chapter II. The DW motion was studied using the MOKE microscopy. The experimental procedure is the following: At first a bubble domain is nucleated by either applying H_z or applying H_z and H_{ip}. Then the differential images of the asymmetric bubble expansion under the action of H_z and H_{ip} field were taken. Here synchronized H_z and H_{ip} field pulses were applied for the duration of 400ms. Then the DW displacements were analyzed and the DW velocities were calculated.

The MOKE differential image of the asymmetric bubble expansion for the $Pt_{(30Å)}/Co_{(6Å)}/Pt_{(15.6Å)}$ sample was already shown in figure III.6. The corresponding DW velocity vs. H_{ip} curves for the two DWs (up/down and down/up DWs moving opposite to each other along the H_{ip} axis) are shown in figure III.8.b and figure III.8.d. We found a deviation from the expected parabolic behavior for the case of the DMI. Nevertheless, according to the DMI model H_{DMI} should act as a bias field that shifts the curves laterally (figure III.7.a). By shifting the two curves in opposite directions by the H_{DMI}, they should coincide. In our case, it is impossible to overlap the curves by any amount of lateral shifting (Figure III.8.b and figure III.8.e). i.e, the DW velocity vs. H_{ip} does not show a horizontal bias shift.

III.2.2.2.2 Symmetric and antisymmetric component of DW velocity

The failure to explain our data using the existing DMI model calls for a detailed analysis in terms of symmetry. The H_{ip} makes the DW motion asymmetric, but at the same time it can also bring symmetric contributions (that are the same for both DWs). This symmetric contribution may not necessarily originate from the SIA related mechanism (for example the H_{ip} changes the overall anisotropy of the systems). At the same time, the asymmetric

contribution can only originate from the SIA associated effects. The velocity variation of the DWs in the presence of H_{ip} is a mixture of these both symmetric and asymmetric contributions. In order to deduce the contribution of the SIA related effects, it is important to start from the study of the anti-symmetric component of the velocity.

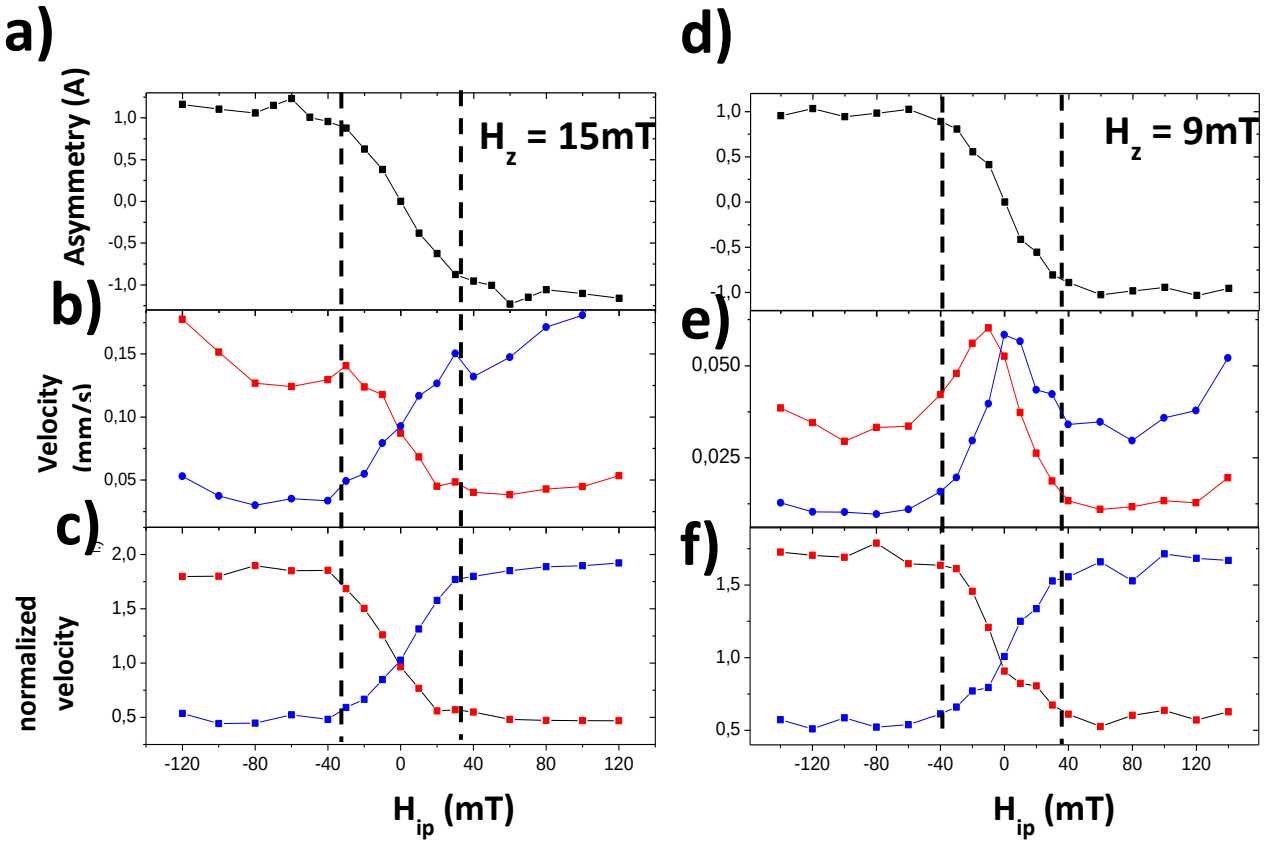

Fig III.8. The experimental graph for **a,d)** the asymmetry v/s H_{ip} **b,e)** the velocity *vs* H_{ip} **c,f)** the normalized velocity v/s H_{ip} for the two samples Pt $_{(30Å)}$ /Co $_{(6Å)/}$ Pt $_{(15.6Å)}$ and Pt $_{(30Å)}$ /Co $_{(6Å)/}$ Pt $_{(18.6Å)}$ respectively. The asymmetry and the normalized velocities for both DWs saturate at H_{ip} = ±40mT associated with a slope change of the velocity graphs at the same field.

III.2.2.2.3. Anti-symmetric component of the DW velocity vs. H_{ip}

In the presence of the H_{ip}, the bubble DW motion becomes asymmetric. The quantitative indicator of the asymmetry is the anti-symmetric component of the velocity. This parameter is shown in figure III.8.a and III.8.d. The A can be written as

$$A = \frac{V_{\uparrow\downarrow} - V_{\downarrow\uparrow}}{[(V_{\uparrow\downarrow} + V_{\downarrow\uparrow})/2}$$

A shows the same behavior for all samples. It increases with increasing H_{ip} and then saturates around H_{sat} = ±40mT. This indicates that the physical parameters that responsible for the asymmetry also saturates above the H_{sat}. The only physical parameter that can vary monotonically and saturates at 40mT is the DW core magnetization. The other possible parameter, the tilt of the magnetization in the domains saturates at much larger fields (> H_K~ 400mT).

Furthermore, if we analyze the data from this perspective we observe that at 40mT both DW velocity curves show a change of slope. Within the DMI scenario, due to the H_{DMI} bias field, only one of the DWs should exhibit a feature at 40mT, the other one should saturate before, and therefore there should be no particular feature on the DW velocity at this field. This observation indicates that the magnetization of both DWs saturates at almost the same in-plane field, indicating that H_{DMI} is much smaller than 40mT.

So far we observe that our data does not behave as predicted by the DMI model, and that the HDMI in our samples is very small. Another puzzling observation is that the measurements performed for different samples and different values of H_z exhibit a very similar variation of their anti-symmetric component even though the raw data looks very different. This indicates that besides the SIA phenomenon reflected in the variation of A, there is also a supplementary symmetric contribution that may not be related to the SIA. In order to remove this symmetric contribution from the raw data, we normalize the DW velocities by the average displacement in all directions. As a result, all the measurements performed on different samples at different Hz exhibit an identical behavior: the DW velocity decreases (or increases – depending on the direction of H_{ip}) monotonically, and saturates at 40 mT (figure III.8. c & f)

III.2.2.2.4. Thickness dependence of DW motion asymmetry and interface anisotropy

To understand the dependence of the asymmetric DW motion on the material properties, we have studied different $Pt_{30Å}/Co_{6Å}/Pt_{(tÅ)}$samples with different thickness of the Pt upper layer (t= 15Å-70Å). The **A** vs H_{ip} graphs are shown in figure III.9.a. All the samples showed the same trend: the asymmetry varies up to H_{sat} and fully saturates above. The saturation values of **A** decrease as the Pt thickness is increased (figure III.9.a inset). Even though the asymmetry values vary from sample to sample the H_{sat} remains the same. The lack of correlation between the value of A and H_{sat} is also inconsistent with the DMI scenario.

In order to check if the uniaxial anisotropies (H_k) contribute to the asymmetry variations, the H_K for different samples were determined using anomalous Hall Effect measurements as shown in figure III.9.c. The anisotropy field shows a reduction from the sample with the thinnest (15.6Å) Pt upper layer to the thickest (70Å). It shows a variation of

30% (0.55 T to 0.38 T). After correcting for the layer's demagnetizing field ($\mu_0 M_s$=1.3 T), we calculate a maximum variation of the anisotropy constant of 10%.

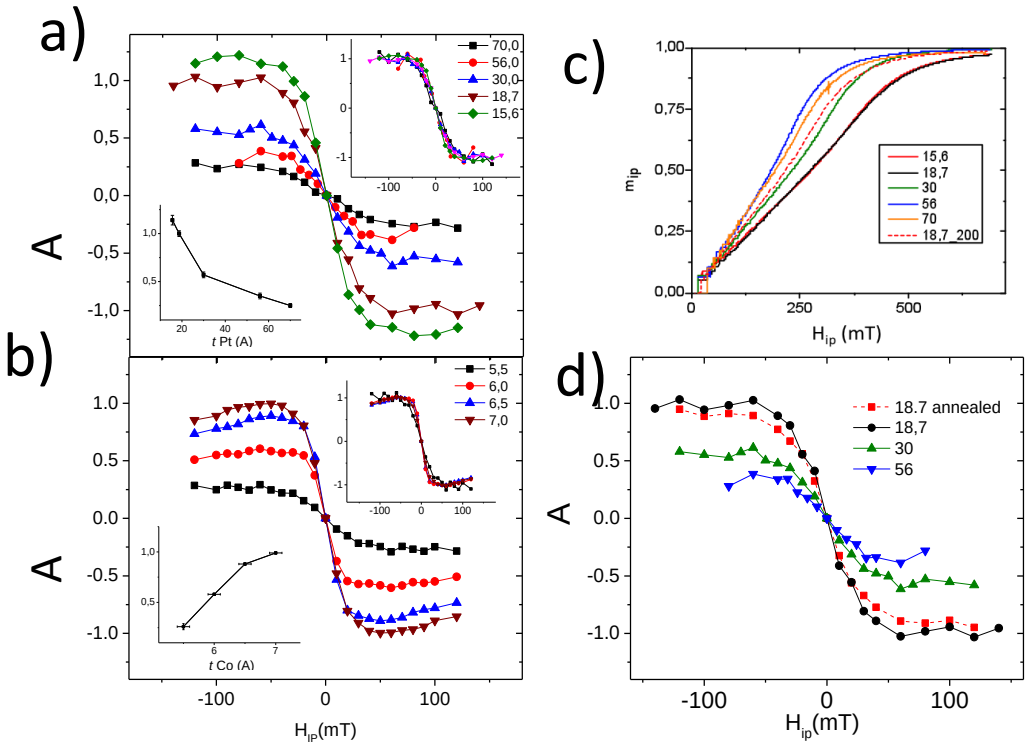

Figure III.9. **a.** Asymmetry curves extracted from Kerr microscopy images for the samples with different Pt thickness ranging from 15 Å to 70 Å. The inset shows the variation of **A** with respect to the Pt thickness **b.** A measured for the sample with different Co thickness varying from 5.5 Å to 7 Å. The variation of the saturation asymmetry values with respect to the Co thickness is shown in inset. **c.** The anisotropy fields of all the samples used in the experiment measured using the anomalous Hall effect. **d.** Asymmetry of the annealed sample compared to the as deposited ones. If the asymmetry value would be correlated to the anisotropy field the asymmetry of the annealed sample (red) would be comprised in-between the asymmetries measured for the samples with 30Å and 56Å of Pt capping.

In a second experiment, we have studied samples with different thickness of the Co layer $Pt_{30Å}Co_{t Å}Pt_{18Å}$ (t = 5.5Å–7Å). The measured anisotropy fields are: $H_k(Co_{5.5Å})$ = 6.0 kOe, $H_k(Co_{6Å})$ = 6.5 kOe, $H_k(Co_{6.5Å})$ = 6.0 kOe and $H_k(Co_{7Å})$ = 6.4 kOe. The measured asymmetry variation was similar to the samples with different Pt thickness. Here the asymmetry values increases with increasing the Co thickness (figure III.9.b). Once again we found that the H_{sat} and the saturation value of **A** are not correlated.

To check if the heat induced anisotropy variation affect the asymmetry or not, the sample with t_{Pt}=18.7Å sample was annealed at 200°C in vacuum for 30 minutes. Then its H_K

as well as the DW motion asymmetry were measured. We observed that the annealed sample has lesser anisotropy. This is due to with the Pt-Co inter-diffusing. On the other hand the asymmetry remains almost unchanged (Figure III.9. d). The only consequence of the anisotropy variation is that the DW width might vary from sample to sample. However, since it depends on the square root of the anisotropy field, its variations will not exceed 10%. Consequently, the DW demagnetizing field stabilizing the Bloch DW structure will vary by the same ratio. In the absence of DMI, H_{sat} is given by the DW demagnetizing field. The fact that we do not detect any significant sample-to-sample variation of H_{sat} is consistent with this scenario

III.2.2.3. The idea of chiral damping

The magnetization dynamics can be mathematically described using the phenomenological Landau–Lifshitz–Gilbert (LLG) equation. As discussed in chapter I, the LLG equation for the field induced DW motion contains two terms: an energy term expressing the effective field and a dissipation term reflecting the damping rate. Since there is no other type of term in the LLG equation, the phenomenon responsible for the DW motion asymmetry must be either dissipative or conservative. This means that the asymmetric modification of the domain wall velocities is either due to the differences in the energies of the two DWs or the difference in their damping or their combined actions. While the possibility of chiral energy has been widely studied and we now know that chiral energy can be modeled by an additional effective field (H_{DMI} fixing the DW chirality), the hypothesis of the chiral damping mechanism has never been reported or studied.

In order to accurately probe this possibility the energy and dissipative contributions to DW motion need to be accurately separated. For this, we used the well-known creep scaling law.

III.2.2.4. The creep scaling law

According to the creep scaling law, at creep regime, the variation of the DW velocity with respect to the applied driving field H_z can be written as

$$v = v_0 \exp\left[\left(-\frac{U_c H_P}{K_B T}\right)^{1/4} . H_z{}^{-1/4}\right] \qquad \text{(III.1)}$$

Where, U_c is the height of the pinning barrier and H_p is the pinning field.

The prefactor v_0 can be written as

$$v_0 = d_0 f_0 \exp\left(C \frac{U_c}{K_B T}\right)^{1/4} \qquad \text{(III.2)}$$

Where $C \approx 1$ is an empirical constant, d_0 is the average distance between two pinning centers, f_0 the attempt depinning frequency.

$$v_{DW} = d_0 f_0 \exp\left(-\frac{E}{K_B T}\left({H_z}^{-1/4} - {H_c}^{-1/4}\right)\right) \quad \text{(III.3)}$$

where $E = {U_c H_p}^{1/4}$ represents all the energy term and $H_c = H_p / C^{-4}$ gives the critical field that determines the limit of the creep regime.

According to the above equation, the exponential term contains all the energy terms. The damping only affects the prefactor $d_0 f_0$. Using the above equation, a logarithmic linear equation can be written as follows

$$\ln(v_{DW}) = ln\,(d_0 f_0) - \left(-\frac{E}{K_B T}\right)\left({H_z}^{-\frac{1}{4}} - {H_c}^{-\frac{1}{4}}\right) \quad \text{(III.4)}$$

By measuring the DW velocity variation with respect to H_z, one can plot a linear graph according to the equation III.4. Here the slope of the graph gives the energy of the system and the intercept can give the information about the attempt frequency. The attempt frequency depends on the damping (explained in detailed in the section III.2.2.6)

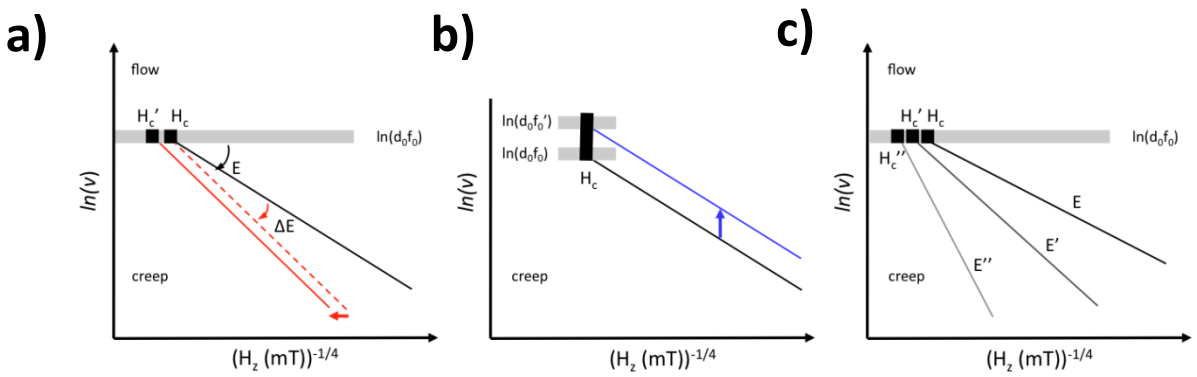

Figure III.10 Influence of energy barrier and attempt frequency on the DW creep scaling law. **a)** The variations of the pinning barrier lead to a change of slope (red dotted line), but also to a lateral shift due to a change of the pinning field. The horizontal gray line represents the approximate transition from creep to flow. The black square is the approximate $H_c^{-1/4}$ **b)** The variation of the attempt frequency leads only to a vertical shift of the curve. **c)** The graph for 3 systems with different energies (E, E', and E''). Due to difference in their slopes, they join at the intercept value ln (v_0). The order of magnitude of $H_c^{-1/4}$ and $d_0 f_0$ can be roughly estimated from this intercept.

Depending on the differences in the energy barriers and the attempt frequencies of the domain walls, the different linear plots can be obtained as shown in figure III.10. If one

varies the pinning barrier of a DW, it leads to the change of the slope as well as a lateral shift due to the change in the pinning field. (Figure III. 10. a). On the contrary, the attempt frequency does not produce any variation of the slope; it only shifts the curve vertically (figure III.10.b).

In summary, by measuring the variation of the DW velocity by varying the H_z and plotting the graph according to the equation III.4, one can extract the information about the energy and damping of the DWs. Therefore, we decided to study the asymmetric DW motion for different H_z for a constant H_{ip}.

III.2.2.5. ln (v) v/s H_z (for a constant H_{ip})

The asymmetric DW motion was studied in two samples, Pt $_{(30Å)}$ /Co $_{(6Å)}$/ Pt $_{(15.6Å)}$ and Pt $_{(30Å)}$ /Co $_{(6Å)/}$ Pt $_{(30Å)}$, for different H_z at a constant H_x. The measurements were done for H_x = 80mT, which is above the H_{sat}. The corresponding plots for the velocity variation of the two DWs ($V_{\uparrow\downarrow}$ and $V_{\downarrow\uparrow}$) are shown in figure III.11. The variation of the velocities in the absence of the H_{ip} is also plotted (black curve). From the figure, it is clear that the two DW velocities (blue and red plots) are differed by a linear shift. The slopes of the two graphs are unchanged. This indicates that the energies of the two DWs are the same. The difference in the DW velocities originated from the difference in their intercept. The intercept is defined by d_0f_0. i.e, the two DWs should have different attempt frequencies.

For the further confirmation of the asymmetric DW motion depends on the energy or not, from the graph, the asymmetric (A_{creep}) and the symmetric component (S_{creep}) of the DW motion can be written as

$$A_{creep} = \ln(v^{80mT\uparrow\downarrow}) - \ln(v^{80mT\downarrow\uparrow}) \qquad \text{(III.5)}$$

$$S_{creep} = \ln(v^{0mT}) - \frac{1}{2}\ [\ln(v^{80mT\downarrow\uparrow}) + \ln(v^{80mT\uparrow\downarrow})] \qquad \text{(III.6)}$$

According to III.4 they can be written

$$A_{creep} = \ln(\frac{{d_0f_0}^{80mT\uparrow\downarrow}}{{d_0f_0}^{80mT\downarrow\uparrow}}) - ({H_z}^{-\frac{1}{4}} - {H_c}^{-\frac{1}{4}})\ \left[\frac{E^{80mT\uparrow\downarrow} - E^{80mT\downarrow\uparrow}}{K_BT}\right]) \qquad \text{(III.7)}$$

$$S_{creep} = \ln(\frac{{d_0f_0}^{80mT\uparrow\downarrow}}{\sqrt{{d_0f_0}^{80mT\downarrow\uparrow}{d_0f_0}^{80mT\uparrow\downarrow}}}) - ({H_z}^{-\frac{1}{4}} - {H_c}^{-\frac{1}{4}})\ \left[\frac{E^{0mT} - \frac{1}{2}(E^{80mT\uparrow\downarrow} + E^{80mT\downarrow\uparrow})}{K_BT}\right] \qquad \text{(III.8)}$$

The A_{creep} and S_{creep} variation with respect to the H_z is shown in figure III.11 inset. The A_{creep} is independent of the H_z indicating that the asymmetry is not due to the chiral energy ($E^{80mT\uparrow\downarrow} = E^{80mT\downarrow\uparrow}$). At the same time, since S_{creep} varies with H_z confirms that the non-chiral energy contribution to the DW when H_{ip} is applied ($E^{80mT\uparrow\downarrow} = E^{80mT\downarrow\uparrow} \neq E^{0mT\downarrow\uparrow}$).

In the creep regime, the DW motion is dominated by the pinning and depinning events. Instead of a continuous flow, the DW hops between the consecutive pinning centers. The time duration of the pinning is generally very longer than that of the hopping. i.e, the DW velocities are largely determined by the time it spends at the pinning regime or it depends on the attempt depinning frequency (f_0). Both energy and damping can contribute to the f_0 [Ferré J 2013]. Since the energies of the two DWs are same here, it can be concluded that the difference in the attempt frequency originates from the difference in their damping

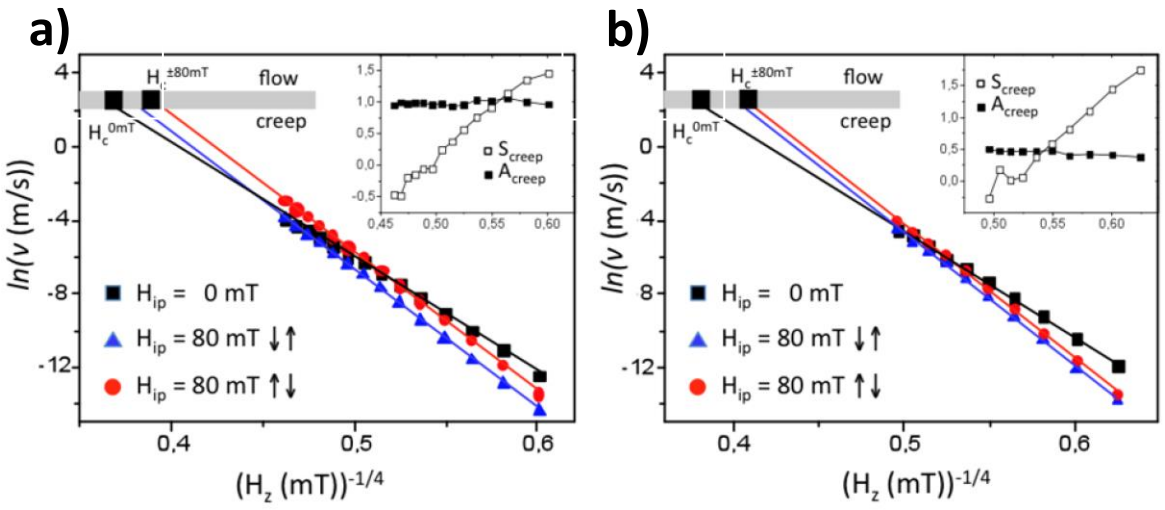

Figure III.11. The ln(V) vs $Hz^{-1/4}$ graph for the sample **a)** Pt $_{(30Å)}$ /Co $_{(6Å)}$/ Pt $_{(15.6Å)}$ **b)** Pt $_{(30Å)}$ /Co $_{(6Å)}$/ Pt $_{(30Å)}$. The graph for H_{ip}=0mT is shown in black. The plots for up/down and down/up DWs at H_{ip} = 80mT is shown red and blue respectively. In both cases, the slopes of the linear graphs are same indicating the energy of the DW velocities are same. The inset show the variation of the S_{creep} and A_{creep} defined by the equations III.5 and III.6.

Our data does not allow obtaining an accurate determination of $H_c^{-1/4}$ and d_0f_0 because the slopes of the different curves are very close to each other, and therefore their intercept is not precisely defined. In order to extract the order of magnitude of the d_0f_0, we rely on the previous measurements of the DW velocity in Pt/Co/Pt samples done by Metaxes *et al*[1] [Metaxes 2007] and Gorchon J. *et al* [Gorchon 2014] . (figure III.12) They studied the creep motion for different Pt/Co/Pt samples with varying Co thickness. The changes in the Co thickness lead to large changes in the energy landscape (exchange, anisotropy etc). Because of this, the ln (v) vs. $H_z^{-1/4}$ curves for the different samples converges into a small area. This

area allows estimating the range of the $H_c^{-1/4}$ and corresponding value of the d_0f_0. The different samples that we studied are nominally identical and were deposited using the same technique (sputtering) under the same conditions as these previous studies [Metaxes 2007] [Gorchon 2014].We obtain a value of d_0f_0 of ~ 10m/s. Considering this value, we estimate that the deviation from the linear behavior of the creep scaling law should occur at ln (v) ~2.5. By considering the disorder correlation length (d_0) should be larger than the typical grain size (20nm), the order of the attempt frequency (f_0) could take a value between 10 MHz to 1GHz.

To conclude, using the creep scaling law we experimentally prove that the asymmetric domain wall motion is due to the chiral dissipation; not due to the chiral energy. The damping can modify the f_0 values that modify the DW velocity. To prove this we decided to check the relation between damping on the f_0 using micromagnetic simulation. This will be described in the next section.

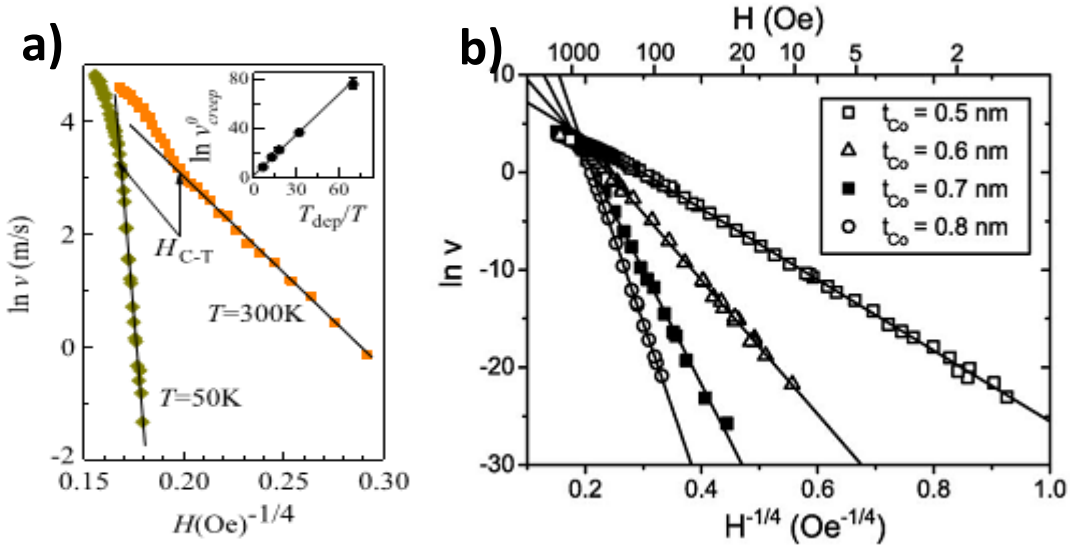

Figure III.12. The ln(V) vs $Hz^{-1/4}$ graph for the Pt/Co/Pt samples with different Co thicknesse **a)** Measurement Gorchon J. *et al* [Gorchon 2014] **b)** by Metaxes *et al*[Metaxes 2007] From both measurements the value of ln(V_0), where the DW velocity variation deviates from the creep scaling law is estimated to be ~2.5 m/s.

III.2.2.6. Numerical modelling

In literature, there is no known precise microscopic mechanism that links the damping to the attempt frequency, f_0. We verify this possibility using 2D micro magnetic simulations. The simulation was done by Liliana Prejbeanu at SPINTEC.

During the creep motion, since the DWs are generally trapped most of the time on the pinning centers, the velocity of the DW is proportional to the average depinning time. To implement this, DW depinning time from a single defect for different damping values were calculated. We indeed observe that the releasing time of the DW depends on the damping values (figure III.13.a). Since the barrier height is kept constant in the simulations, it is only f_0 that can be responsible for this variation. We find that f_0 is proportional to the inverse of the damping (DW mobility, $v_{DW} \propto 1/\alpha$).

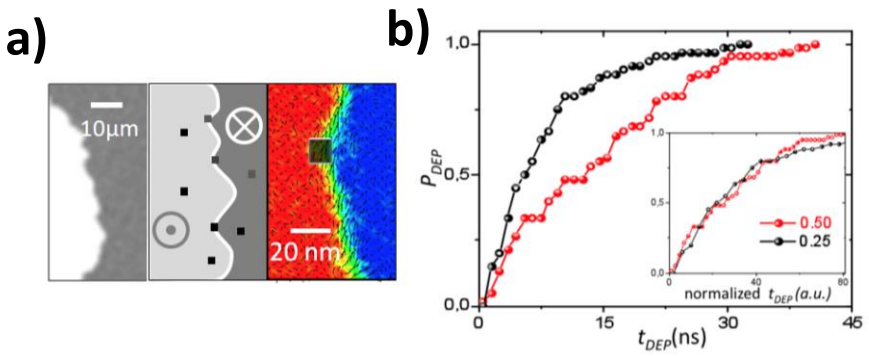

Figure III.13. a) Design of Micromagnetic model. The first picture is the Kerr differential image of the propagated DW. The second picture is the schematic diagram of the localized pinning centers that create ripple like DW shape according to the Kerr image. Third picture is a Micromagnetic configuration of a pinned DW in a 100 nm wide nanowire pinned at a defect. The pinning center is indicated by the rectangle designates an area with 50% smaller anisotropy that traps the DW. **b)** The graph showing the variation of the depinning probability, P_{DEP} (for 60 independent events) with respect to the time for two damping values: $\alpha = 0.5$ (shown in red) $\alpha=0.25$ (shown in black) at Hz= 18mT. The inset shows that the curves overlap when the timescale is normalized by the damping constant. This indicates that f_0 is proportional to the inverse of the damping.

Because micromagnetic simulations are time consuming, we completed our study using a simpler and much faster 1D model. While 2D micromagnetics allow including realistically the partial pinning of the DW, by definition in the 1D models the entire DW is enclosed in the pinning potential. As a consequence, when projecting the 2D DW dynamics onto a single dimension, the effective pinning potential needs to be adapted accordingly. The simplest way

to model the partial pinning of the DW is to use effective pinning centers that are much wider than the DW, such that the DW will have to shift far from the energy minimum before actually applying pressure on the pinning potential

In order to probe the influence of the damping variation on the thermally activated DW motion, we calculate the velocity (Figure III.14) as a function of the perpendicular magnetic field, for several damping values. The DW parameters used in the simulations are ΔDW=5nm, H_{dip}=40mT. The effective pinning field is modeled by a sinusoidal function with a period of 50nm, (10 times larger than the DW width) with amplitude of 3 mT. This form of pinning is chosen only for ease of implementing in the numerical model. Though it is not realistic for the quantitative calculation of the DW velocity, since it allows modeling the repeated pinning and de-pinning of the DW, it is sufficient to evidence the impact of damping on the DW velocity. We observe that the DW velocity depends strongly on the damping value (0.2, 0.4, 0.6). Moreover, by normalizing all the velocity curves by the inverse of the damping (proportional to the DW mobility) they overlap (figure III.14.a). This indicates that the DW velocity depends on the intrinsic DW mobility. On the contrary, when trapping the DW in a narrow potential well with the same barrier height (period of 2.5 nm and amplitude of pinning field of 60 mT) the velocity curves completely loose the damping dependence (figure III.14.b).

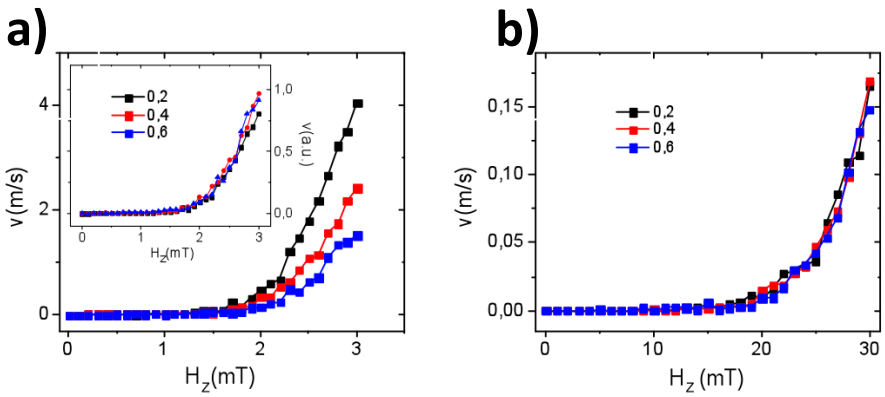

Figure III.14. DW velocity in the 1D model for 3 different damping values. Each velocity point is obtained after averaging 30 displacements produced by 500ns long pulses **a).** DW velocity when the width of the pinning potential is 10 times larger than the size of the DW (5nm). The inset shows the velocity curves normalized by the inverse of the damping value. **b).** The velocity calculated for a potential half the width of the DW (5nm). In this case, the DW velocity is independent of the damping value.

III.2.2.7. The dependence of the asymmetry on DW velocity (or for different Hz)

As discussed in the last section, the asymmetry is independent of the value of H_z or corresponding velocity of the DW motion. In order to check this, we repeated the DW velocity measurements for the Pt $_{(30Å)}$ /Co $_{(6Å)/}$ Pt $_{(15.6Å)}$ samples for a wide range of H_z. This is shown in figure III.15.

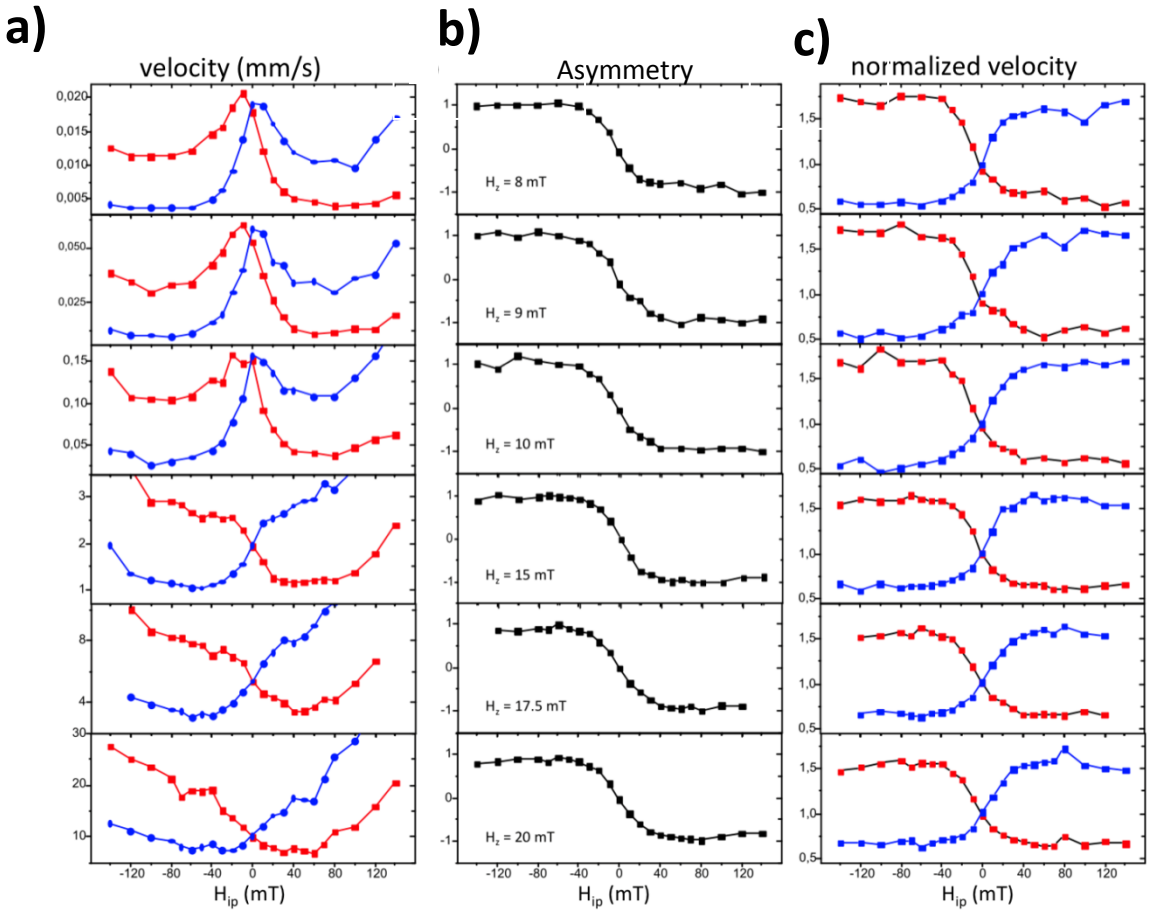

Figure III.15. Dependence of the anti-symmetric component ***A*** on H_z. **a)** Velocity curves for different values of H_z. **b.)** The corresponding $A_{raw} = 2(v_{\downarrow\uparrow} - v_{\uparrow\downarrow})/(v_{\downarrow\uparrow} + v_{\uparrow\downarrow})$. **c)** The normalized velocities.

Two important features are apparent on from this study:

1) The asymmetric components to the DWs showed the same behavior independent to the H_z values

2) Increasing the H_z value changed the overall shape of the velocity graph.

Since the asymmetric component is always the same, these changes are due to the variation of the symmetric components to the velocity. This result confirms the Hz dependence of S_{creep} and the H_z independence of A_{creep} studied previously. The fact that the anti-symmetric component is independent of Hz further confirms our conclusion that its origin is not related to energy but to damping.

III.2.2.8. Mathematical description of chiral damping

The lnV v/s H_z shows that the velocity asymmetry is not due to the chiral energy, but to chiral damping. In the presence of the H_{ip}, the H_z driven up/down and down/up DWs experience a different damping. The chiral damping is possible if the damping coefficient (α) depends on the orientation the DWs core magnetization with respect to the magnetization gradient. Mathematically it can be written as,

$$\alpha \propto \alpha_c \, (\overrightarrow{m_{ip}} . \nabla m_z)$$

where α_c is the coefficient of chiral damping and m_{ip} is the core magnetization along the H_{ip} direction. For the up/down and down/up DWs the chiral contribution will have the opposite sign. However, this kind of damping cannot exist by itself in a real physical system since it is possible that the overall dissipation may become negative if the chiral contribution exceeds the intrinsic damping. To prevent this unphysical behavior, the chiral damping must include at least a second component, which always offsets its value in the positive range. Then the final expression for the chiral damping becomes

$$\alpha \propto \alpha_0 + \lambda_{ex} \, \alpha_c \, (\overrightarrow{m_{ip}} . \nabla m_z), \text{ where } \alpha_0 > \alpha_c$$

Where λ_{ex} is exchange length (constant value). In the general case the coefficients α_0 and α_c depend on absolute value of magnetization gradient such that $\alpha_0 > \alpha_c . \lambda_{ex} \, |\nabla m_z|$).

III.2.2.9. DW velocity v/s H_{ip} according to the collective model

To establish the influence of the chiral damping on the DW motion, the DW velocity variation was studied using the numerical collective coordinate model. Since such models do not include explicitly the magnetization gradients, we write the chiral damping using a simplified form: $\alpha \propto \alpha_0 + \alpha_c \cos\varphi$. Here the value of the magnetization gradient is considered constant and is implicitly included in the values of α_0 and α_C. The orientation of the DW magnetization is described by the azimuthal angle ϕ.

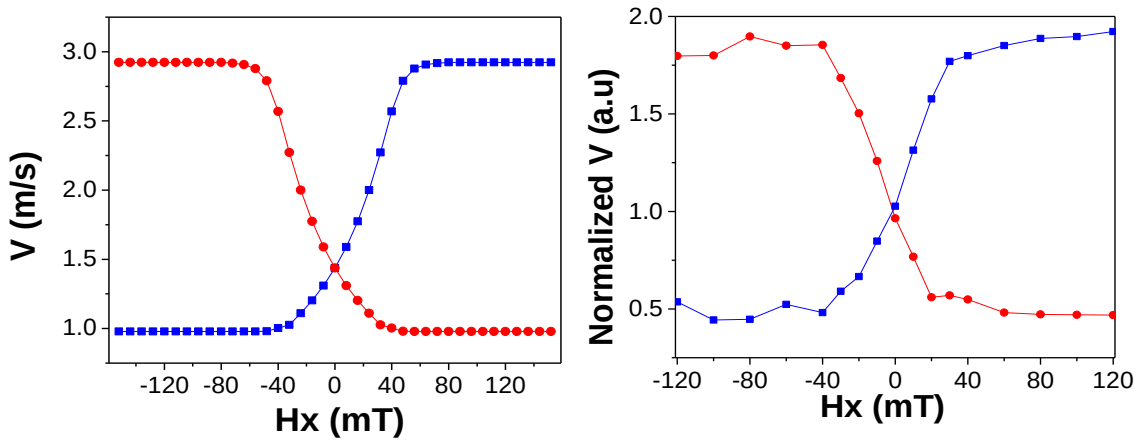

Figure III.16.a) The variation of the calculated DW velocity vs H_{ip} obtained using the numerical model at a temperature 0K. As shown in the figure, the velocities increase monotonically when H_{ip} increases. After a certain field both DW velocities saturates simultaneously, at the field value where their core magnetization saturates. The values used in this calculation are α_0=0.6, α_c=0.3, ΔDW=5nm, H_{dip}=35mT, H_z=0.01mT **b)** The normalized graph, the symmetric component of the measured velocity is removed as it is not produced by the chiral damping. The numerical graph in figure a is comparable with this experimentally measured normalized velocity graph.

III.2.2.10. Conclusion

We have performed a detailed quantitative study of the asymmetric bubble domain expansion in Pt/Co/Pt system in presence of H_z and H_{ip}. Previous studies reported that the DW motion asymmetry due to the presence of the DMI. In our study, the detailed analysis of the anti-symmetric and the symmetric components of the DW velocities, showed deviation from the homo-chiral Néel wall behavior. Thus we concluded that in our system, the DW has mostly Bloch structure. Then using the creep scaling law, we have compared the contribution of the energy and damping to the domain wall velocity. We found that the anti-symmetric domain wall motion is due to the chiral dissipation, not chiral energy.

In order to explain the asymmetry in the DW velocity, we introduce a new damping term in the LLG equation. The influence of the chiral damping on the DW dynamics is verified by numerical modelling. The results from simulations are compatible with the experimental data.

At this stage, we do not know why the effect of chiral damping is dominant over DMI in our samples. In general these two phenomena should co-exist. The relative strength of the two effects may depend on the precise material parameters (crystallographic structure).

While the physical origin of the DMI is well known, the origin of the chiral damping mechanism is not clear. Extensive theoretical studies are required to understand the mechanism that gives rise to the chiral damping. Nevertheless, we would like to propose a possible path towards an explanation. It is well known that the SOTs have two components: Field like and damping like. Theoretically DMI is associated with the conservative (field) like component. Similarly, the chiral damping can be the reminiscent of the dissipation component. Concerning the microscopic mechanism of the chiral damping, just like in the case of the current induced spin orbit torques, there can be multiple contributions from different phenomena. Among these possibilities, besides the DMI, it could also emerge from the Rashba interaction and more generally from any form of SO coupling that includes inversion symmetry breaking.

Despite the unclear mechanism, the discovery of the chiral damping opens new possibilities for controlling the DW motion in materials with large spin orbit coupling. Furthermore, due to its expected co-existence with DMI, it can play an important role in understanding the dynamics of the chiral magnetic spin textures like skyrmions, DWs etc.

III.2.3.Discussion on similar experiment reported in literature:

The incompatibility of the DMI model to explain the asymmetric DW motion was also reported by Lavrijsen et al [Lavrijsen 2015]. Using dc sputtering technique, they deposited different SiO_2 /Ta/$Pt_{(4nm)}$ /$Co_{(0.6nm)}$ /$Pt_{(4nm)}$ trilayer samples. In these samples, during the deposition of the upper Pt layers, different Ar gas pressures (P_{top}) were used such that each sample had different growth kinetics. At first, they measured the effective anisotropy field ($H_{K,\,eff}$) of each sample. They found that for the samples with P_{top}=0.29 Pa to P_{top}=2.80 Pa, the $H_{K,\,eff}$ values varied by a factor 3 (figure III.17.a). This indicates the different interfacial quality or degree of intermixing of the samples that leads to different SIA. After, they measured the DW velocity with respect to the H_z field and confirmed the creep behavior of each sample (figure III.17b) following the creep equation

$$v = v_0 \exp(-\chi H_z^{-\frac{1}{4}}) \qquad \text{(III.10)}$$

where v_0 is the prefactor and χ indicates the energy of the system.

After, they studied the asymmetric DW motion behavior in presence of out of plane and in plane field (H_x) for each samples and DW velocity (v) *vs* H_x graph. The shape of the graphs showed features similar to my observations (figure III.18.a) showing incompatibilities with the simple DMI model. As well as, from the minima of the same graph, the DMI fields of each sample were measured. For samples with different P_{top}, since their $H_{K,\,eff}$ were different indicating their micro-structural differences, different DMI values were expected. Contrary to

this, a constant DMI field (60mT±10mT) for all the samples was observed. This also questioned the applicability of DMI model to explain the asymmetric DW motion.

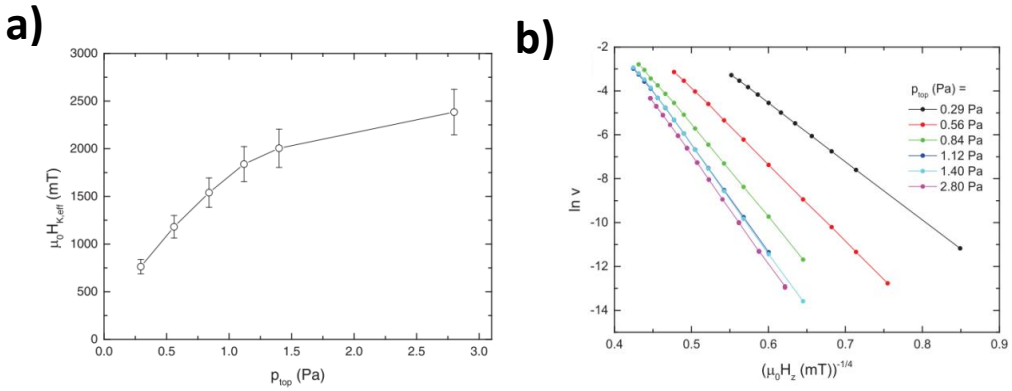

Figure III.17.a) The variation of effective anisotropy ($H_{K,eff}$) with respect to the variation Ar pressure used for the deposition of top Pt layer (P_{top}). For the samples with smaller and higher P_{top}, the $H_{K,eff}$ varies by a factor~3. b) The graph showing variation of ln V with respect to the variation of $H_z^{-1/4}$. The linear behavior confirms that the sample behaves according to the creep scaling law. [Lavrijsen 2015].

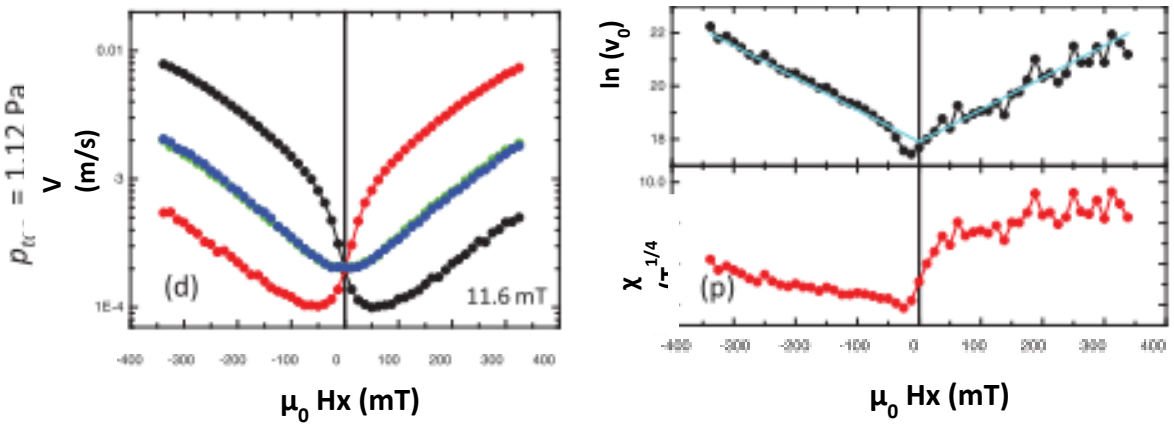

Figure III.18. a) The variation of DW velocity with respect to H_x, the red, black, blue and green curves corresponds the DW motion along +X,-X,+Y,-Y directions. Similar to my observations, the two velocity graphs (black and red) shows features not corresponds to DMI. b) The variation ln v_0 *vs* H_x (black curve) and χ *vs* H_x (red curve) extracted according to the equation III.10. The ln V_0 varied symmetrically for $\pm H_x$. On the other hand the variation of χ was asymmetric indicating the asymmetric energy variation to the DWs [Lavrijsen 2015].

To differentiate the chiral energy and chiral damping contributions, following the similar procedure that I used, they plotted graph of ln v_0 *vs* H_x and χ *vs* H_x. However, contrary to our conclusion, they observed asymmetric energy and symmetric damping contributions (figure III.18.b) to the DWs. Therefore they concluded that neither the chiral damping nor the simple DMI model can explain the complete picture of the asymmetric bubble expansion in Pt/Co/Pt.

Even though their analysis to differentiate between chiral energy and damping appears to be similar to us, there is a major difference: In their studies, they extracted the pre-factor ln v_0 at $H_z^{-1/4}=0$ (from the equation III.10). In our case, we measured the pre-factor at $H_z^{-1/4}= H_c^{-1/4}$ according to the equation (III.18) considering the studies proposed by Gorchon et al [Gorchon 2014] . If we apply our analysis to their results, we find that in their case, both the slope and the intercept of ln (v) *vs* $H_z^{-1/4}$ should be different (figure III.19). Therefore we can conclude that, their results clearly exhibit the signature of chiral energy contibution; but they cannot exclude the chiral damping contribution.

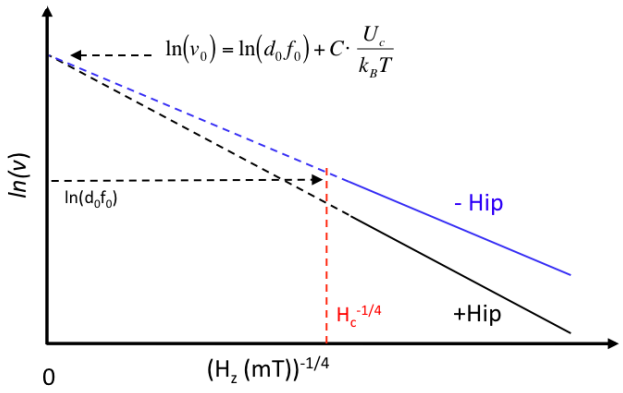

Figure III.19. Schematic diagram showing the difference between extractions of value of prefactior at $H_z^{-1/4}=0$ and $H_z^{-1/4}= H_c^{-1/4}$. Lavarijsen et al [Lavrijsen 2015] extracted the value of prefactor at $H_z^{-1/4}=0$ where for both $+H_{ip}$ and $-H_{ip}$ the values of pre-factors appear to be same. But the same graph give different pre-factors at $H_z^{-1/4}= H_c^{-1/4}$ (red dotted line) . Therefore, Lavarijsen et al cannot exclude the possibility of the asymmetric contribution to the pre-factor and they does not exclude the possibility of chiral damping.

It is possible that some of the samples used in their experiment exhibit DW motion asymmetry similar to our samples. However, since they used different growth conditions that changes the microstructure of top Pt layer, contrary to our case, they have different observation where chiral energy plays an important role.

III.3. Comparison: Asymmetric bubble domain expansion in Pt/Co/AlOx and Pt/Co/Pt

In order to understand how the asymmetric bubble expansion behaves in creep and flow regimes, I have performed the study of the asymmetric DW motion at large H_z. We observed a significant difference between the behaviors of the anti-symmetric component for Pt/Co/AlOx and Pt/Co/Pt. The detailed experimental results and possible conclusions are described in this section.

III.3.1. Asymmetry v/s Hz (at constant Hx)

In order to apply large H_z, the micro coil was used (a detailed explanation about the micro coil set up is described in section II.3.1). The asymmetric DW displacements for a constant H_x were imaged using MOKE microscope. The H_{ip} field used for the $Pt_{(30Å)}$ /$Co_{(6Å)}$ /$Pt_{(15.6Å)}$ was 80 mT and that for $Pt_{(30Å)}$/$Co_{(6Å)}$/AlO_x was 100 mT. The corresponding images are shown in figure III.20. For the higher H_z values, for Pt/Co/Pt the experiments were affected by the adjacent nucleation (figure III.20.a). This is why we used slightly smaller H_{ip} field value for Pt/Co/Pt compared to Pt/Co/AlO_x.

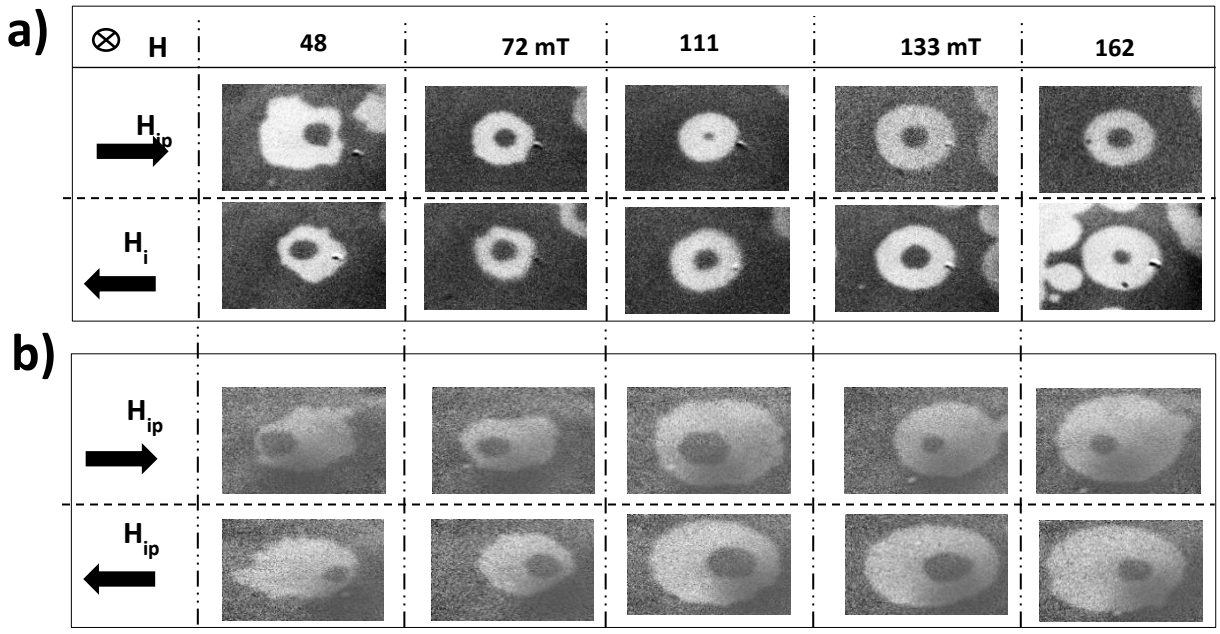

Figure III.20. The MOKE differential images of the asymmetric expansion of a down magnetic domain for a constant H_{ip} by varying H_z **a)** for Pt/Co/Pt at H_{ip} = 80 mT. Here the asymmetry disappears at large H_z field **b)** for Pt/Co/AlO_x at H_{ip}=100mT. Here the asymmetry is preserved for all the H_z values.

A quantitative analysis of the DW displacement and asymmetry variation for the Pt/Co/Pt for H_{ip} = ±80mT is shown in figure III.21. The DW displacements along the ±x and ±y directions are plotted in figure III.21.a & b. The corresponding asymmetric variations with respect to the H_z values are shown in the figure III.21. c & d. We observed that the asymmetry disappeared 110 mT. Note that the data for $+H_{ip}$ and $-H_{ip}$ yields a slightly different values for the asymmetry. this is due to the inhomogeneity of Hz generated by the micro-coil.

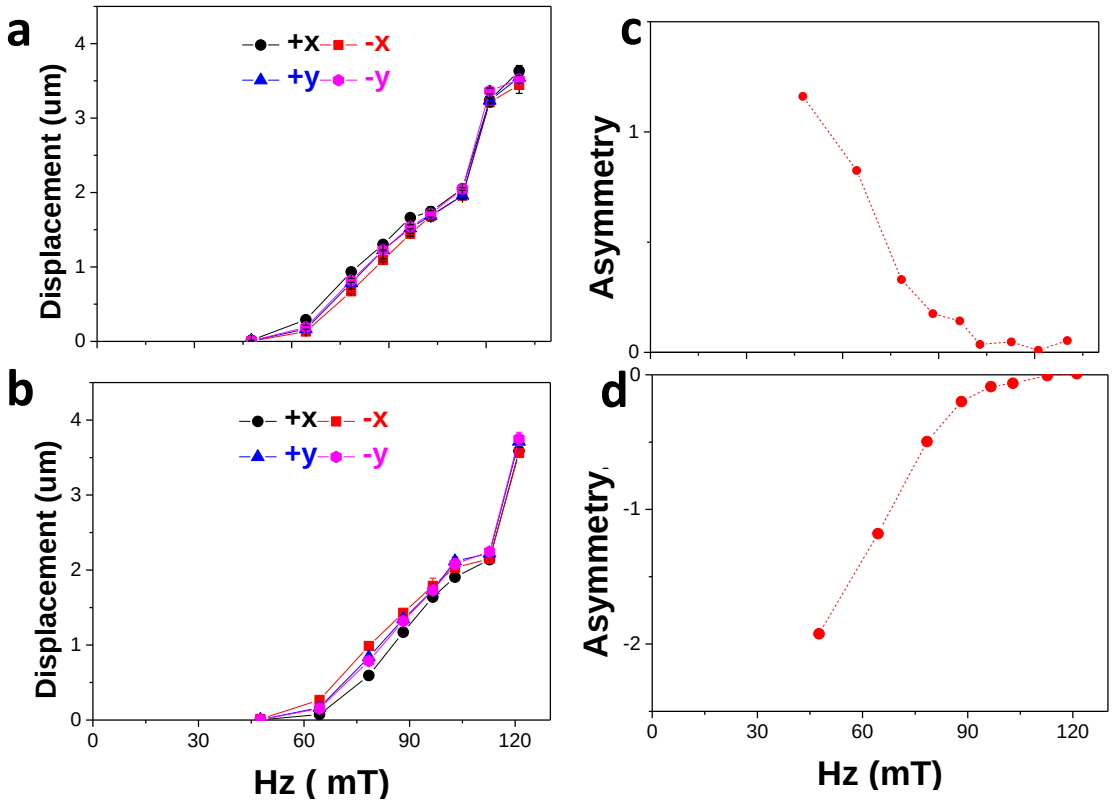

Figure III.21. The DW displacement vs. H_z for Pt/Co/Pt measured from the differential images in figure III.20. **a)** for H_x=-80mT **b)** for H_x=+80mT. Here the DW displacements along the axis of H_{ip} (±X axis) are different for low H_z values. They became equal at around H_z = 110 mT where the asymmetry disappears. **c, d)** The asymmetry vs. H_z plots for for H_x=-80mT and for H_x=+80mT respectively.

As shown in figure III.20, for Pt/Co/Pt, we observed that the asymmetry of the bubble expansion disappeared as the H_z was increased. On the other hand for Pt/Co/AlOx, the asymmetries always present for a large range of the H_z values. These observations are very interesting and need better understanding.

A possible explanation behind the asymmetry disappearance can be given based on the concept of the different regimes of the DW motion: steady state regime and oscillatory regime. This is explained in details in the following sections.

III.3.2. The Walker breakdown in Pt/Co/Pt and Pt/Co/AlO_x

In section I.5.2, I have described the different regimes of the DW motion. At smaller H_z field, the steady state DW motion is expected. As the H_z increased, the DW motion also increases. At a certain field called the Walker field, the DW motion becomes oscillatory. At this field, the DW velocity suddenly drops. In section I.5.3, I have explained the problem regarding the observance of walker break down. In the realistic experiments, for small H_z fields, the ideal behavior of the velocity curve may not necessarily be observed. This masks the velocity drop at Walker breakdown

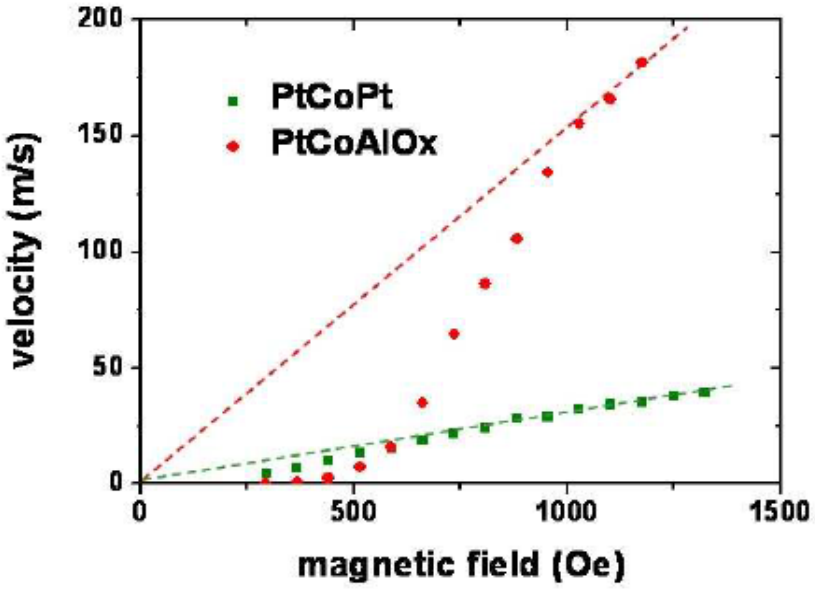

Figure III.22. The DW velocity vs. magnetic field graph measured by I.M. Miron [Miron 2009].. For the same field values, the velocity of the Pt/Co/AlOx (shown in red) is much larger than that of Pt/Co/Pt (shown in green)

The measurements of the field induced DW velocity v/s H_z in Pt/Co/Pt and Pt/Co/AlOx were already done in our lab in the thesis work of I.M Miron [Miron 2009]. The corresponding graph is shown in figure III.22. For both cases, the DW velocity shows an exponential behavior for the small H_z field and then becomes linear. Since the sudden velocity drop of the walker breakdown in not observed here, it is difficult to directly identify the linear regime is corresponds to the steady state regime or to the oscillatory regime. However, the two velocity region can be differentiated by the DW mobility values. In the steady state

regime, the DW velocity varies inversely to the damping parameter (1/α). In the oscillatory regime, it varies with ($\frac{\alpha}{1+\alpha^2}$). i.e, the DW mobility for the steady state regime varies monotonically with α, while for the oscillatory regime it is limited by a maximum value. i.e, if the observed DW mobility is higher than the maximum value attainable in the oscillatory regime, it can be concluded that the linear regime corresponds to the steady state regime. In his observation, I.M. Miron observed that the DW velocity for the Pt/Co/AlOx is much higher than that of Pt/Co/Pt. By analyzing the DW mobility values, it was concluded that the linear regime for Pt/Co/AlO_x is corresponds to the steady state regime, while that for the Pt/Co/Pt corresponds to the turbulent motion.

The asymmetry disappearance we observed can be explained based on these different velocity regimes.

III.3.3. The asymmetry disappearance due to the Walker breakdown

In the steady state regime, the internal structure of the DW does not change with time. On the other hand, in the turbulent regime the DW transforms continuously between Néel and Bloch. When we apply H_{ip} along with the H_z, the H_{ip} can only align the DW in its direction if the DW motion is in steady state. In the turbulent regime, since the magnetization oscillates, H_{ip} is expected to not have any significant effect. The asymmetric DW motion, according to both the DMI and chiral damping mechanism, is proportional to the magnetization in the H_{ip} direction (m_{ip} component). This indicates that the asymmetric bubble expansion only occurs in the steady state regime, while it should disappear at Walker breakdown.

We have observed that the asymmetry disappearance only occurs in Pt/Co/Pt, not in Pt/Co/AlO_x. This can be understood considering that for the case of the Pt/Co/AlO_x the Walker breakdown occurs at large H_z (DWs move in the steady regime) while in Pt/Co/Pt it occurs at small H_z (DWs move in the turbulent regime).

One important thing to specify here is, for the case of the Pt/Co/Pt, the field at which the asymmetric DW motion disappears is the field DW motion becomes completely oscillatory. It may not necessarily be the walker breakdown field. As discussed extensively in this chapter, for small DW velocity region, the DW motion is a mixture of the pinning and depinning events. This means even though breakdown occurs, the oscillatory DW motion occurs only when the DW hops between two adjacent pinning centers. The H_{ip} can still create the asymmetric DW motion by modifying the time of the pinning. In this case, even after the Walker breakdown, the asymmetric bubble expansion can be observed. The disappearance of the asymmetry only signifies that the DW motion reaches the flow regime, without any pinning or depinning events.

As an application of this result, we can propose that asymmetric DW motion studies can be used as a standard tool to understand if the DW motion is steady state or oscillatory. This method only works for the material with SIA that exhibit asymmetric DW motion. Since simple velocity measurements in materials with significant pinning are generally not suitable for observing the Walker breakdown, verifying the asymmetric DW motion can serve as a simple method to discriminate turbulent and steady DW motion regimes.

III.3.4. Conclusion

In this section, I studied the variation of the DW motion asymmetry at large H_z. We observed that the asymmetry disappears at large field for Pt/Co/Pt, but not for Pt/Co/AlO_x. The asymmetry disappearance is linked to the position of the Walker breakdown. Therefore, in multilayer systems with SIA, the asymmetric bubble expansion method can be used as a tool to distinguish between steady and oscillatory DW motion.

III.4. Conclusion

In this chapter, I have mainly described my experimental studies of the DW motion in Pt/Co/Pt systems. At first, I explained the current induced DW motion measurements in Pt/Co/Pt wires. I showed that our observation contradicts the SOT+DMI model. This indicates that another possible mechanism can exist in the system. By analyzing the field induced asymmetric DW motion in the same system, we propose a new mechanism that can govern the DW dynamics: The chiral damping mechanism. I have presented both experimental and simulation studies proving the existence of the new mechanism. Finally, a comparative study of the field induced DW motion in Pt/Co/Pt and Pt/Co/AlOx was presented. We propose a new application of the asymmetric bubble expansion: we can use this method to distinguish between oscillatory and the steady state behaviors of the DW motion.

Chapter IV

Non-collinear current induced domain wall motion in systems with large SIA ($Pt/Co/AlO_x$)

A magnetic memory device requires two basic operations: reading and writing of the magnetic state. After the discovery of giant magneto resistance (GMR) [Baibich 1988] followed by the discovery of tunnel magneto resistance (TMR) [Miyazaki 1995], the reading of the magnetic data is considered as an easy task to build fast and high density magnetic memory devices. The major issue of improving the magnetic memories has been related to the writing of the magnetic bits. These last years, the magnetic memory industry has been highly focused in finding novel routes to optimize the writing process with less power consumption and high speed.

In order to change the magnetization state of a bit, instead of using the magnetic field, the torque induced by the electric current can be used. It combines several advantages like e.g. lower energy consumption and scalability. As discussed in chapter 1, two mechanisms of current induced spin torques are identified: STT and SOT. Based on both these two torque concepts, two kinds of magnetic memory devices have been widely studied: 1) The current induced DW motion based devices like race track memory device[Parkin 2008] where the magnetic bits are separated by the DW; 2) the magnetic random access memories (MRAMs) [Dieny 2010] where the magnetic bits are physically separated. The DW motion devices are mainly studied in micro-nano wires. The magnetic bits in MRAMs generally have pillar shapes (figure IV.1).

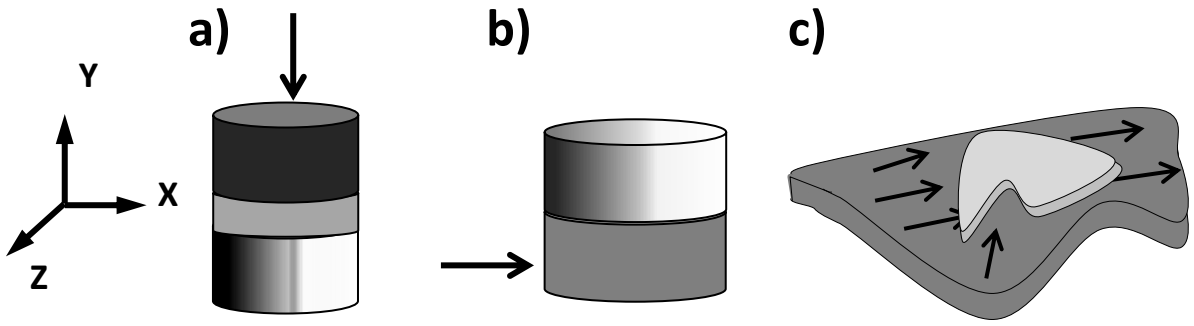

Figure IV.1. Schematic diagrams of **a)** The STT switching scheme: the magnetic bit has a pillar shape. The current direction is restricted to a single direction (perpendicular to the tunnel junction). **b)** The SOT geometry: the current is applied along the in-plane direction with respect to the magnetic bit. **c)** The new scheme for manipulating the magnetization. In the case of SOT, the source of spin torque is the SIA combined with the presence of the heavy metal. The idea is to play with an additional degree of freedom: the current direction is no more restricted by the geometry that defines the magnetic dot shape, both can be structured independently.

In the case of STT-MRAMs, the current is applied perpendicular to the plane of the thin film (along the Z axis as shown in the figure IV.1.a). The electrons spins get polarized

by the fixed layer and transfer their spin angular momentum to the free layer resulting in the magnetization reversal. On the other hand in the case of SOT, no spin polarization by a ferromagnetic layer is required. Under the in-plane current injection, the angular momentum is transferred from the heavy metal crystal lattice resulting in the magnetization reversal. Here, unlike the STT the current flow is no more restricted to a single direction (along Z), but it can be applied in any in-plane direction with respect to the pillar shapes (X & Y directions in the figure IV.1.b). In the case of STT, the pillar shape defines the current flow as well as the shape of the magnetic element. On the other hand SOT geometry allows decoupling of the two: The heavy metal electrode shapes the current flow, independently of the ferromagnetic layer. This liberty allows a new approach to control the magnetization reversal: the spatial distribution of the current induced torque (SOT (x,y)) can be freely shaped to control the temporal evolution of the magnetization (M(x,y,t)). In our experiment we wanted to verify this possibility.

In SOT-MRAMs, the magnetic bits are of few tens of nanometers, larger than the typical size of the DW width. Here the switching occurs through domain nucleation and DW propagation. Thus, in order to improve the magnetization switching, the DW motion should be controlled. More particularly, the study of the influence of the shape on the magnetization switching demands to study its influence on the DW motion. For this, I have studied the current induced DW motion in Pt/Co/AlO_x wires oriented along different angles with respect to the current direction. Based on the specific properties of this non-collinear current induced DW motion, I have developed a new kind of magnetic devices, where the shape allows to control the magnetization reversal

This chapter is divided into two parts: I will describe first the non-collinear current induced DW motion experiments and the possible physical mechanisms that could explain my results. In the second section, I will discuss about a new device concept called magnetic origami.

IV.1. Non-collinear Current induced DW motion

As presented in chapter I, in the case of the STT driven DW motion, the direction of the spin polarization of the electrons continuously rotates as they pass through the magnetization gradient. This rotation is linked to a transfer of spin angular momentum between the conduction electrons spins and the local magnetization. This transfer results in the DW motion. Here the torques acting on the DW do not depend on the direction of the magnetization inside the DW (Bloch or Néel). It only depends on the magnetization gradient profile. On the other hand, the SOT driven DW motion may strongly depend on the DW type (Néel or Bloch).

In the case of the SOT, the angle between the magnetization inside the domain wall with respect to the current direction as well as the direction along which the symmetry is broken (***z***), defines the strength of the effective fields that drive the DWs $\boldsymbol{H_{FL}} \sim \boldsymbol{z} \times \boldsymbol{j}$ and $\boldsymbol{H_{DL}} \sim \boldsymbol{m}\ X\ \boldsymbol{H_{FL}}$). By varying the angle, the action of the current on the DW can be tuned. In the case of STT, varying the angle decreases the current density passes through the domain and then reaches the DW. i.e., it decreases the spin polarization. In this case, as the non-collinearity between the current and the DW increases, a steady decrease in the DW displacement is expected.

In my experiments, I studied the DW displacement variation by applying current at different angles with respect to the DW. The details of my experiment, results and their consequences are explained in this section.

IV.1.1. The sample geometry

To introduce the non-collinearity, we fix the current direction and rotate the wire at different angles with respect to the current. For this, we fabricated Co/AlOx wires oriented in different directions on top of the Pt electrode (the fabrication process is described in chapter II. Since the Pt layer (3 nm) is much thicker than the Co layer (0.6nm), most of the current is expected to flow through the Pt under layer. A schematic diagram of the system that I have studied is shown in figure IV.2.b. It contains 7 wires whose ends are connected. When the current is applied along the sample, each wire presents a different angle with respect to the current. The angle of the wires varies from 0° to 90° in steps of 15°.

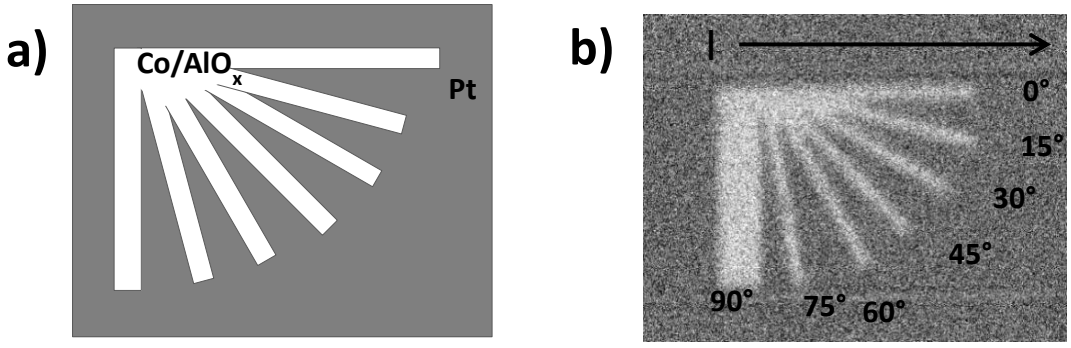

Figure IV.2. **b)** Schematic diagram of the structure used. The 7 different ferromagnetic Co/AlOx wires were fabricated on top of the Pt heavy metal. Each wire is connected to a common junction. **b)** The MOKE microscopy image of the saturated state of the wires structure confirming that only the wires part is magnetic. If one applies the current through the heavy metal layer (Pt), each of the wire presents a different angle with respect to the current direction. The angle of the wires varies from 0° to 90°, in steps of 15°.

IV.1.2. DW displacement measurements

The current induced DW motion in each of the wires is studied using MOKE microscopy (the experimental set up is described in chapter II). Initially, all the wires were saturated using a perpendicular magnetic field. Figure IV.3.a shows the case of the magnetization saturated in the downward direction (the white color contrast corresponds to the down magnetization state). The image confirms that only the wires are magnetic. When a current is injected along the direction represented by the black arrow, a small up magnetic domain is nucleated in the upper left corner of the wires system where all the wires are connected. Using a small propagation field, the nucleated domain was expanded such that the DW reaches each of the wires. Then, under the same current injection, the displacements of the DWs in each of the wires were observed. Figure IV.3.b shows a differential image of the DW motion induced by a positive current. The black color contrast corresponds to the displacement of the up/down DW. By reversing the current, the down/up DW motion was observed (figure IV.3.c). The magnetic image clearly shows a difference between the DW motion under the positive and negative current injection. The DW displacement strongly depends on the angle of the wires.

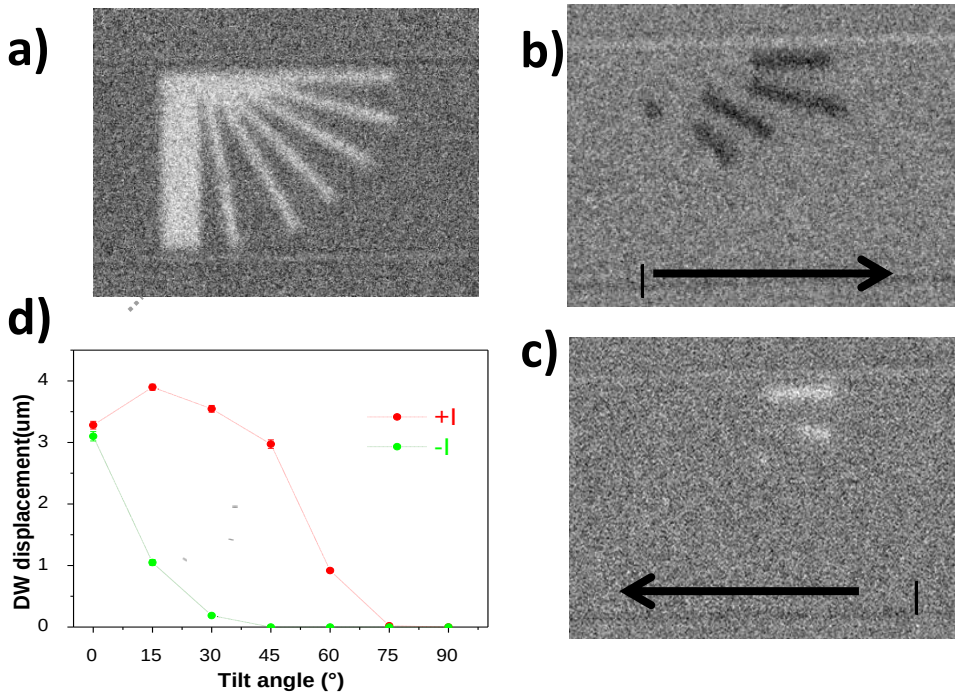

Figure IV.3. MOKE microscopy images of the Pt/Co/AlO_x wires in the non-collinear geometry**. a)** The down magnetic saturated state. **b)** The differential images of the up/down DW displacement under positive current injection. **c)** The down/ up DW motion under negative current injection. d) DW displacement with respect to the tilt angle of the wires. The displacements under the a positive (resp. negative) current are shown in red (resp. green). The current density is 1.75×10^{12} Am^{-2} and a series of 10 pulses of 2.62ns were applied.

For a better understanding of the DW motion under the non-collinear current, the DW displacement in each wire is quantitatively analyzed. Figure IV.3.d shows the variation of the displacement with respect to the tilt angle of the wire. The red curve shows the displacement of up/down DW under a positive current injection and the green curve shows that of down/up DW under a negative current injection. Here the current density used was 1.75×10^{12} Am^{-2}. As shown by the graph, the two domain walls move differently under the current injection. For the 0° wire both DW displacements are almost equal. As the tilt angle is introduced, the up/down DW moves faster compared to the down/up DW. The up/down DW displacement (red curve) increases and finds a maximum at around 15° and then decreases and vanishes around 90°. The 15° angle corresponding to the maximum DW displacement is an approximation since the angle is varied by in steps of 15°. For the down/up DW (green curve), the displacement decreases as the tilt angle is increased from 0° and it vanishes after 45°. This means that between 45°≤60°, only one of the DW moves.

To confirm that this angular dependence is a characteristic feature of the DW velocities rather than mere DW displacements, I have performed additional measurements. In order to measure the DW velocity, we followed the same procedure as discussed in section II.4. For each wire, DW displacements were measured at a constant current density (1.81×10^{12} Am^{-2}) for three different current pulse lengths. The DW displacement varies linearly with the pulse length as shown in figure IV.4. The slope of the linear dependence gives the DW velocity. The DW velocity versus the tilt angle (figure IV.4.c) behaves the same as the DW displacement shown previously

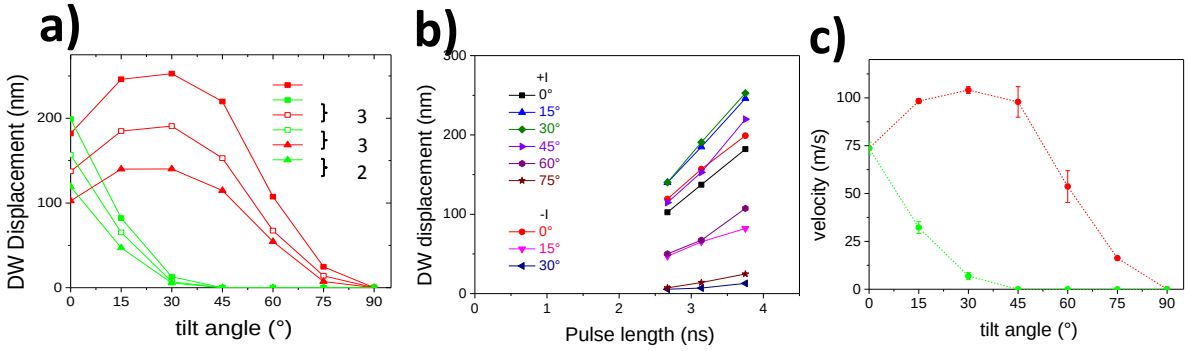

Figure IV.4. **a)** DW displacement with respect to the tilt angle for three different pulse lengths 3.75ns, 3.14ns and 2.76ns. The DW displacements corresponding to a single pulse are plotted. They are calculated by dividing the total displacement in each wire by the number of pulses injected for each case. **b)** DW displacement versus the pulse length for each wire. Note that for a negative current, there is no plot for wires with angles> 30° because the displacements were zero. **c)** DW velocity versus the tilt angle. The DW velocity value in this graph is obtained from the slope of the corresponding linear plot in figure b.

IV.1.3. DW motion along all the angles in two dimensions

In the previous section, I have described the DW motion in wires with angles varying clockwise from 0° to 90°. The same DW motion studies can be done in wires whose angles are varying anticlockwise from 0° to -90°. For this no additional experimental measurements are required. Results can be simply obtained from symmetry operations.

Figure IV.5 shows the results of the mirror symmetry operations applied on the wires system. The magnetization and the magnetic field are axial If the mirror is perpendicular to the Y axis (figure IV.5.a), the magnetization, parallel to this mirror, gets reversed. According to mirror symmetry, any effect associated with the up magnetized region in the first system should be the same for the down magnetized region in the mirror image system. As shown in figure IV.5.b, the sample with wires oriented from 0° to -90° is the mirror image of the sample with wires oriented from 0° to 90°. It implies that the up/down DW displacements in the wires oriented from 0° to 90° should be the same as for the down/up DW displacements in the wires oriented from 0° to -90°. In the figure IV.5, the green and red arrows represent the DW displacements according to the graph shown figure IV.3.d. This figure IV.5 shows the complete picture of both up/down and down/up domain wall displacements in wires oriented from -90° to 90°.

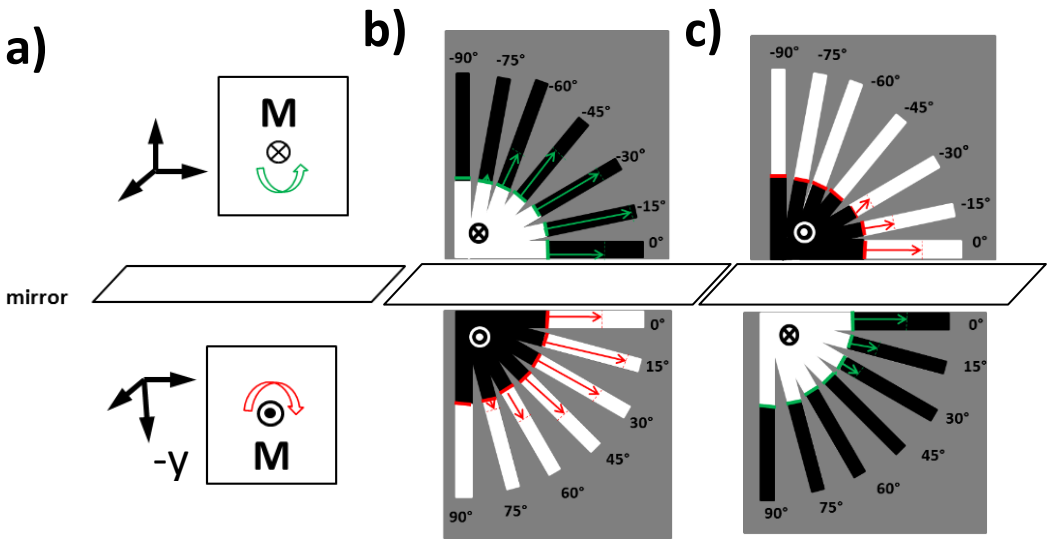

Figure IV.5. The mirror symmetry operations. a) Since magnetization is an axial vector lying in the plane of the mirror, the up magnetized region will be changed in a down magnetized region in the mirror image. **b)** The down/up DW displacements represented by length of the green arrows are changed in up/down DW displacements represented by the length of the red arrows and vice et versa **c)**. The resulting figure represents the complete picture of the DW displacements in wires oriented from -90° to 90°. According to this complete picture, the DW motion is asymmetric with respect to the current direction and the up/down and down/up DW displacements show opposite asymmetry with a maximum displacement at +15° for the up/down DW and -15° for the down/up DW.

By analyzing the complete picture of the DW displacements in figure IV.5, it is clear that the DW moves asymmetrically with respect to the current direction. The maximum DW velocity for up/down DWs is skewed towards positive angles and that for the down/up DWs is towards negative angles (figure IV.6.a & b)

IV.1.4. DW motion in a magnetic pad

Before discussing the possible physical mechanisms behind the asymmetric DW motion observed in the wires, we should first confirm that the observed phenomenon is not an artifact. There are two possible artifacts associated with the experiments. 1) Since I used an unconventional sample structure where the heavy metal and the ferromagnetic wires were shaped separately, we can wonder whether this separate patterning could influence the current flow in the sample and create the DW motion asymmetry. 2) In all the wires, we assumed that the DW is sitting perpendicular to the wire axis. This may not necessarily be true. The DW can be tilted or distorted in the wires (this situation will be explained in details in section IV.1.6). Thus, the angle between the current direction and the wires may not necessarily be the same as the angle between the current direction and the DW.

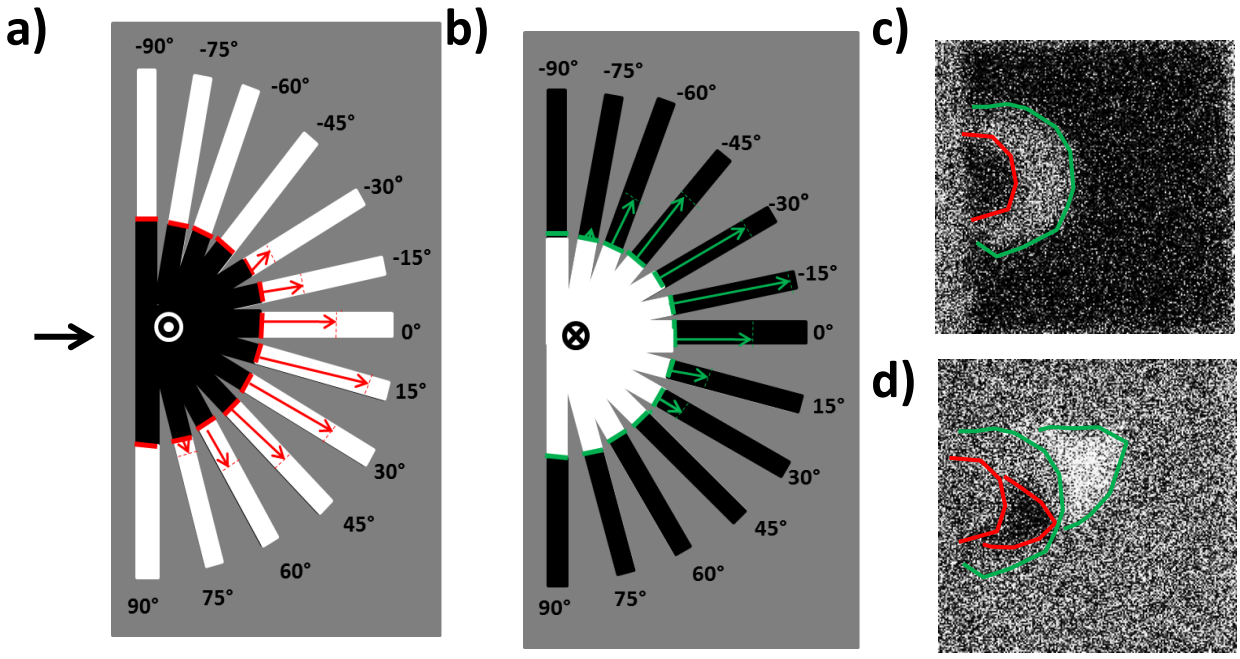

Figure IV.6. Schematic diagrams of the DW displacements in wires with angle -90° to 90° according to the mirror symmetry operation showed in figure IV.5 a) for up/down DW. b) for down/up DW. c) The MOKE images of the initial position of the DW in a magnetic pad. Two arc-shaped DWs (up/down DW in red and down/up DW in green) spanning from -90° to 90° were prepared. d) Differential image of the DW displacement under the current injection. The two DWs move asymmetrically and show opposite asymmetries with a maximum velocity along the angle ~ ±20°..

In order to exclude these two possible scenarios, I repeated this non-collinear current induced DW motion experiment in a continuous film. The sample is a 10µm X 10µm magnetic pad of Pt/Co/AlO_x. I nucleated two semi-circle shaped DWs in this pad (shown in figure IV.6.a). The advantage of this shape is that it spans all the angles from 90° to -90°. Then under the current injection, the DW motion was studied in the complete range of angles. We observed the asymmetric DW motion with opposite asymmetries for up/down and down/up DWs and a maximum DW displacement for angles ~ ±20° as in the case of the wires (figure IV.5).

Since we observed the same asymmetry for the samples with wires as well as for the continuous films, the artifacts associated with the sample fabrication and the DW tilt in the wires can be excluded. This confirms that variation of the DW displacement is due to the fact that the current is applied at different angles with respect to the DWs.

IV.1.5. Absence of the DW tilt

In a nanowire, in order to minimize its length and thus its energy, the DW is expected to sit perpendicular to the wire length. However, recently K.-S. Ryu *et al.*[5] showed that in perpendicular magnetized Co/Ni nanowires the DW tilts during their fast current induced motion (figure IV.7). They showed that the tilts are opposite for up/down and down/up DWs and that the tilt angle strongly depends on the length of the pulse (figure IV.7.b). For short pulses, the tilt angle is very small. It increases with the pulse length and saturates for pulse longer than around 100ns. Later, An explanation of this tilt formation was given by O. Boulle *et al.* [Boulle 2013] using analytical modeling and micromagnetic simulation

In our non-collinear experiments, the angle is defined between the current direction and the wire axis and the DW itself. We assume that the DW does not tilt so that the angles defined with respect to the wire axis and the DW are the same. However, if the DW tilts as described by the model in[6], this assumption is wrong. In our experiments, the width of the wire is around 500nm. Due to the resolution limitation of the microscope, we cannot observe directly if the DWs inside the wires are tilted or not. However, unlike the wire case, for the bubble domain case the DW motion can be directly observed for every angle. Since we observed the same asymmetric DW motion for the wire structure and the magnetic bubble, one could conclude that, with respect to the current direction, the angle with the wire axis and with the DW inside the wire are the same. i.e, there is no tilt formation occurs in the wires. The absence of DW tilt can be due to the fact that we used very short pulses. According to the results by O. Boulle *et al* for the 500nm wires that I used in my experiments, at least a pulse duration of 25 ns is needed to form a stable tiltIn my experiments, I used very short pulse length (~2 to 3 ns). This may explain the absence of the tilt formation in the wire.

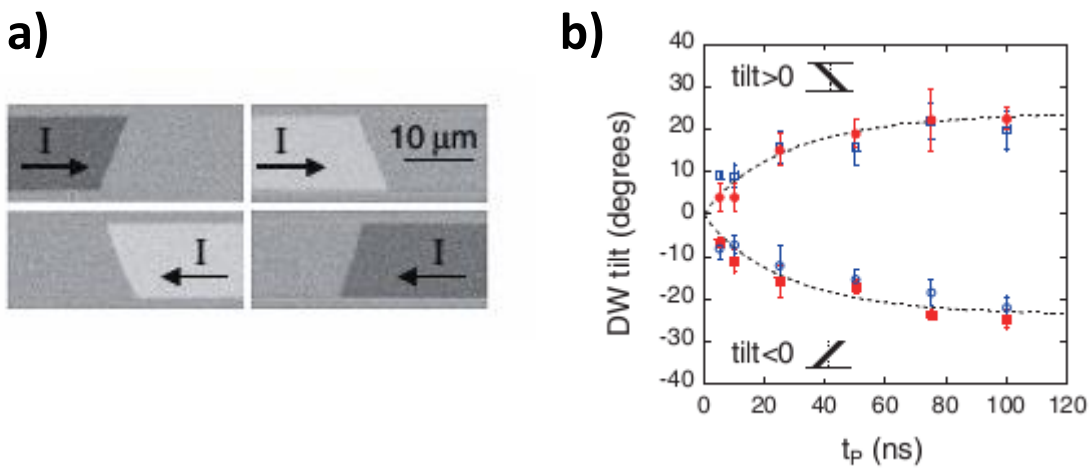

Figure IV.7. The observations K.S. Ryu *et al.*[5] a) The DW is tilted along the wire direction during its fast current induced motion. Black (white) color contrast corresponds to down (up) magnetic domains. For up/down and down/up DWs, the tilts are opposite. b) Variation of the DW tilt with respect to the pulse length of the injected current.

VI.1.6. Physical mechanism behind the non-collinear current induced DW motion

For the non-collinear geometry, a series of negative current pulses injected after an identical series of positive current pulses does not bring back the DW to its initial position (figure IV.3.b & c). If the DWs response to the current were linear, the total DW displacement(Δ) would vanish after injection of a positive and negative current since the total current is zero (Δ[+*I*]+ Δ[-*I*]= Δ[+*I*-*I*] =(Δ[0]=0]Thus, here the effect of current on the DW is non-linear. The DW displacement results from the SOT and the magnetization of the DW. SOT vary linearly with the current. If the current only created SOT without altering the DW structure, the DW displacement would be linear with the current. Since it is not the case, we can conclude that the current not only induces SOT, but also contributes to the DW motion by modifying the DW structure.

In our system, there are two possibilities for the modification of DW structure: 1) the tilt of the DW in the wires 2) the canting of the core magnetization of the DW (figure IV.8.a). In the previous section, I explained why the DW tilt in the wires can be excluded as a relevant source of the asymetry. The only remaining possibility of the non-linearity is the distortion of the core magnetization of the DW.

IV.1.6.1. Dynamic deformations of the magnetization

If a strong DMI exists in our system as demonstrated by recent experiments [Belmeguenai 2015] ,in the static configuration the DW possesses a perfect chiral Néel structure where the core DW magnetization is aligned with the current direction In the dynamic regime, this may not necessarily be true. The combined action of the current (STT that I will neglect in the following and strong SOT) and DMI can distort the magnetization direction and change its angle with respect to the current direction.

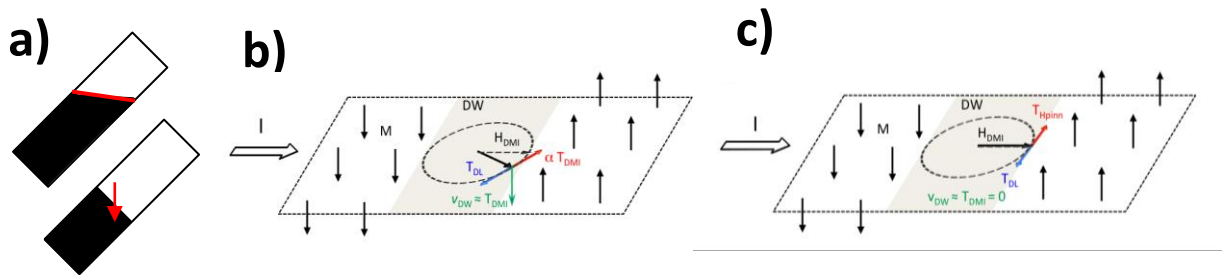

Figure IV.8. **a)** The two possibilities for the DW distortion: the tilt of the DW in the wires or the canting of the core DW magnetization. **b)** Schematic representation of the dynamic DW distortion in the SOT-DMI model. The orientation of the core DW magnetization (black arrow in the grey area), initially pointing along H_{DMI}, is modified by the presence of T_{DL}. As the DW equilibrium structure is distorted, the effective restoring field (H_{DMI} in this case) exerts a torque pointing out-of the plane. The perpendicular magnetization variation, that moves the DW, also produces a dissipative torque αT_{DMI}. In steady state motion the in-plane orientation of the DW magnetization is fixed by the balance of in-plane torques T_{DL} and αT_{DMI}. **c)** In the presence of forces that oppose the DW motion, such as pinning to defects, the effect of T_{DL} on the DW distortion is inhibited by the effective pinning torque, T_{Hpinn}. Since there is no DW distortion, there cannot be any out-of plane torque and thus the velocity must be zero**.**

The current induced DW motion within the SOT-DMI model can be depicted using a graphical construction, as shown in figure IV.8.b. When the current is applied through the DW, the damping-like SOT induces a distortion of the Néel DW structure. The restoring internal field (H_{DMI}) creates an out of plane torque that displaces the DW. The dissipative torque associated to the DW motion is opposed to T_{DL}. Since T_{DL} and the dissipative torque are directed opposite to each other, at a certain steady angle, they cancel each other.

$$T_{DL} = \alpha . T_{DMI}$$

and the out-of-plane torque dictates the DW velocity

$$v \propto T_{DMI}$$

Both T_{DMI} and T_{DL} depend on θ, the angle between the actual DW magnetization and its static equilibrium position dictated in this case by the DMI

$$T_{DMI} \propto H_{DMI} \sin(\theta) \qquad \text{and} \qquad T_{DL} \propto H_{DL} \cos(\theta)$$

Here H_{DMI} and H_{DL} are the corresponding effective fields. In this case, the deformation angle is:

$$\tan(\theta) = \frac{H_{DL}}{\alpha . H_{DMI}}$$

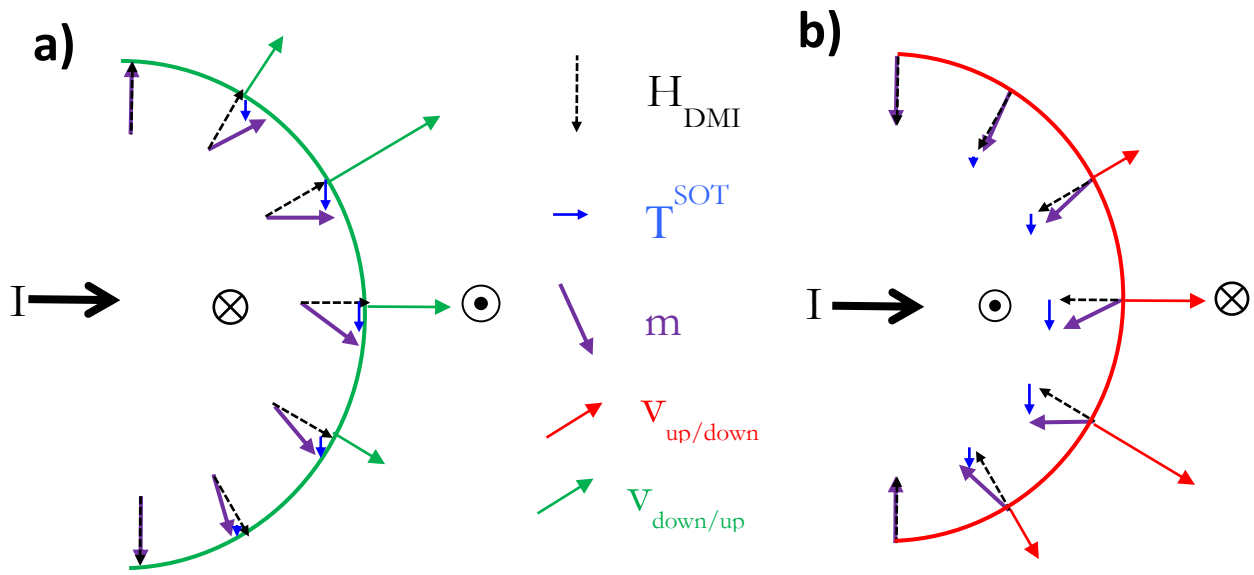

Figure IV.9: Schematic picture of the DW distortion across the bubble. **a)** Down/up DW case. **b)** Up/down DW case. Initially, the magnetizations are aligned along the DMI field (shown by the dotted black arrows). When the current is applied, the spin orbit torque cants the magnetization clockwise for a down/up DW (anti-clockwise for a up/down DW). The new direction of the magnetization is shown by the purple arrows. For a certain angle different from 0°, the magnetization gets aligned with the current and the resulting DW velocity (shown by red and green arrows) is maximum.

If we include the magnetization distortion into the bubble domain motion picture, the asymmetry of the DW velocity can be explained (figure IV.9). According to the DMI-SOT mechanism, the DW velocity is proportional to the component of the

magnetization aligned with the current When the DW is distorted, the core magnetization of the DW at the 0° position of the bubble deviates from its alignement with the current and its velocity is reduced. At the same time, because of the same distortion, the core magnetization of the DW at a tilt angle of the bubble can align along the current direction. Hence, the DW displacement at this particular angle becomes maximum (figure IV.9). Due to the chirality of the magnetization imposed by the DMI, the magnetization distortion is opposite (clockwise and anti-clockwise) for up/down and down/up DWs. Hence the two DWs shows opposite asymmetry.

IV.1.6.2. Asymmetric DW motion in creep regime

An important specificity of the SOT-DMI model is that the velocity depends on T_{DMI} (see figure IV.8) that depends on the dynamic canting angle: a significant DW distortion is synonym of large velocity while a slow DW motion is accompanied with a small distortion.

However when the injected current density is decreased to decrease the DW velocity, the DW motion regime changes. At the small current densities, the DW enters the creep regime. In this regime, the DW is sensitive to the imperfections or the defects in the material structure that act as local pinning centers. Although this regime is much more complicated, involving the displacement of an elastic interface in weakly disorder medium (see chapter I), it can be viewed here in a simpler way. The DW displacement involves the pinning and hopping between pinning centers. The DW spends the majority of the time at the pinning centers and moves very fast between the pinning centers. Therefore the average velocity is largely determined by the density of the pinning centers and their depinning time, where the short period of the DW motion between the pinning centers is negligible.

To a first approximation, the DW pinning acts as an effective field opposing the DW motion (figure IV.8.c).

If $H_{DL} \approx H_{pinn}$ the DW deformation becomes

$$\tan(\theta) = \frac{H_{DL} - H_{pinn}}{\alpha . H_{DMI}} \approx 0$$

At very small DW velocities the DW distortion should vanish. In the absence of this DW distortion, the maximum DW velocity should be along 0°, not at a finite angle.

In order to test the validity of the asymmetric DW motion mechanism presented above, I repeated the same experiment on the magnetic bubble domain for different, and particularly smaller current densities: $1.1x10^{12}$ Am^{-2}, $1.6x10^{12}$ Am^{-2} (case shown figure IV.6) and $2.1x10^{12}$ Am^{-2}.

For the smaller current density, the DW motion was slowed down approximately by three orders of magnitude compared to the two other current densities). The DW velocity was extremely small (~0.1m/s) and the DW dynamics is expected to be in creep regime. Interestingly, the asymmetric behavior of the DW motion remained the same (figure IV.9). Since the same asymmetric behavior is observed for both fast and very slow DW motion, the physical mechanism described above is not valid and the asymmetric motion has a different origin or needs a more complex model than the simple DMI-SOT mechanism.

To conclude, with the current understanding of the SOT driven DW motion in the presence of DMI, it is very hard to explain the asymmetric DW motion, apparently independent on the DW motion regime. More experiments are needed to get a better picture of the exact physical mechanisms behind the non-collinear current induced DW motion.

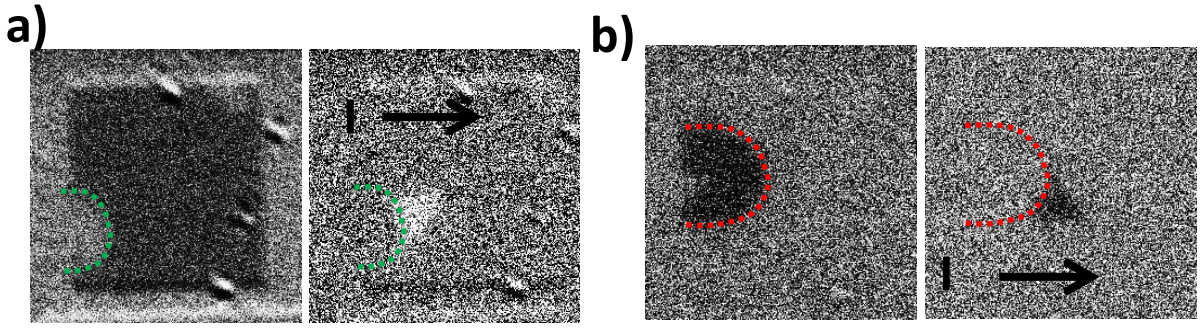

Figure IV.10. DW displacements in a magnetic pad at very low current density ($1.1x10^{12}$ Am^{-2}). **a)** For down/up DW. **b)** For up/down DW. The maximum DW velocity was very slow (0.1m/s), but the DW motion asymmetry was preserved, with a maximum velocity for an angle around 20°, identically to the fast domain wall motion regime.

IV.1.7. Angular dependence of the critical current

We have studied the critical current density for the DW motion in each wire. In our experiment, the critical current density is defined as the smallest current required observing the DW displacement over the resolution of the microscope (300 nm). Ideally, a continuous current should be used for this experiment. However, using such current increases the sample temperature. This may either lead to the nucleation of new domains or thermal breakdown of the sample. This is why, we have measured critical current density for 1000 pulses with three different durations (1.8ns, 3.8ns and 6.3ns) injected at 100 Hz frequency. The corresponding measurements are shown in figure IV.10. We observed that the critical current density mirrors the velocity dependence on the tilt angle of the wire. Again, this result excludes the possibility of the DW tilt formation in the wires: the pulses are short and DW does not move enough distance to form the DW tilt.

For each wire, the critical current densities decreased as the pulse length were increased. This is expected because the increase in the pulse length increases the thermal energy that eases the DW depinning.

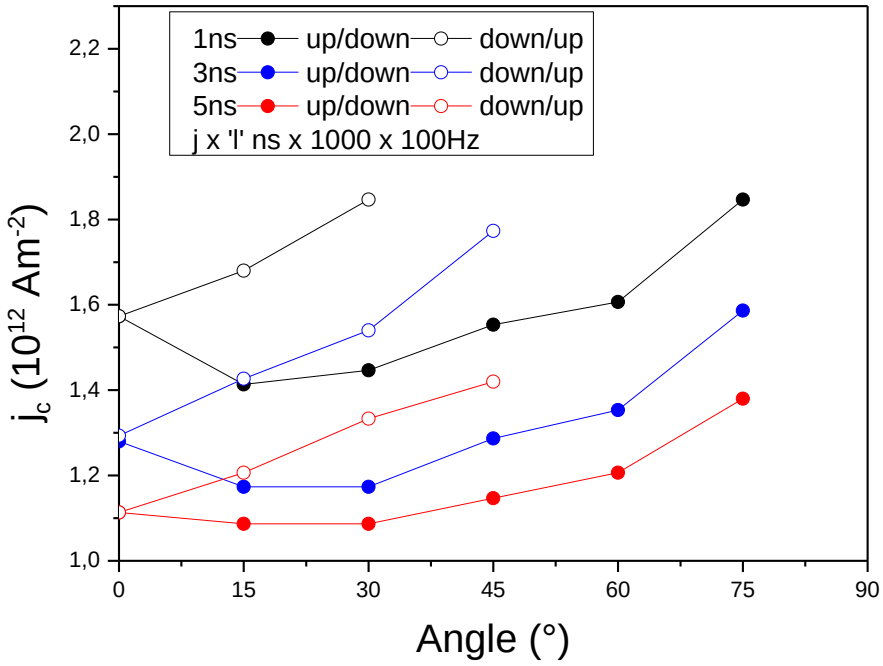

Figure IV.11. The critical current density v/s the tilt angle of the wire (ϕ) for +I (shown as closed symbols) and –I (shown as open symbols). The black, blue and red curves correspond to the current pulse lengths1.8ns, 3.8ns and 6.3ns respectively.

IV.2. Magnetic origami

IV.2.1.The basic concept

Origami is the art of paper folding where one can create different shapes from the same sheet of paper. In our studies, we implement the concept of the origami into magnetic devices. We introduce new magnetic switching schemes where the magnetization reversal depends on the geometry of the device. i.e., different shapes fabricated from the same magnetic thin film undergo different magnetization reversal schemes under the same current injection.

As the current technological world craves for faster and more efficient devices, magnetic devices like memories and logic devices should also be improved with better functionality and faster accessibility. Finding novel routes for storing, retrieving and transmitting the magnetic information is important for improving these magnetic devices. Information is written by switching the magnetization using either magnetic or electrical excitations. If one could introduce a simple additional parameter that harnesses the complexities of the magnetization reversal, new and better magnetic devices can be designed. This is what the concept of magnetic origami offers. In our experiments, we show that by simply changing the geometry of the device, a large versatility for the magnetic device functions can be achieved.

The idea of the geometrical switching is constructed based on the specific features of the non-collinear current induced DW motion that I described in the last section. Even though the exact physical mechanism behind this effect is not completely clear, the specific characteristics of the DW motion are useful for practical applications. While in the collinear geometry, upon current injection, DWs move equally in the wires irrespective to their polarity, in the non-collinear geometry, the DW motion depends on the current direction as well as on the DW type (up/down or down/up). An important feature of the non-collinear DW motion is that in the wires with angles $\geq 45°$, only one polarity of DW moves while the other stands still: the up/down DW moves in the wire with +45° angle with respect to the current direction while the down/up DW moves for the wire with -45° angle. This offers a unique possibility of DW selectivity and, from an application point of view, opens up the possibility of new devices. The beauty of this idea lies in the simplicity of its implementation; it requires only changing the shape of device

Exploiting the property of the DW selectivity, we have developed new devices whose magnetization switching is determined by their geometry. We experimentally demonstrated two geometries with different kinds of switching schemes: ‘u shaped’ reversible and ‘s

shaped' irreversible switching. A detailed description of the device construction, switching mechanism and experimental results will be given in the following sections.

IV.2.2. The building blocks

The geometries for the reversible and irreversible switches were constructed by joining three wires of angle 0°, ±45°. The wires with angle 0° can transmit both up/down and down/up DWs. The ±45° wires select the DW polarity so that it determines the polarity of the magnetization switching (figure IV.12). In our device the switching occurs through domain nucleation followed by the DW motion. If the magnetization is initially saturated, we need first to nucleate a domain to induce the switching. This nucleation can be induced by joule heating due to the injection of relatively high current density pulses. Since the ±45° wires determine the switching polarity, the domain should be nucleated in these wires and not in the 0° wire (the nucleation is discussed in details in section IV.2.6). To control this nucleation, this, we make one end of the ±45° wires much narrower than the other (figure IV.12.c). Since the magnetic volume is smaller in the narrower regions, its thermal stability is less compared to the wider region. Therefore the nucleation can be achieved in the narrow parts of the ±45° wires for relatively smaller current compared to that needed for nucleating a domain in the 0° wire.

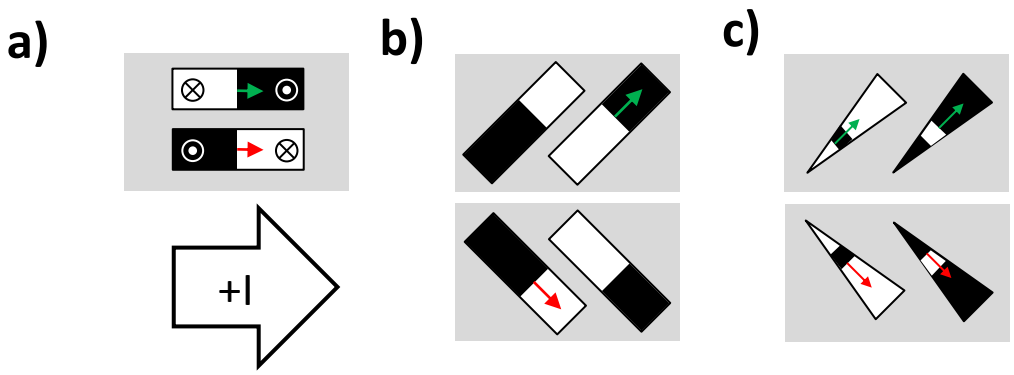

Figure IV.12. The basic building blocks for the construction of the shape based switches. **a)** The 0° wires: here under current injection, both up/down and down/up DWs move. Thus, the wire can be used as a DW transmitter. **b)** In the 45° wire, only one of the DW moves. Hence, it can be used as DW selector. **c)** The tilted wires define the direction of the magnetization switching by selecting the DW polarity to be injected. In order to inject the DW, we need first to nucleate a domain. The nucleation can be controlled by giving pin shapes to one end of the tilted wires.

In the ±45° wires, the nucleated domains expand or contract depending on their magnetization direction. In +45° wires the up/down domain wall moves, while the down/up DW does not. If the nucleated domain is oriented upwards, it expands along the wire. On the other hand, if the nucleated domain is oriented downwards, the mobile up/down DW moves

and meets the immobile down/up DW resulting in the collapse of the magnetic domain (figure IV.13.c). Opposite domain expansion occurs in -45° wire.

By joining these three wires to form specific two dimensional geometries, reversible and irreversible magnetic switching devices can be designed.

IV.2.3. The u-shape device: a reversible switch

By joining two tilted wires with opposite tilt angles at the two ends of a straight wire a bipolar switch can be built. We call this device a 'u-shape switch' because the device shapes like the letter 'u'. In a functional device, the read element, such as the top part of a magnetic tunnel junction, is placed on top of the straight wire (0° wire).

The switching mechanism of the u-shape and inverted u-shape devices is shown in figure IV.13. Here the DW motions under positive and negative current injection for the two different initial saturation (up or down) states are shown. The magnetization reversal direction is defined by two parameters: the device shape and the current direction.

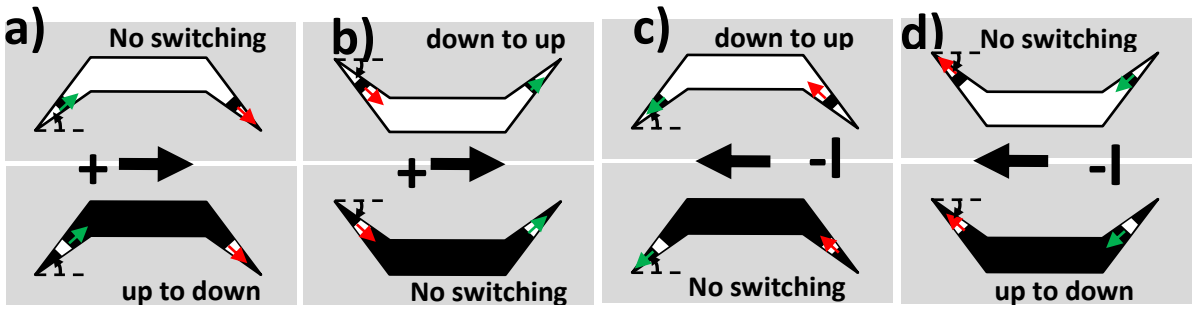

Figure IV.13. Schematics of the DW motion during switching. The black and white colors correspond to up and down magnetization states respectively. **a)** Switching of inverted u-shape under a positive current injection. The DW moves from left to right along the current direction. If the device is initially saturated down, an up magnetic domain gets nucleated at the end of the tilted wires. In the nucleated domain, the fast moving down/up DW sits behind the immobile up/down DW. Hence, the nucleated domain diminishes and no DW is propagated through the straight wire. On the other hand, if the saturation is initially up, the down nucleated domain on the left wire expands to the straight wire resulting in the switching to the down magnetization. **b)** Switching for u-shape device under the injection of a positive current. **c)** Switching of inverted u-shape **d)** and u-shape, under the injection of a negative current.

The magnetization of the inverted u-shape device submitted to a positive current injection (figure IV.13.a) switches only into the down direction. If the initial saturation state is already downward, no switching occurs. This is because under positive current, the DW propagates from left to right. The relevant domain is then nucleated in the narrow part of the left wire (-45° wire). In this -45° wire, the down/up DW moves while the up/down DW stays

still. This results in the expansion of the down magnetic domain and the contraction of the up magnetic domain. Thus if the initial magnetic state is upwards, under a current injection, a down magnetic domain gets nucleated in the left wire and then it expands through the straight wire.. If the initial state is already downwards the magnetic state of the straight wire is not altered. Now to switch from the down to the up direction, the current should be applied in the opposite direction (figure IV.13.c). This is because under negative current injection, it is the domain nucleation and the DW propagation in the right wire (45° wire) that defines the switching. In this 45° wire the up/down DW moves while the down/up/ DW stays still. Since magnetization reversal in opposite directions can be achieved by applying current in opposite direction, the device is a bipolar switch.

The u-shape and the inverted u-shape are mirror images. According to the mirror symmetry operations, for the same current direction, the switching behaviors of the two devices are opposite to each other as represented in figure IV.13..

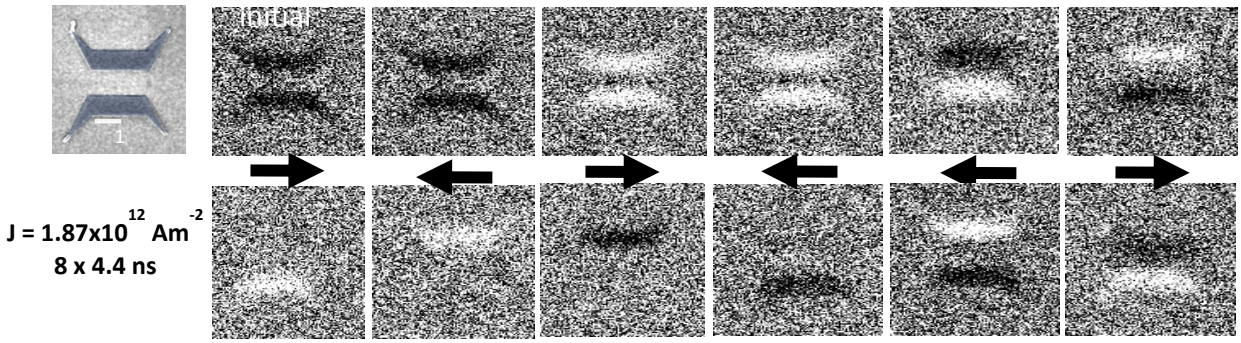

Figure IV.14: MOKE microscopy images of the switching events in u-shape and inverted u-shape devices under the injection of a series of 8 current pulses (whose direction is shown by the black arrows) of 4.4ns length with a current density = 1.87×10^{12} Am^{-2}. The first raw shows the initial state of the devices and the second raw contains the differential images of the switching events after applying the current. Different initial saturation states were studied: both u-shape and inverted u-shape saturated upwards, downwards, or a mixed state of the two saturations. In all the events, the switching occurs according to the mechanism described previously (figure IV.14). The u-shape and inverted u-shape devices always behave opposite to each other.

In order to check experimentally if the switching in the u-shape and inverted u-shape occurs according to this mechanism, the two devices were fabricated from the same $Pt/Co/AlO_x$ thin film (the fabrication process is detailed in chapter II). The final device consists in u-shape and inverted u-shape Co/AlOx structures on top of a Pt electrode. The length and width of the central region were 2µm and 500 nm respectively. The switching was imaged using MOKE microscopy. The two devices were fabricated adjacent to each other on the same Pt electrode so that they can be imaged simultaneously under the same current

injection. The different switching events under different conditions (positive and negative current, initial saturation up or down, are shown in figure IV.14. The switching images confirm that the two devices are bipolar switches with opposite switching behaviors under the same current injection as explained before (figure IV.13)

IV.2.4. The s-shape device: an irreversible switch

In the u-shape devices, even though the magnetization reversal is controlled by the geometry of the device, it still depends on the current direction. Using the same idea, we can build objects whose switching is completely independent of the current direction and purely defined by the shape. In the u-shaped device, the two wires with opposite tilt angle were connected to the straight wire. In the new 's'-shaped device, the two pin wires have the same tilt angle. The detailed schematics of the DW motion are shown in figure IV.16. Whatever the direction of the current, positive or negative, both right and left pin wires select the same DW, resulting in the straight wire always magnetized in the same direction. This direction is only determined by the tilt angle (+45° or -45°) of the wire.

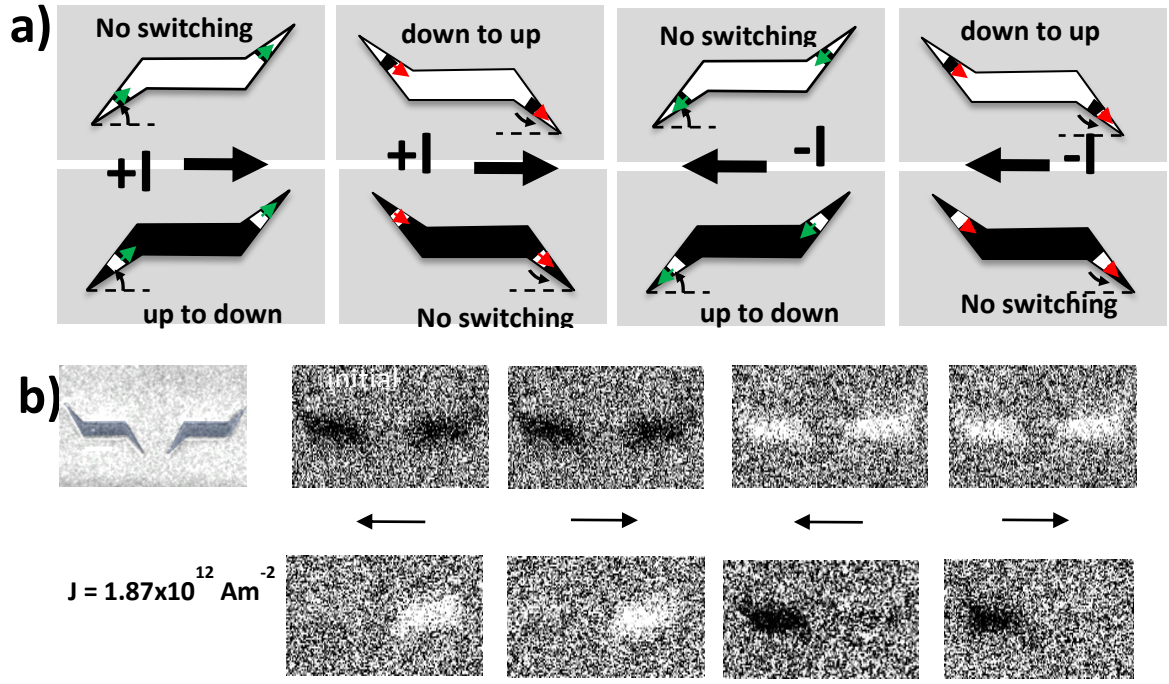

Figure IV.15. **a)** Schematics of the switching events in s-shaped devices. Since the two pin wires have the same tilt angle, they select the same DW to be propagated into the straight wire under both positive and negative current injection. Hence the final magnetization state of the device always remains the same (either up or down). The switching polarity depends on the sign of the tilt angle. **b)** MOKE images confirming the switching schemes as explained in figure a. Here a series of 8 current pulses of 5ns length with a current density = $1.87 \times 10^{12} Am^{-2}$ were applied. Under the current injection, a device always ends up in the same magnetization state. i.e, the switching is irreversible

Figure IV.15.b shows the MOKE images of the magnetization switching in the s-shaped devices. After the current injection, the magnetization state of the particular device always remains in the same direction, i.e. the switching in these devices is irreversible.

From applications perspectives, such irreversible switches can be used as reference bits where the magnetization state always remains in the same direction irrespective of the current direction.

IV.2.5. Imaging of DW motion during switching

In the previous parts, only the result of the switching process was imaged (figures IV.14 and IV.15). In order to confirm that the switching follows the nucleation/propagation mechanism that is at the basis of our Origami concept, images during the switching process are required. Real time imaging is far from the temporal resolution and sensitivity of the MOKE technique we used. However, the complete switching was obtained after the injection of 8 consecutives current pulses and images can be obtained after a given series of these pulses to follow the switching mechanism. More precisely these 8 current pulses were divided into 4 series of 2 pulses and a differential image was taken after each series. The corresponding images are shown in figures IV.16 and IV.17. Initially, the magnetization of the devices was saturated by applying a magnetic field.

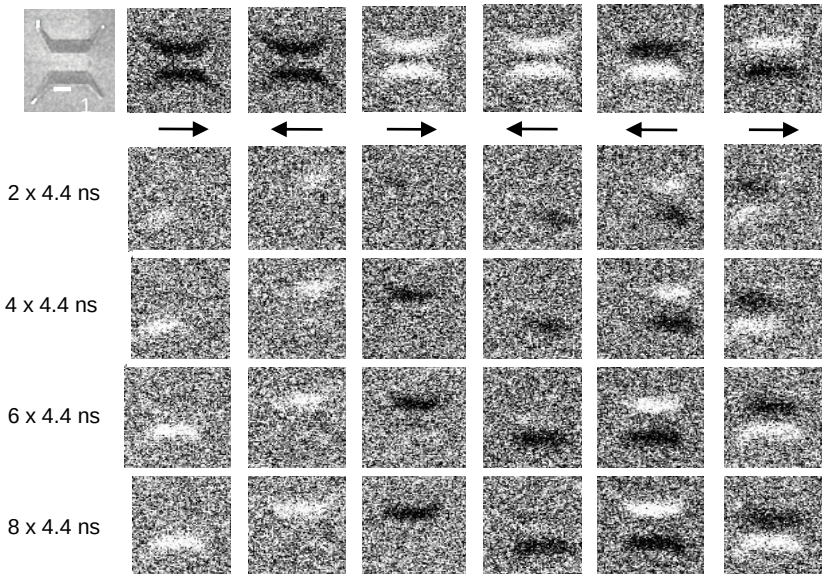

Figure IV.16: Step by step imaging of the DW motion during the switching for a u-shape device and an inverted u-shape device. The pulses used were 4.4ns long. The first raw contains the images of the initial magnetic states of the switches. The black arrows show the direction of the current. The further consecutive images in each column correspond to the step-by-step DW motion after applying a series of 2 current pulses at each step. These images confirm that the switching occurs according to the nucleation and DW propagation mechanism explained in the text

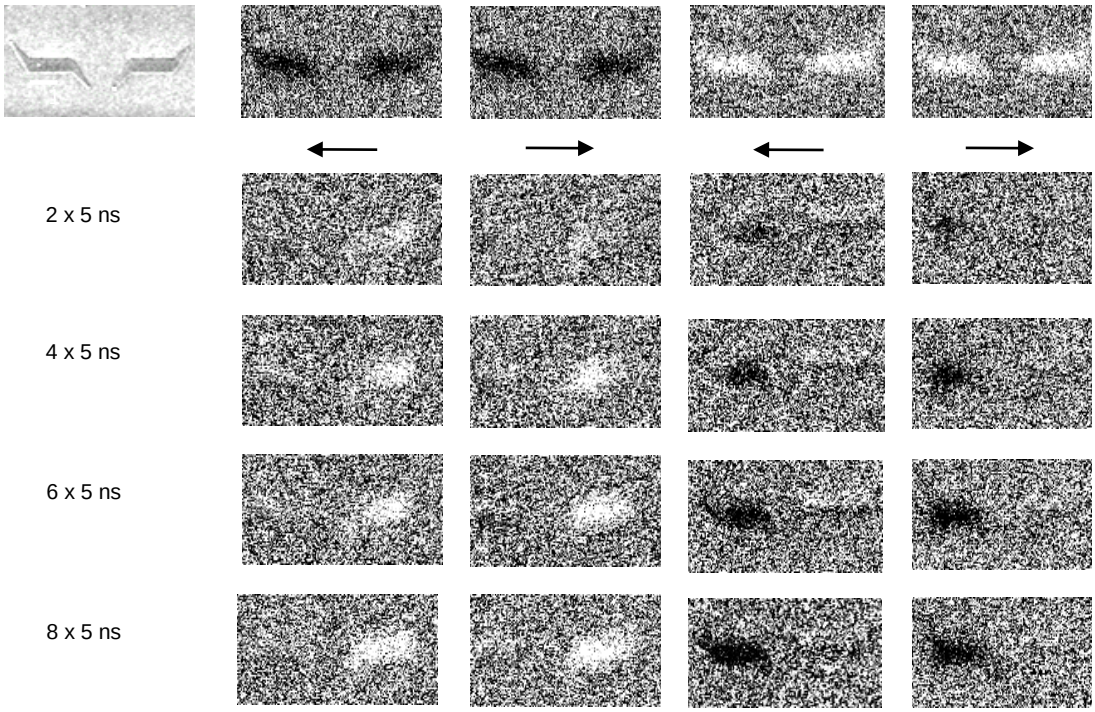

Figure IV.17: Step by step imaging of the DW motion during the switching for s-shape devices. The length of the current pulse used here was 4.4ns.

IV.2.6. Switching: size, speed and nucleation limits

The switching scheme that we propose is based on heat induced domain nucleation and selective DW propagation. The speed of the switching depends on the total length of the device as well as on the DW velocity. The smaller the size of the bit length and larger the DW velocity, the faster will be the switching. Due to the resolution limit of the optical microscope, we chose the 2 µm length for all the straight wires in all the devices. Ideally it should be possible to make switches with the smaller size that work using exactly the same principle as long as their length remains larger than the DW width. A second way of improving the switching time is to increase the DW velocity. The maximum DW velocity reported in Pt/Co/AlOx was around 400 m/s. In our experiments, the maximum DW velocity achieved was around 100 m/s. This is because the sample resistance limited the maximum current density that we could apply. By using devices with less resistance, it can be possible to improve the DW velocity and thus the switching speed.

The range of pulse width and height where controlled switching occurs is limited by domain nucleation. As discussed earlier, the shape of the switch contains two tilted wires and a straight wire. The switching is only possible if the nucleation takes place in the tilted wires and not in the straight wire. For this, the tilted wires have a pin shape in order to decrease the thermal stability in the narrower regions. Thus the current required to nucleate the DW in the tilted wires is always smaller than that in the straight wire. At the upper limit, when the current becomes large enough to create nucleation in the straight wire, the switching becomes stochastic.

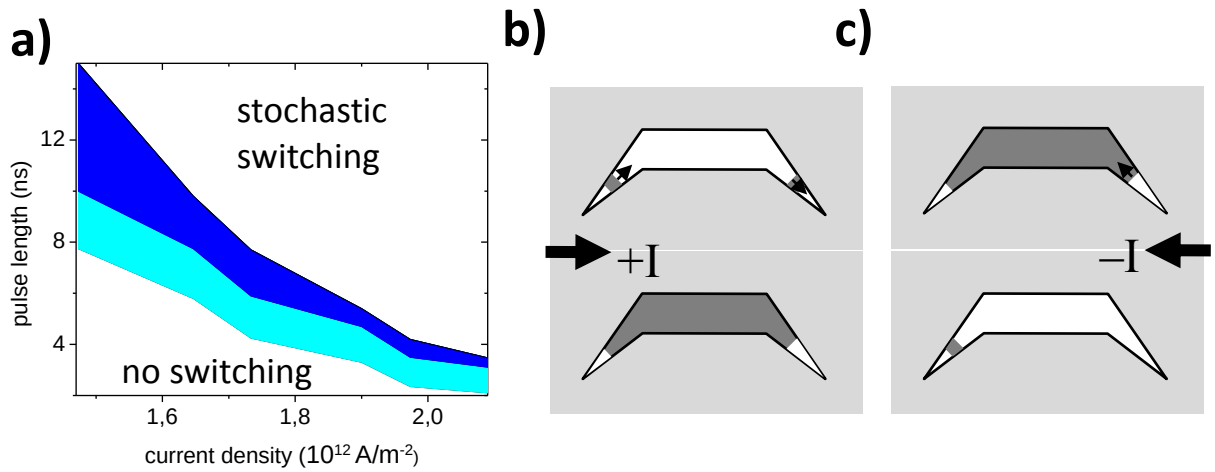

Figure IV.18. The current density required for the switching **a)** Graph showing the pulse length required for switching with respect to the current density. The dark and light blue regions correspond to the saturated and non-saturated initial states of the switches. Note that the switching pulse length window becomes narrow as the current density increases. This is because for large current density, a small change in the pulse length produces a large variation in Joule heating and nucleation becomes easier. **b)** A schematic diagram of switching from a saturated state. The reversal begins with a nucleation (upper panel) followed by DW propagation through the straight wire and into the second tilted wire, where it stops (lower panel). **c)** Since a DW is already present, the high current density required for nucleation is not required any more. Therefore, the object can be switched back with lower current density. This phenomenon increases the switching range (light blue area in panel a).

The critical current density required for switching depends on the initial magnetic state of the switches. For all the switching experiments that we discussed so far, magnetization was initially saturated using an external magnetic field. But there is also another possible initial state where DW is already present in the tilted wires. In this case no nucleation is required for switching. One such possible situation is schematically shown in figure IV.18b&c. To switch our device, we apply a current such that the nucleated DW in one tilted wire propagates through the straight wire and reaches the second tilted wire. Here, because of the opposite tilt, the DW will stop. Now if we want to do a second switching to the opposite direction, since there is already a DW present in the tilted wire, there is no need of nucleation. Instead we

only need to apply current to propagate the DW in opposite direction. Since the current required for propagation is smaller than that for the nucleation, the critical switching current becomes smaller. Note that the possibility to have DWs that remain in the pins depends on the relative magnitude of two effects. The retaining force is given by the strength of the pining to defects. The expelling force is derived from the DW energy reduction corresponding to the shortening of the DW as it moves toward the end of the triangle. To obtain saturation of the tilted wires they could be shortened, thereby increasing the pin angle and the resulting expelling force. We chose to work with long tilted wires such that the DWs do not move out by themselves, since we can easily saturate the samples using external field.

In order to evidence these different types of behavior, we systematically studied the switching as a function of the length and the intensity of the current pulses. The result shown in figure IV.18.a indicates the existence of three different regions: no switching, switching and nucleation regions. For a particular current density, an increase in the length of the current pulse increases the Joule heating. For short pulses, there is not enough heat for the nucleation and thus no switching. When we increase the pulse length, the heating becomes sufficient to nucleate in the tilted wires and the switching begins. The upper limit is given by the pulse length where nucleation occurs in the straight wire. Above, the switching becomes stochastic.

The critical current dependence on the initial state is also illustrated in Figure IV.18.a where the switching region is further divided into two. The dark and light blue region corresponds to the switching window for saturated and non-saturated initial states.

IV.2.7. The advantages and the future of magnetic origami

The current induced DW motion has been a well-known phenomenon for many years. Until now, for the application requirements, it has been studied in one-dimensional systems like nanowires. Here through our new studies, we could introduce the current induced DW motion into a new dimension. We prove that by understanding the current induced DW dynamics in different 2D geometries, new and interesting device concepts can be developed.

The physical phenomenon that led to the realization of this new concept is the asymmetric characteristics of the DW motion in the non-collinear geometry. Here, one could vary the relative motion of the two domain walls depending on their polarity and the degree of the non-collinearity. Such freedom is not possible in the conventional collinear geometry. We infer that this new liberty to control the current induced DW motion opens a wide range of applicability for the DW based devices.

The ‘u-shape’ and the ‘s-shape’ devices explained previously are merely two examples of what can be achieved by the geometry control. In Pt/Co/AlOx material itself, it

will be possible to make numerous shapes and achieve different magnetization reversal schemes. At the same time this new concept can be extended into different magnetic multilayer systems. The SOT based DW motion and switching experiments have been widely studied in many magnetic multilayer systems. Our new experiments can be done in all these systems. Since the spin orbit interactions are different in different systems, the asymmetric non-collinear DW motion is expected to be material dependent. Then according to the DW dynamic properties, each system requires its own device geometries. For this reason, the geometrical switching offers countless strategies to develop different magnetic devices.

Compared to the STT switching, the SOT switching holds the advantage of the better endurance. In the case of STT based switching, the writing current should be applied across the magnetic tunnel junctions (MTJs). For the SOT switching, the current is applied in-plane through the heavy metal and not through the MTJ. Since the MTJs are very sensitive to the current induced electrical and thermal breakdown, the SOT based devices present a much better endurance. On the other hand, compared to the STT switching where only current is used, the SOT switching requires an additional small in-plane field to decide the magnetization reversal direction[Miron 2011], i.e. the SOT switching is not a purely current induced phenomenon. Our new geometrical switching holds the same properties of the conventional SOT switching and, additional to this, it presents the advantage that the switching does not require any in-plane field. Here, the magnetization reversal direction is dictated by the geometry, not the in-plane field. Hence the switching is a purely current induced phenomenon.

Moreover, the non-collinear current induced DW motion enlightens new insights to the understanding of the physics behind the SOT driven DW motion. As discussed in section IV.1.5.2, the asymmetric DW motion can be due to a more complex phenomenon than simple SOT+DMI mechanism. For more understanding, the non-collinear DW motion of experiments can be extended to different multilayer systems. This will be the future perspective of this study.

To summarize, from both the application and the physics point of view, our new concept open new and interesting research possibilities to the current and future spin orbitronics research field.

IV.3. Conclusion

In this chapter, I described my experimental studies on current induced DW dynamics in Pt/Co/AlOx multilayer systems. I have studied the DW motion under non-collinear current injection. I observe that the current induced DW motion is asymmetric in the two dimensional geometries and that this asymmetry seems to be independent on the motion regime. It remains the same in the flow and the creep regime whereas the velocity is changed by three orders of magnitude. This observation points the limitations of the standard SOT/DMI model to explain my observation. Either an "ingredient" is missing or the model needs to be refined. The discovery of this asymmetric DW motion opens a broad field of application that we named as magnetic origami. Using this concept, we have shown that it is possible to build magnetic devices whose operations depend on the geometry of the magnetic device. I have developed two kinds of geometrical switches: reversible (bipolar) and irreversible (unipolar). Unlike the conventional SOT case, our new switching schemes are purely current induced phenomenon without any in-plane field required. Since this method uses the angular momentum by in-plane current injection, it can be used with wide range of materials from heavy metals to topological insulators. The major advantage is the ease to implementation: making shape is easily achievable in the lithography process. In CMOS technology, it provides a large versatility to the microchip design: cells with different shapes having different functions can be fabricated on a same chip with a single technological process.

To conclude, we introduce an interesting idea that is capable of extending the capacity of the usage of spin orbit torques into more exciting technological applications.

General conclusion

The role of structural inversion asymmetry (SIA) in different magnetic phenomena is currently one of the hottest research topics in nanomagnetism. Recently, along with the SIA, the influence of the spin orbit interaction in magnetic DW dynamics is widely studied. During my Ph.D, I have performed different experiments on this timely topic. I have studied two kinds of multilayers: Pt/Co/Pt and Pt/Co/AlO_x. Both of them are perpendicular magnetic anisotropic systems. The DW motion was detected using MOKE microscopy magnetic imaging technique

Pt/Co/Pt multilayers are almost symmetric. In this system, a weak SIA can be produced by the crystallographic differences between the top and bottom Co interfaces and by the different Pt thicknesses.

The DWs can be moved either by electrical current or magnetic field. I started my experiments with the qualitative study of the current induced DW motion $Pt_{(30Å)}/Co_{(6Å)}/Pt_{(15.6Å)}$ nanowires. Two kinds of torque mechanisms can be responsible for the current induced DW dynamics: spin transfer torque (STT) and spin orbit torques (SOT). For the STT case, the direction of the DW motion should be against the current flow. In our Pt/Co/Pt sample, the DW moved in the same direction of the injected current. Therefore, we concluded that STT does not play a role here.

Recently, it was predicted that the combined action of the damping like component of the SOT (T_{DL}) and Dzyaloshinskii Moriya interaction (DMI) can drive the DW motion either in the same or opposite direction of the current flow. In multilayers with SIA, DMI imposes chiral Néel DW structure. Depending on the material properties and multilayer composition, the DWs can have either left handed or right handed chirality. Similarly, the T_{DL} can be either positive or negative. By observing the DW motion direction and measuring the sign of the T_{DL}, the DW chirality can be identified. For this, we measured the sign of the T_{DL} by studying the current induced DW motion in the presence of an in-plane magnetic field. From this measurement, we concluded that in our system the DMI should induce the left handed Néel DWs.

In literature, other indirect methods were proposed to identify the DW chirality. Another technique is the field induced asymmetric domain expansion method. It was shown that, in Pt/Co/Pt, the out of plane field induced (H_z) domain expands asymmetrically in the presence of an in-plane field (H_{ip}). Using this method, both the sign and the strength of the DMI exchange field in DW were measured. We also reproduced the same measurements and we found that according the DMI model, the DW should have the right handed chiral Néel structure. This contradicts to what measured from the current induced DW motion. Therefore,

we decided to perform a detailed quantitative study of the asymmetric DW motion. After verifying the validity of the DMI model, we also searched for other possible physical mechanisms that could give rise to the asymmetry. We performed two kinds of experiments. At first we measured the DW velocity variations with respect to the H_{ip} at a constant H_z. Secondly, we studied the DW motion at varying the H_z and constant H_{ip}.

In the first experiment, we extract the anti-symmetric component of the DW motion from the DW velocities (V). We found that the saturation of the asymmetry indicating the saturation of the DW magnetization along H_{ip}, coincides with a change of slope of the raw velocity for both DWs. This proves that both DWs saturate at the same field value, thus ruling out the existence of the DMI induced chiral Néel wall in these samples. When repeating the experiment with different samples of $Pt_{(30Å)}/Co_{(6Å)}/Pt_{tÅ}$ with varying upper Pt layer thickness (x) we observe that they all exhibit similar features.

The field induced DW motion is mathematically described by Landau–Lifshitz–Gilbert (LLG) equation that contains two terms: An energy term (related to the effective fields) and a dissipative term (related to the damping). DMI influences the DW motion by contributing an additional effective field ($\pm H_{DMI}$) that modulates the energy term. We realized that there is another possible situation where the DW motion can be affected by the damping. i.e., the different damping experienced by the two DWs can result in asymmetric DW motion. We decided to perform a new experiment to differentiate between these two possible scenarios. The DW velocity is now measured as a function Hz under a constant $H_{ip.}$ Based on the creep scaling law, we can separate the energy terms influencing the DW motion from the slope of the linear plot ln (V) vs $H_z^{-1/4}$. We found that the DW velocities for the two different chiralities have the same slope indicating that their energies are same. They differ by an offset linked to $V_{0,}$ the creep velocity factor. V_0 depends on both energy and damping. Since the energies of the DWs are the same, we conclude that the difference in the intercepts that causes the difference in the two DW velocities is due to the difference in damping. We confirmed this possibility using the simulation and numerical modeling which reproduced the experimental results.

We propose the idea of the chiral damping by including an additional damping term (α) in the LLG equation. This additional damping is chiral in the sense that it depends on the type of DW (Up/Down or Down/up) and orientation of its core magnetization with respect to the magnetization gradient: $\alpha \propto \alpha_c\ (\vec{m}_{ip}.\nabla \vec{m}_z)$.

Chiral damping is the dissipative counterpart of the DMI. Therefore, just like DMI, it can play an important role in the magnetization dynamics in different magnetic textures. However, more theoretical work is needed to understand the physical origin of chiral damping. This is one of the future perspective of this study. Measuring the contribution of the

chiral dmping in different magnetic system may bring more insights for the understanding of the DW dynamics in systems with SIA.

Finally, the asymmetric bubble expansion in Pt/Co/AlO_x and Pt/Co/Pt were compared. We found that, at constant H_{ip}, increasing the H_z results in the disappearance of the asymmetry in Pt/Co/Pt. On the other hand, in Pt/Co/AlO_x it survived at large H_z fields. We attribute this to the presence of Walker breakdown in Pt/Co/Pt at low H_z field, but not in Pt/Co/AlO_x. We propose to use the asymmetric bubble expansion as a tool to differentiate between the steady and oscillatory regimes of the DW motion in materials with SIA.

In the second part of my Ph.D, I have studied the non-collinear current induced DW motion in Pt/Co/AlO_x. This study led to the realization of new magnetic device concept: magnetic origami.

In Pt/Co/AlO_x nanowires the measured current induced DW motion is extremely efficient. The current induced DW motion measurements were done by injecting the current collinear to the wire, and to the direction of the DW motion. In our experiments, we performed experiments in an unconventional geometry where the current is injected at different angles with respect to the DW. For this purpose we fabricated ferromagnetic (Co) wires of different tilt angles above the Pt under layer. This allowed the study of the DW velocity dependence on the the tilt angle. To avoid possible artifacts due the nanofabrication, the same kind of experiments were repeated in a larger non-patterned magnetic pad where a circular DW spans all angles. We observed the same kind of behavior in both cases: the DW moves asymmetrically as the wires are tilted left or right with respect to the electric current. For up/down and down/up DWs, the opposite asymmetries were observed.

When analyzing our results using the DMI+T_{DL} mechanism of the current induced DW motion, we found that this mechanism may explain the DW motion asymmetry in flow regime, but fails to explain it for thermally activated motion. Therefore, the non-collinear DW motion characteristics require at least a more complex mechanism than the simple DMI+T_{DL} model. This could be the future perspectives of this study.

Even though the physical mechanism behind the asymmetric DW motion is not completely clear, such behavior is highly useful for application. We found that above the tilt angle $\geq 45°$, only one DW polarity can move. This phenomenon can be used to select the DW polarity. Based on this, we constructed new magnetization switches where the magnetization reversal depends on the geometry of the device. Experimentally, we showed two different geometries (u shape and s shape) giving two kinds of magnetization reversals: reversible and irreversible. The same idea is applicable for different geometries and different materials. In short, we put forward a simple but fruitful concept with a wide range of applicability in magnetic memories.

To summarize, during my Ph.D., I have studied the DW motion in magnetic multilayers with different SIA. My results contribute to the understanding of the physical mechanism underlying the DW dynamics in these materials. I also introduced a new device concept offering an easy way of engineering the propoerties of spintronics devices.

References

Chapter I

[Ando 2008] Ando, K. *et al.* "Electric Manipulation of Spin Relaxation Using the Spin Hall Effect". *Physical Review Letters.*101, 036601 (2008).'

[Berger 1970] Berger, L. "Side-Jump Mechanism for the Hall Effect of Ferromagnets". *Physical Review B* 2, 4559–4566 (1970).

[Berger 1974] Berger, L. "Prediction of a domain-drag effect in uniaxial, noncompensated ferromagnetic metals", Journal of Physics and Chemistry of Solids, 35, 947 (1974).

[Buschow 2003] Buschow, K. H. J. *et al* "Physics of magnetism and magnetic materials" ISBN 0306474212, 9780306474217 Springer, 2003

[Chauve 2000] Chauve, P *et al*., **"**Creep and depinning in disordered media", *Physical Review B* 62, 6241 (2000).

[Chen 2013] Chen, G. *et al.*, "Tailoring the chirality of magnetic domain walls by interface engineering". *Nature communications*, 4. 2671 (2013)

[Dresselhaus 1955] Dresselhaus, G. "Spin orbit coupling effects in zinc blende structures". *Physical Review* 100, 580-586 (1955)

[Dyakonov 1971] Dyakonov, M. I et al., "Possibility of orienting electron spins with current". *JETP Letters.* 13, 467–470 (1971). Dyakonov, M. I. et al., "Current-induced spin orientation of electrons in semiconductors". *Physics Letters A* 35, 459 (1971).

[Dzyaloshinskii] Dzyaloshinskii, I. E., "Thermodynamic Theory of "Weak" Ferromagnetism In Antiferromagnetic Substances" *Soviet Physics JETP* 5, 1259 (1957) "Theory of Helicoidal structures in Antiferromagnetis I Nonmetals" Soviet Physics JETP 19, 960 (1964) . "Theory of Helicoidal structures in Antiferromagnetis II Nonmetals", Soviet Physics JETP 20, 665 (1965).

[Emori 2013] Emori, S. *et al*, "Current-driven dynamics of chiral ferromagnetic domain walls". *Nature materials*, *12*(7), 611-616 (2013).

[Engel 2007] Engel, H.A., *et al* "Out-of-Plane Spin Polarization from In-Plane Electric

and Magnetic Fields". *Physical Review Letters* 98, 036602 (2007).

[Fert 2013] Fert, A. *et al*., "Skyrmions on the track Nature Nanotechnology" 8,152–156(2013)

[Fert] Fert, A. *et al*., *Physical Review Letter* 44, "Role of Anisotropic Exchange Interactions in Determining the Properties of Spin-Glasses"1538 (1980). A. Fert, "Magnetic and Transport Properties of Metallic Multilayers", *Materials Science Forum* 59-60, 439 (1990).

[Freimuth 2013] Freimuth, F. *et al,* "Spin-orbit torques in Co/Pt(111) and Mn/W(001) magnetic bilayers from first principles". *Physical Review B* 90.17 (2014)

[Garate 2009] Garate, I. *et al.,* "Nonadiabatic spin-transfer torque in realmaterials". *Physical Review B* 79, 104416 (2009).

[Garate 2010] Garate, I. *et al*, "Inverse Spin-Galvanic Effect in the Interface between a Topological Insulator and a Ferromagnet" *Physical Review Letters* 104, 146802

[Garello 2013] Garello, K. *et al.* "Symmetry and magnitude of spin-orbit torques in ferromagnetic heterostructures". *Nature Nanotechnology* 8, 587–93 (2013).

[Gerber 2002] Gerber, A., et al. "Extraordinary Hall effect in magnetic films" *Journal of magnetism and magnetic materials* 242 (2002): 90-97.

[Gignoux 2005] Damien Gignoux *et al* "Magnetism: Fundamentals" ISBN 0387229671, 9780387229676 Springer, 2005

[Gilbert 2004] Thomas L. Gilbert "A Phenomenological Theory of Damping in Ferromagnetic Materials *" IEEE TRANS ON MAGNETICS*, VOL. 40, 3443 (2004)

[Haazen 2013] Haazen P.P.J *et al*., "Domain wall depinning governed by the spin Hall Effect", *Nature Materials* 12,299–303(2013)

[Hals 2009] Hals, K. M. D *et al*,. "Intrinsic Coupling between Current and Domain Wall Motion in (Ga , Mn) As". *Physical Review Letters* 102, 256601 (2009).

[Haney 2013] Haney, P. M. *et al*., "Current induced torques and interfacial spin-orbit coupling: Semiclassical modeling". *Physical Review B* 87, 174411 (2013).

[Hayashi 2006] Hayashi, M. *et al*. "Dependence of current and field driven depinning of domain walls on their structure and chirality in permalloy nanowires". *Physical Review Letters* 97, 207205 (2006).

[Hayashi 2007] Hayashi, *et al*., "Current driven domain wall velocities exceeding the spin angular momentum transfer rate in Permalloy Nanowires". *Physical Review Letters* 98, 037204 (2007)

[Hayashi 2008] Masamitsu Hayashi *et al.*, "Current-Controlled Magnetic Domain-Wall Nanowire Shift Register", *Science*, 320 5873, 209-211

[Hoffman 2011] Hoffmann, A. "Spin Hall Effects in Metals". *IEEE Transaction. Magnetics.* 49, 5172–5193 (2013).

[Hrabec 2014] Hrabec, A. *et al*., "Measuring the Dzyaloshinskii-Moriya interaction inversion in Pt/Co/Ir/Pt multilayers", *Physical Review Letter* B 90, 020402

[Hubert 1988] Hubert, A. and *Schäfer*, R "Magnetic Domains: The Analysis of Magnetic Microstructures." Berlin: Springer, 1998.

[Inoue 2004] Inoue, J *et al.*, "Suppression of the persistent spin Hall current by defect scattering". *Physical Review B* 70, 041303 (2004).

[Je 2013] Je, S-G *et al*. "Asymmetric Magnetic Domain-Wall Motion by the Dzyaloshinskii-Moriya Interaction." *Physical Review B* 88, 214401 (2013)

[Karplus 1954] Karplus, R. *et al*., "Hall Effect in Ferromagnetics". *Physical Review* 95, 1154–1160 (1954).

[Kato 2004] Kato, Y. et al., "Current-Induced Spin Polarization in Strained Semiconductors". *Physical Review Letters* 93, 176601 (2004).

[Kim 2012] Kim, K.W *et al*., (2012). "Magnetization dynamics induced by in-plane currents in ultrathin magnetic nanostructures with Rashba spin-orbit coupling". *Physical Review B*, 85 :180404. Kim, J., (2012a). "Layer thickness dependence of the current-induced effective field vector in Ta / CoFeB / MgO". *Nature Materials*, 12 :240-245.

[Kläui 2005] Kläui, M. *et al*., "Direct observation of domain-wall configurations transformed by spin currents". *Physical Review Letters* 95, 026601 (2005).

[Klaui 2003] Kläui.M *et al*., "Domain wall motion induced by spin polarized currents in ferromagnetic ring structures" *Applied Physics Letters* 83, 105 (2003)

[Kontani 2007] Kontani, H. *et al*., "Study of intrinsic spin and orbital Hall Effects in Pt based on a (6 s , 6 p , 5 d) tight-Binding Model". *Journal of the Physical Society of Japan* 76, 103702 (2007)

[Landau-Lifshitz 1935] Landau, L. D. Lifshitz, E. M. "On the theory of the dispersion of magnetic permeability in ferromagnetic bodies", *Physikalische zeitschrift der Sowjetunion* 8, 153 (1935).

[Lee 2010] Lee, J.C. *et al,*. "Roles of adiabatic and non-adiabatic spin transfer torques on magnetic domain wall motion" *arXiv:1006.1216v1*

[Lemerle 1988] Lemerle, S. *et al*., "Domain wall creep in an ising ultrathin magnetic film", Physical Review Letter 80, 849 (1998)

[Liu 2011] Liu, L *et al*., "Spin-Torque Ferromagnetic Resonance Induced by the Spin Hall Effect." *Physical Review Leters.* 106, 036601 (2011).

[Liu 2012] Liu, L. *et al*. "Spin-torque switching with the giant spin Hall effect of tantalum". *Science* 336, 555–558 (2012).

[Luttinger 1958] Luttinger, J. "Theory of the Hall effect in ferromagnetic substances." *Physical Review* 112, 739 – 751 (1958).

[Manchon 2009] Manchon, A. & Zhang, S. "Theory of spin torque due to spin-orbit coupling". *Physical Review B* 79, 094422 (2009).

[Meier 2007] Meier, G. *et al*. "'"Direct imaging of stochastic domain-wall motion driven by nanosecond current pulses". *Physical Review Letters* 98, 187202 (2007).

[Metaxas 2007] Metaxas, P. J. *et al*., "Creep and flow regimes of magnetic domain-wall motion in ultrathin Pt/Co/Pt films with perpendicular anisotropy", *Physical Review Letters* 99, 217208 (2007).

[Miron 2009] Miron, I. M. *et al. «* Domain Wall Spin Torquemeter". *Physical Review Letters.* 102, 137202 (2009).

[Miron 2011] Miron, I. M. *et al.*, "Fast current-induced domain-wall motion controlled by the Rashba effect". *Nature Materials* 10 419-423 (2011)

[Miron 2011 Sup] Miron, I. M. *et al.* "Supplementary information:Perpendicular switching of a single ferromagnetic layer induced by in-plane current injection". *Nature* 476, 189–93 (2011).

[Miron 2011] Miron, I. M. *et al.* "Perpendicular switching of a single ferromagnetic layer induced by in-plane current injection". *Nature* 476, 189–93 (2011).

[Miron et al., 2010] Miron, I.M. *et al*., "Current-driven spin torque induced bythe Rashba effect in a ferromagnetic metal layer". Nature Materials, 9(3) :230-234(2010)

[Monso 2002] Monso, S., *et al*. "Crossover from in-plane to perpendicular anisotropy in Pt/CoFe/AlOx sandwiches as a function of Al oxidation: A very accurate control of the oxidation of tunnel barriers." *Applied physics letters* 80.22 (2002)

[Moriya 1960] Moriya, T. "Anisotropic superexchange interaction and weak ferromagnetism." *Physical Review* 120.1 (1960)

[Mougin 2007] Mougin, Alexandra, *et al*. "Domain wall mobility, stability and Walker breakdown in magnetic nanowires." *EPL (Europhysics Letters)* 78.5 (2007)

[Murakami 2003] Murakami, S., Nagaosa, N. & Zhang, S.-C. "Dissipationless quantum spin current at room temperature". *Science* 301, 1348–51 (2003).

[Murakami 2004] Murakami, S., *et al*, "SU(2) non-Abelian holonomy and dissipationless spin current in semiconductors". *Physical Review. B* 69, 235206 (2004).

[Nagaosa 2010] Nagaosa, N *et al.,* "Anomalous Hall effect". *Reviews of Modern Physics* 82, 1539–1592 (2010).

[Néel 1954] Néel, L., "Anisotropie magnétique superficielle et surstructures d'orientation", *Journal de Physique et le Radium* 15, 225-239 (1954).

[O'Handley 1999] O'Handley, R. C. (1999). "Modern Magnetic Materials : Principles and Applications".

[Ortiz 2013] Ortiz Pauyac, C. *et al*., "Angular dependence and symmetry of Rashba spin torque in ferromagnetic heterostructures". *Applied Physics Letters.* 102, 252403 (2013).

[Pi 2010] Pi, U. H. *et al.* "Tilting of the spin orientation induced by Rashba effect in ferromagnetic metal layer". *Applied Physics Letters.* 97, 162507 (2010).

[Piechon 2007] Piéchon, P., *et al*., "Spin transfer torque in continuous textures: Semiclassical Boltzmann approach" *Physical Review B* 75, 174414 (2007)

[Ralph 2008] Ralph, D. C. and ***Stiles, M. D. "spin transfer torques"***, *Journal of Magnetism and Magnetic Materials* 320, 1190-1216 (2008)

[Rizzo 2013] Rizzo, N. D. *et al*., "A fully functional 64 Mb DDR3 ST-MRAM built on 90 nm CMOS technology." *IEEE Transaction Magnetics* 49, 4441-4446 (2013).

[Rodmaq 2003] Rodmacq. B., *et al*., "Crossovers from in-plane to perpendicular anisotropy in magnetic tunnel junctions as a function of the barrier degree of oxidation", *Journal of Applied Physics* 93, 7513 (2003).

[Rodmaq 2009] Rodmacq. B., *et al*., "Influence of thermal annealing on the perpendicular magnetic anisotropy of Pt/Co/AlOx trilayers", *Physical Review B* 79, 024423 (2009).

[Ryu 2013] Ryu, K. S. *et al*., "Chiral spin torque at magnetic domain walls". *Nature Nanotechnology* 8(7), 527-533. (2013).

[Schryer 1974] N. L. Schryer, L. R. Walker, "The motion of 180° domain walls in uniform dc magnetic fields", Journal of Applied Physics 45 (1974) 5406.

[Sinova 2004] Sinova, J. *et al.* "Universal Intrinsic Spin Hall Effect". *Physical Review Letters* 92, 126603 (2004).

[Šipr 2008] Šipr, O. *et al*, "Influence of composition, manybody effects, spin-orbit coupling, and disorder on magnetism of Co-Pt solid-state systems". *Physical Review B* 78, 144403 (2008)

[Smit 1958] Smit, J. "The spontaneous Hall effect in Ferromagnetics II". *Physica* 24, 39–51 (1958).

[Suzuki 2011] Suzuki, T *et al*., "Current-induced effective field in perpendicularly magnetized Ta / CoFeB / MgO wire". *Applied Physics Letters*, 98 :142505 (2011).

[Tanaka 2008] Tanaka, T. *et al.* "Intrinsic spin Hall effect and orbital Hall effect in 4d and 5d transition metals". *Physical Review B* 77, 165117 (2008).

[Tetienne 2014] J.-P. Tetienne *et al*., "The nature of domain walls in ultrathin ferromagnets revealed by scanning nanomagnetometry", *Nature Communications* ,6,Article number 6733 (2014)

[Thiaville 2004] Thiaville, A. *et al.,* "Domain wall motion by spin-plarized current: a micromagnetic study", *Journal of Applied Physics* 65, 7049 (2004)

[Thiaville 2012] Thiaville, A. *et al*., "Dynamics of Dzyaloshinskii domain walls in ultrathin magnetic films". *Europhysics Letters*, *100*(5), 57002. (2012).

[Vanhaverbeke 2007] Vanhaverbeke, A. *et al*., "Simple model of current-induced spin torque in domain walls", *Physical Review B* 75, 024411 (2007).

[Waintal 2004] Waintal, X. *et al*., "Current-induced distortion of a magnetic domain wall", Europhysics Letters 65, 427 (2004).

[Wang 2012] Wang, X. & Manchon, A. "Diffusive Spin Dynamics in Ferromagnetic Thin Films with a Rashba Interaction". *Physical Review Letters* 108, 117201 (2012).

[Yamaguchi 2004] Yamaguchi, A. *et al*. "Real-space observation of current-driven domain wallmotion in submicron magnetic wires." *Physical Review Letters* 92, 077205 (2004).

[Yang 2011] H. X. Yang, *et al.,* "First-principles investigation of the very large perpendicular magnetic anisotropy at Fe|MgO and Co|MgO interfaces", *Physical Review B* 84, 054401 (2011).

[Zhang 2004]S. Zhang, Z. Li, "Roles of nonequilibrium conduction electrons on the magnetization dynamics of ferromagnets", *Physical Review Letters* 93, 127204 (2004).]

Chapter II

[Bonfim 2001] Bonfim, M. "Micro bobines à champ pulsé : applications aux champsforts et à la dynamique de renversement de l'aimantation à l'échelle de la nanoseconde par effet Kerr et Dichroïsme Circulaire Magnétique de rayons X". *PhD thesis*, UniversitéJoseph Fourier, Grenoble(2001).

[Manchon 2008] Manchon. A. *et al.,* "Analysis of oxygen induced anisotropy croosover in Pt/Co/MOx trilayers", *Journal of applied physics* 104, 043914 (2008)

[Monso 2002] Monso, S., *et al*. "Crossover from in-plane to perpendicular anisotropy in Pt/CoFe/AlOx sandwiches as a function of Al oxidation: A very accurate control of the oxidation of tunnel barriers." *Applied physics letters* 80.22 (2002)

[Schäfer 2007] R Schäfer, "Handbook of magnetism and advanced magnetic materials, chapter XX: Investigation of Domains and dynamics of Domain walls by the Magneto-optical Kerr effect".

Chapter III

[Chen 2013] Chen, G. *et al.,* "Tailoring the chirality of magnetic domain walls by interface engineering". *Nature communications*, *4*. 2671 (2013)

[Emori 2013] Emori, S. *et al*, "Current-driven dynamics of chiral ferromagnetic domain walls". *Nature materials*, *12*(7), 611-616 (2013).

[Ferré J 2013]., *et al.,* "Universal magnetic domain wall dynamics in the presence of weak disorder" *C. R. Physique* 14 651–666 (2013)

[Garello 203] Garello, K. *et al.* "Symmetry and magnitude of spin-orbit torques in ferromagnetic heterostructures". *Nature Nanotechnology* 8 587-593 (2013)

[Gorchon 2014]Gorchon, J., *et al*. "Pinning-Dependent Field-Driven Domain Wall Dynamics and Thermal Scaling in an Ultrathin Pt/Co/Pt Magnetic Film." *Physical Review Letter*. 113.2 027205 (2014).

[Haazen 2013] Haazen P.P.J *et al*., "Domain wall depinning governed by the spin Hall Effect", *Nature Materials* 12,299–303(2013)

[Hrabec 2014] Hrabec, A. *et al*., "Measuring the Dzyaloshinskii-Moriya interaction inversion in Pt/Co/Ir/Pt multilayers", *Physical Review Letter* B 90, 020402

[Je 2013] Je, S-G *et al*. "Asymmetric Magnetic Domain-Wall Motion by the Dzyaloshinskii-Moriya Interaction" *Physical Review B* 88, 214401 (2013)

[Lavrijsen 2012] Lavrijsen, R. *et al*., "Asymmetric Pt/Co/Pt-stack induced sign-control of current-induced magnetic domain-wall creep". *Applied Physics Letters*, *100*(26), 262408 (2012).

[Lavarijsen 2015] . Lavarijsen *et al*., "Asymmetric magnetic bubble expansion under in-plane field in Pt/Co/Pt: Effect of interface engineering", *Physical Review B 91*, 104414, (2015)

[Lee 2010] Lee, J.C. *et al*., "Roles of adiabatic and non-adiabatic spin transfer torques on magnetic domain wall motion". *arXiv:1006.1216v1*

[Liu 2012] Liu, L. *et al*. "Spin-torque switching with the giant spin Hall effect of tantalum". *Science* 336, 555–558 (2012).

[Metaxas 2007] P. J. Metaxas *et al*, "Creep and Flow Regimes of Magnetic Domain-Wall Motion in ultrathin Pt/Co/Pt Films with Perpendicular Anisotropy" *Physical Review Letters* 99, 217208 (2007)

[Miron 2009] Miron, I. M. (2009). "Etude de l'interaction entre un courant polarisé en spin et une paroi de domaine magnétique dans des matériaux à aimantation perpendiculaire ». *PhD thesis*, Université Joseph Fourier, Grenoble.

[Miron 2011a] Miron, I. M. *et al.* "Perpendicular switching of a single ferromagnetic layer induced by in-plane current injection". *Nature* **476,** 189–93 (2011).

[Miron 2011b]Miron, I. M. *et al*. "Fast current-induced domain-wall motion controlled by the Rashba effect" *Nature Materials* 10,419–423(2011)

[Moore 2008] Moore, TA *et al*., "High domain wall velocities induced by current in ultrathin Pt/Co/AlOx wires with perpendicular magnetic anisotropy", *Applied Physics Letters* 93, 262504 (2008)

[Ryu 2013] Ryu, K. S. et al., "Chiral spin torque at magnetic domain walls". *Nature Nanotechnology 8(7), 527-533.* (2013).

[Šipr 2008] Šipr, O. *et al*, "Influence of composition, many body effects, spin-orbit coupling, and disorder on magnetism of Co-Pt solid-state systems". *Physical Review B* 78, 144403 (2008)

[Tetienne 2014] J.-P. Tetienne *et al*., "The nature of domain walls in ultrathin ferromagnets revealed by scanning nanomagnetometry", *Nature Communications* ,6,Article number 6733 (2014)

[Thiaville 2012] Thiaville, A. *et al*., "Dynamics of Dzyaloshinskii domain walls in ultrathin magnetic films". *Europhysics Letters*, *100*(5), 57002. (2012).

Chapter IV

[Baibich 1988] M. N. Baibich *et al*., "Giant Magnetoresistance of (001)Fe/(001)Cr Magnetic Superlattices", Physical Review Letters 61 (21): 2472–2475 (1988)

[Belmeguenai 2015] M, et al. "Interfacial Dzyaloshinskii-Moriya interaction in perpendicularly magnetized Pt/Co/AlO x ultrathin films measured by Brillouin light spectroscopy." *Physical Review B* 91.18 (2015): 180405.

[Boulle 2013] Boulle, O. *et al*., "Domain wall tilting in the presence of the Dzyaloshinskii-Moriya interaction in out-of-plane magnetized magnetic nanotracks". *Physical review letters* 111 217203 (2013)

[Dieny 2010] Dieny, B. *et al*., "Spin-transfer effect and its use in spintronic components", *International Journal of Nanotechnology*. 7, 591 (2010)

[Miron 2011] Miron, I. M. *et al*. "Perpendicular switching of a single ferromagnetic layer induced by in-plane current injection", *Nature* 476, 189–193 (2011).

[Miyazaki 1995] Miyazaki, T. *et al*., "Giant magnetic tunneling effect in Fe/Al_2O_3/Fe junction". *Journal of Magnetism and Magnetic Materials*, 139: L231–L234 (1995)

[Parkin 2008] Parkin, S. S. P. *et al*., "Magnetic domain-wall racetrack memory", Science 320, 190–194 (2008).

[Ryu 2012] Ryu, K. S. *et al*. "Current induced tilting of domain walls in high velocity motion along perpendicularly magnetized micron-sized Co/Ni/Co racetracks". *Applied Physics Express* 5 093006 (2012)